UNIVERSITY OF CALIFORNIA SANTA CRUZ

TOWARDS HIERARCHICAL STRUCTURAL SELF-ASSEMBLY OF CONJUGATED POLYELECTROLYTE LIGHT HARVESTING COMPLEXES

A dissertation submitted in partial satisfaction

of the requirements for the degree of

DOCTOR OF PHILOSOPHY

in

Chemistry

by

Carmen J. Segura

September 2019

The Dissertation of Carmen Segura is approved:

_____

Professor Alexander L. Ayzner, Chair

_____

Professsor Yat Li

_____

Professor Ilan Benjamin

_____

Quentin Williams

Acting Vice Provost and Dean of Graduate Studies

Contents

List of Figures

Abstract

TOWARDS HIERARCHICAL STRUCTURAL SELF-ASSEMBLY OF CONJUGATED POLYELECTROLYTE LIGHT HARVESTING COMPLEXES

Carmen Segura

The dramatic decrease in the world's finite reserve of fossil fuels has led to an increase demand for alternative energy resources. Inspired by natural photosystems that were fine-tuned by nature through billions year of evolution. The focus of this research aims to mimic and improve upon nature's approach of capturing solar energy by constructing an artificial photosystem. The method of approach was done by creating 'soft supramolecular complexes' based on conjugated polyelectrolyte (CPE) complexes as analogs to nature's light harvesting machinery. Conjugated polyelectrolytes (CPEs) are a class of quasi-1D structures whose delocalization of pi-electrons through their backbone enables the motion and transport of electrical charge and excitation energy; In addition, they bear ionic sides chains per repeating monomer unit that enable these non-polar macromolecules to be water soluble and facilitate their microstructural self-assembly. In order to construct efficient 'light harvesting complexes' it is important to understand the physics that drive the self-assembly and microstructure of the CPE complexes and how this relates to their electronic energy transfer (EET) dynamics between the donor and acceptor units of the CPE complexes. The initial phase of this work focused on constructing 'light harvesting complexes' centered on pairing oppositely charged and electronically coupled CPEs PFPI-donor and PTAK-acceptor. Results from this initial investigation showed evidence of EET between the donor-

acceptor complexes as well as the ability to tune the EET dynamics of the system by varying the molar charge composition of the CPEs. The design of projects forward led to a natural trajectory focused on building on the complexity by first incorporation of ionic surfactants, mixed micelle systems with varying charge densities and finally the templating of donor-acceptor CPEs as a layer-by-layer assembly onto a charged liposome scaffold. The local micro and macrostructural morphology of the CPE complexes was characterized using a combination of Dynamic light scattering (DLS), small x-ray scattering (SAXS) and Confocal Laser Scanning microscopy (CLSM) techniques. The use of scattering techniques and light microscopy are complementary to one another since they access different length scales from nanometer details to the visualization of CPE-liposome micron sized structures. These structural techniques combined with optical techniques provided insight to the relation of morphology and photo-physical properties of these CPEC-Surfactant/Lipid interactions. The results of this dissertation demonstrate the capability to ironically assemble a stable multicomponent modular light harvesting system. The influence of surface charge, charge density of amphiphilic systems had on both the electronic structure and microstructure of CPE was deeply explored. It was found that through careful choice, ternary molecules and self-assembled structures such as surfactants and liposomes can be used to manipulate the electronic structure and thus the energy transfer dynamics of higher order CPE systems. This research forms a basis for the creation of a soft, light-weight artificial photosystem with the potential of converting sunlight into chemical fuels.

Dedication

My Amá – Manuela Casillas – For your endless support, love and wisdom.

My Sister – Esmeralda Segura-Casillas – For your sense humor, humility and inspiring perseverance.

Acknowledgment

My advisor, Professor Alexander Ayzner for his intellectual guidance and professional support through my Ph.D. My committee members, Professor Yat Li and Professor Ilan Benjamin, for dedicating their time and providing feedback through every milestone. The Ayzner group, past and current: Dr. Vincent Duong, Michael Roders, Will Hollingsworth and Anna Johnston. Along with being supportive colleagues they became close and dear friends. Staff scientists at the Stanford Synchrotron Light Source, Ivan Rajkovic, Tsutomu Matsue and Thomas Weiss for their beamline support and helpful insight. Staff scientist at UCSC; Director of NMR, Jack Lee Director of the Microscopy center, Ben Abrams, their help was invaluable. My friendships development during my time as a graduate studies. Thank you all.

Chapter 1

General Background

1.1 Motivation and Overview

There has been significant interest in the use of "soft materials" both in the context of the development of new technologies as well in the context of fundamental understanding in the physics of "new" technologies but as well gaining more fundamental insight in the soft molecular machinery of the natural world. Semiconductor π-conjugated polymers are key materials for both in the development in new soft technologies and are key in the light harvesting machinery used by photosynthetic organisms.

Major interest of conjugated polymers has been in the development of organic solar cells (OSCs), The current record efficiency of OSCs is 17%[1] , however, they still haven't gotten close to being competitive to inorganic silicon solar cells that currently have an efficiency of ~44%. Even less so to the efficiency and elegance to the light harvesting architecture used by photosynthetic organisms. Over the evolutionary timescale of a millennia, this light harvesting systems have evolved a delicate balance in the organization photophysical process and reactions, maximizing the organization hierarchy of compounds based on time scales and fixed spatial distances.[2–5] **Figure 1.1**. (bottom plot) shows a few select pigments used by photosynthetic organisms to harvest energy from the sun. As can be seen the select pigments maximize the use of the solar radiance that reaches the earth, the spectral radiance of the sun graph is shown as the

top plot of **Figure 1.1**. Approximately 85 PW of solar radiation reaches the earth at sea level, after initial reflection back to space and absorption by the clouds. The averaged total solar power used by terrestrial photosynthesis amounts to ~ 0.09% (75TW) of the total solar power available to land organisms**.**

The average total power consumption of the human world in 2018 was 23 TW, a +3.5% increase from the past year. It's expected that with the growth of global development the global energy usage will continue to rise, therefore, its imperative to focus on the development of new technologies that pertain to sustainable energy.

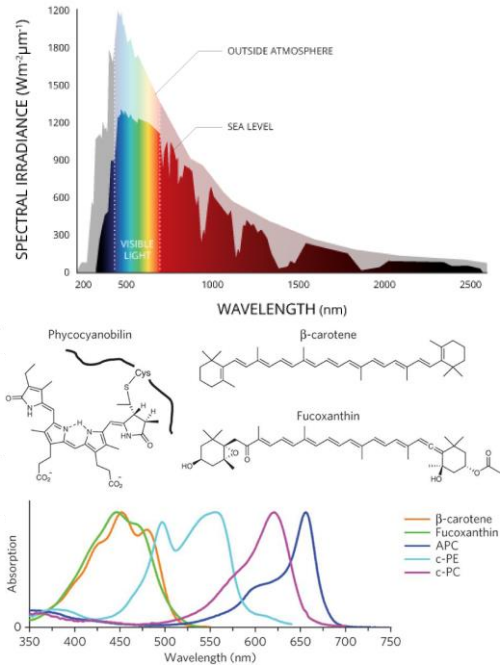

Figure 1.1 Top Panel: Solar spectral radiance. Bottom Panel: Representative spectra of common photosynthetic pigments, adapted from reference 2.

Semiconductor π-conjugated polymers with charged side chains (CPEs) have caught interest in the context of light harvesting materials as well for the development of applications related to sensing, biomedical and materials. This has coincided with development of the synthesis of conjugated polyelectrolytes[6–8]. The optical properties

of CPEs have a strong relationship with their microstructure that will be reviewed in the following sections.

1.1.2 Structural and Photo-Physical Relationship of Conjugated Polymers

Conjugated polyelectrolytes are composed of conjugated monomer subunits that have alkyl side chains with functionalized ionic groups at the end. The alternating single and double bonds of the backbone classifies CPEs as organic semiconductors. As shown previously, **Figure 1.2** shows examples of CPEs with varying monomer backbones and ionic side chains. The monomer subunit of the CPE can influence rigidity and overall macromolecular structure of CPE complexes and therefore the types of interactions different segments the multi-chromophore backbone can experience.

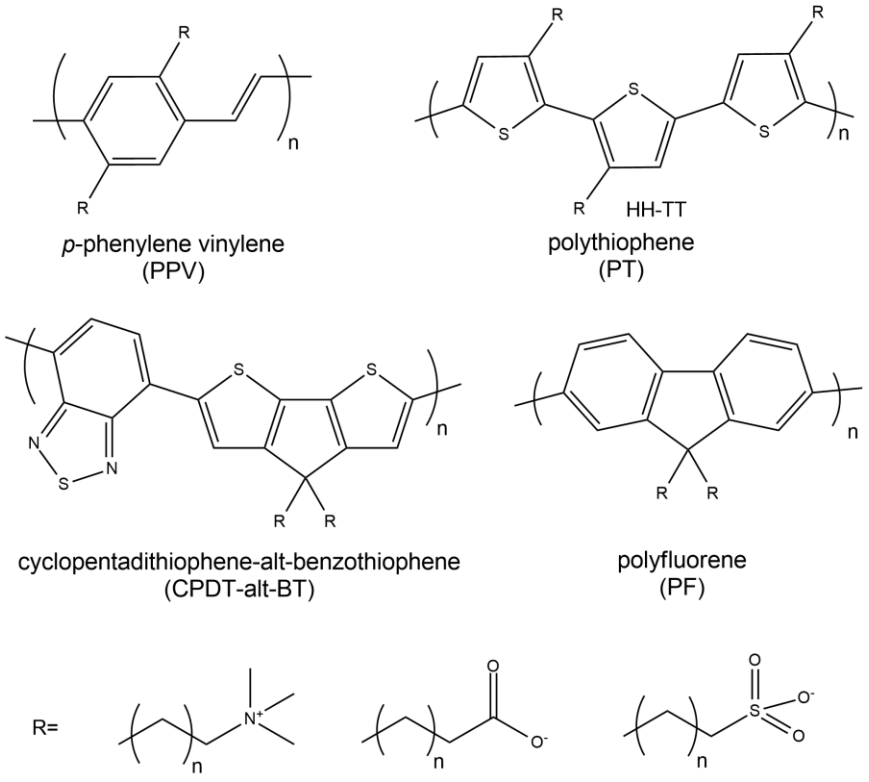

Figure 1.2 Examples of conjugated polyelectrolytes backbone chemical structures and ionic side chains.

Kasha's theory is a model developed in the 1950's that described emergent spectroscopic properties from the aggregation of individual chromophore molecules. Kasha found that depending on the orientation of the aggregates i.e. either head to tail (J aggregate) or a side to side configuration (H aggregate) it would lead to distinct spectroscopic signatures[9]. However, this theory only applied to the individual aggregation of chromophores it was expanded to polymers with repeated conjugated monomer subunits by Spano et al.[10–12] In Spano's expanded H & J aggregate model. Analogous to Kasha's theory of monomer dipoles oriented in a head to tail fashion, J-aggregates in the polymers are characterized by through bond interactions between the repeated monomer units, where like in the case individual chromophore molecules, the monomer subunits on the polymer backbone are oriented in a head to tail fashion as well. This type of orientation leads to negative excitonic coupling. Given to the flexible nature of polymers, through space interactions between different segments of polymer chains (side to side configuration) leads to positive excitonic coupling to the parallel orientation of transition dipoles in this geometry, resulting in H like spectroscopic behavior. **Figure 1.3** shows the how the LUMO band structure at zero momentum changes (k=0) with the coupling of the monomer units within conjugated polymer chains. J like coupling has a positive curvature at the LUMO band, therefore the exciton lies in lowest in energy at k=0 and this leads to a high 0-0/0-1 photoluminescence (PL) vibronic peak ratio due to the highly dipole allowed transition from the lowest excited state to the ground state. In the case H like coupling, the resulting spectral signature is different. There is a negative curvature at the LUMO band, therefore the exciton lies in

highest in energy at k=0 and this leads to a low 0-0/0-1 PL vibronic peak ratio due to transition from the lowest excited state to the ground state being dipole forbidden.

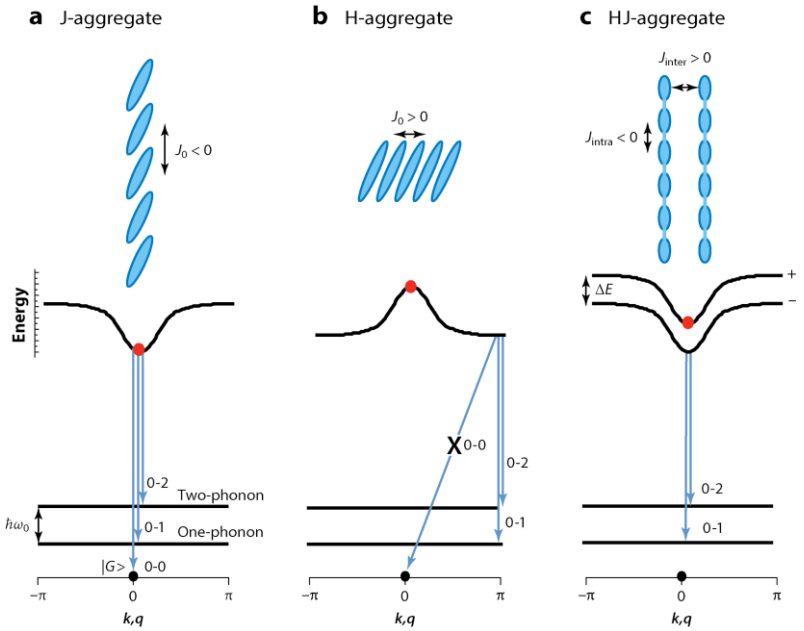

Figure 1.3 Schematic of H and J aggregation electronic structures and transitions adapted from Reference 5.

1.1.3 Forster Resonant Energy Transfer

Electronic energy transfer (EET) is an inductive resonance interaction between the transition dipole moments of donor μ_D and acceptor μ_A chromophore molecules separated at a long of distance where other close proximity (~5Å) energy transfer methods that involves the intermolecular orbital overlap (IOO) between the donor and acceptor orbitals cannot be taken into account. This interaction between donor and acceptor molecules is driven by electronic coupling (V). Coupling that is not in the short range is a coulombic interaction. The coulombic coupling V^{Coul} is dependent on

several factors (**Equation 1.2**): R is the center to center intermolecular separation between transition dipole moments (μ) of the donor (μ_D) and acceptor (μ_A), ε_0 is the dielectric constant of the solvent medium, the orientation factor κ, describes the relative orientation of between the donor and acceptor transition-dipole-moments, in the case of randomly oriented donor-acceptor systems the isotropic average of the dipole orientation factor is taken as 2/3.

$$V = V^{Coul} + V^{Short(IOO)} \qquad \textbf{(1.1)}$$

$$V^{Coul} = \frac{1}{4\pi\varepsilon_0}\frac{\kappa\mu_D\mu_A}{R^3} \qquad \textbf{(1.2)}$$

Increased coupling (V^{Coul}) between donor and acceptor chromophores increases the probability of energy transfer taking place and is incorporated in Forster's equation for electronic energy transfer (**Equation 1.3**). Equation 1.3 summarizes the several parameters that influence the rate of EET, parameters not included in V^{Coul}: the donor lifetime (τ_D), the quantum yield of the donor fluorescence (ϕ_D), n is the medium index of refraction and the spectral overlap (J_F) (**Equation 1.4**) the most important of these parameters. The spectral overlap determines if EET is thermodynamically allowed between a donor-acceptor pair. **Figure 1.4** summarizes the sequence of event in resonant energy transfer and the coupling dependence of the initial and final electronic states of the donor and acceptor molecules involved (|D′A⟩ and |DA′⟩). FRET is initiated by excitation of the donor D⟶D', in the excited state the donor undergoes vibrational relaxation. During the de-excitation of the donor, the oscillations of its electrons induces oscillation of the acceptor's electrons, this causes electronic excitation of the acceptor. This inductive resonance interaction between the donor-

acceptor is what transfers the electronic excitation energy from the donor to acceptor.[13–17]

$$k_{Forster} \propto \frac{1}{\tau_D}\frac{\kappa^2 \phi_D J_F}{n^4}\frac{1}{R^6} \qquad \textbf{(1.3)}$$

$$J_F(\lambda) = \int F_D(\lambda)\varepsilon(\lambda)\lambda^4 d(\lambda) \qquad \textbf{(1.4)}$$

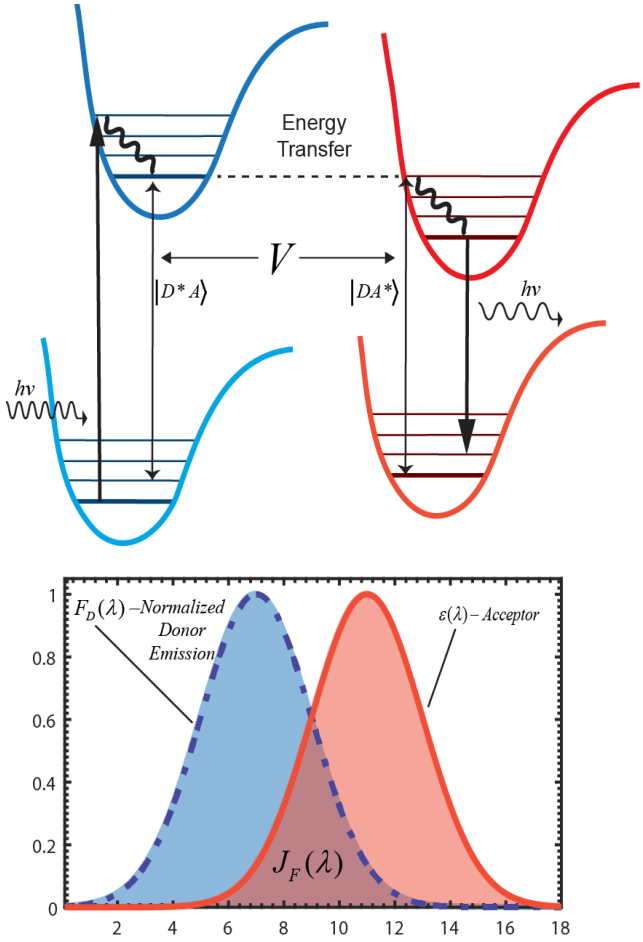

Figure 1.4 FRET Summary.

1.2 Experimental and Analytical Methods

1.2.1 Dynamic Light Scattering

In terms of SLS and SAXS where the foundations of these methods are very similar, in the case of both these methods they are very complimentary to DLS. However, SAXS requires a synchrotron radiation light source, while SLS can be performed in the same light scattering instrument as DLS. Together DLS and SLS are commonly applied to study the particle size of many materials/fields especially polymer systems.

The premise dynamic light scattering involves the fluctuation of intensity with respect to time from molecules in a solution. **Figure 1.5** shows the basis of DLS. In the right upper hand corner of **Figure 1.5** it shows the change in fluctuation intensity of scattered light from particles in solution with time. Over a large time scale, the fluctuation of intensity is random due to Brownian motion, however, at very short time intervals the fluctuation of intensity isn't random and doesn't change significantly, such that that at short time differences the intensities are correlated. In the bottom of **Figure 1.5** its shows the diagram of a light scattering set up. A laser hits the sample, the sample scatters the light, the scattered light is detected by a photon counting device where the signal becomes processed and the scattered intensities in a small-time domain become correlated resulting in a correlation function.

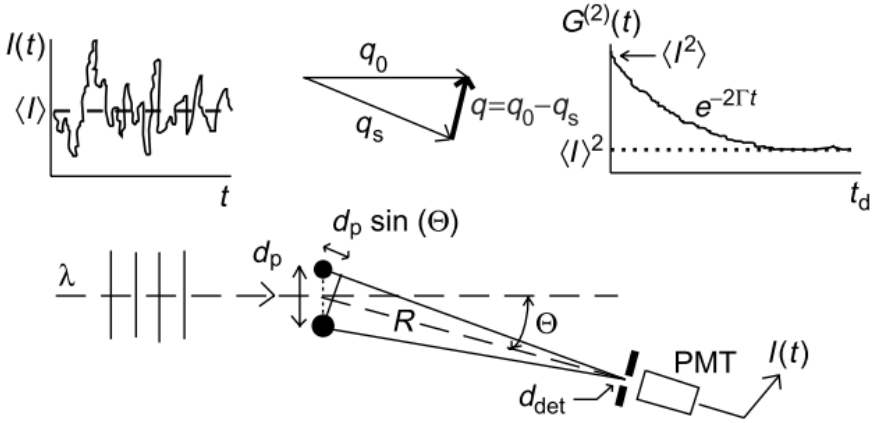

Figure 1.5 The basis of DLS, adapted from reference 19.

Mathematically this is described by **Equation 1.5** The intensity is recorded over a long period of time and compared at different time intervals. The processing device a digital autocorrelator approximates **Equation 1.5** to **Equation 1.6**. Within **Equation 1.6** lies the dynamic information of the system of focus in **Equation 1.7** where the decay rate can be obtained and the diffusion coefficient, Q is the scattering vector (**Equation 1.8**). Q is the result of the incident and scattering vectors k_0 and k_1, respectively. where θ is half of the scattering angle defined within the Bragg equation. Using the Stokes-Einstein equation the radius of hydration can be obtained **Equation 1.9** .[18–20]

$$G^{(2)}(t) =< I(0)I(t) >= \lim_{T\to 2T} \int_{-T}^{T} I(t') \cdot I(t'+t)dt' \qquad \textbf{(1.5)}$$

$$G^{(2)}(t) = B(1 + f \cdot \left|g^{(1)}(t)\right|^2) \qquad \textbf{(1.6)}$$

$$g_1(t) \; = \; e^{-t/\tau} = e^{-\Gamma t} = e^{-Dq^2 t}, \Gamma = \tau^{-1} \; = Dq^2 \qquad \textbf{(1.7)}$$

$$Q = K_o - K_1 = \frac{4\pi n}{\lambda} sin(\frac{\theta}{2}) \qquad \textbf{(1.8)}$$

$$R_h = \frac{kT}{6\pi\eta_o D} \; eqn.(5) \qquad \textbf{(1.9)}$$

1.2.2 Small Angle x-Ray Scattering

Small angle x-Ray scattering is an analytical method that is used to characterize and determine the structures of particles using a synchrotron light source. It is a complementary structural characterization technique to light scattering; it probes small length scale ranges $10^1 – 10^3$ Å. The average shape and size of particles can be found from solution or solid samples. Given that the work in thesis, solely employed solutions SAXS, the rest of the SAXS background will be focused on transmission SAXS, as opposed to other SAXS method that are often used to characterize solids, such as grazing-incidence SAXS that is use to characterize the surface of films. However, experimentally they are very similar. In transmission SAXS, x-Rays are irritated through the sample. How the incoming x-rays scattered by particles in the solution, gives the particle structural and morphological information. The scattering of the x-rays can either be inelastic (loss of energy) or elastic (no loss of energy). When elastic scattering from particles this the detector it leads to a constructive interference on the detector (a bright spot) while inelastic scattering from particles leads to destructive interference (dark spots on the detector). The constructive interference pattern on the detector gives the structural information in reciprocal space, Q ($Å^{-1}$) (similar to DLS), where common names for Q ($Å^{-1}$) are "length of the scattering vector" or "momentum transfer", scattering vector in a SAXS experimental set up is shown in the diagram in **Figure 1.6**.

The total SAXS scattering intensity profile is dependent on the N, the number of scattering particles and is a composed of the form factor P(Q) and structure factor

S(Q). The form factor gives the particles shape "form" and is purely a result from intraparticle scattering. The structure factor, gives information of the positions of particles relative to each other, therefore gives the "structural ordering" of particles in a densely packed and is a result of interparticle scattering. The majority the particle systems of this thesis work is considered to be in the "dilute regime" meaning that the structure factor doesn't contribute to the total scattering profile. [21–23]

$$I(Q) = N\,P(Q)\,S(Q) \qquad \textbf{(1.9)}$$

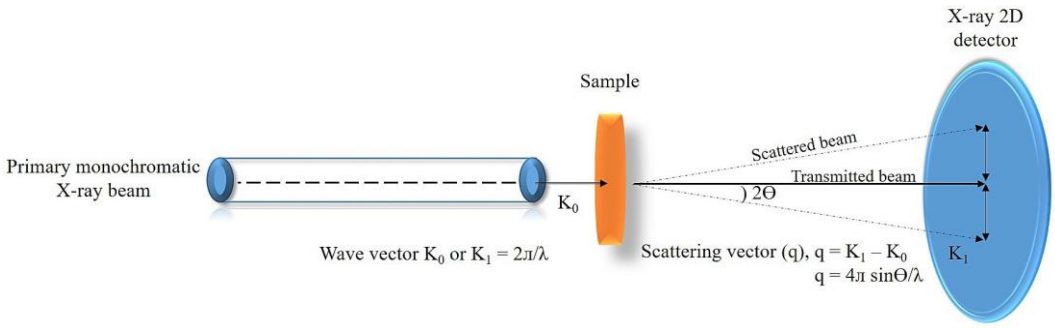

Figure 1.6 Schematic diagram of the incident beam of SAXS, adapted from reference 24.

In order to translate the structural information of the particles reciprocal space ($Å^{-1}$) needs to be converted to real space (Å). To do so requires a performing a Fourier transform on the form factor in order to obtain P(r), what is called the "pair-distance distribution function" (PDDF) (**Equation 1.0**).

$$I(Q) = 4\pi \int_0^\infty P(r)\,\frac{\sin Qr}{Qr}\,dr \qquad \textbf{(1.10)}$$

Deconvoluting the P(r) from the total scattering intensity proves to be difficult because attaining a Q range from zero to infinity isn't experimentally realistic. However, a

method developed by Glatter et al, allows the P(r) to be obtained by using the Indirect Fourier Transform (IFT) technique. The power of this technique is that pair-distance distribution functions can be obtained without using a model, meaning you don't need to know the exact morphologies/geometries of your samples) as well as interpolating the intensity in the low Q range.[24–29]

1.2.3 Diffusion Ordered Spectroscopy

Diffusion ordered spectroscopy (DOSY) is a pulse gradient spin-echo (PGSE) NMR technique that is commonly used to find the translation diffusion coefficient of molecules in solution. DOSY is based on the pairing of gradient pulses that encode and decode the diffusion information of nuclei active molecules in solution. The translation diffusion can be found by measuring the decay intensity of the NMR signal based on the gradient strength. It's important to clarify that DOSY is a series of 1D 1H NMR measurements not a 2D NMR measurement. **Equation 1.1** defines parameters involved in the DOSY measurement: D is the diffusion coefficient, g is the gyromagnetic ratios of the nuclei in the measurement, δ is the diffusion gradient pulse length and Δ is the diffusion delay. Commonly for a DOSY measurement, diffusion gradient pulse length and Δ is the diffusion delay are the parameters that are changed dependent on the size distribution of the samples the main parameters that are changed. large molecules would have larger diffusion coefficient, therefore, the diffusion gradient pulse length and Δ is the diffusion delay would need to be extended in order to capture the decay **Figure 1. 7** illustrates the basic pulse sequence (top panel) of a DOSY measurement and the bottom illustrates the magnetization vectors of the molecules nuclei during and as a result of the pulse gradient sequence, the magnetization vectors of the nuclei are

aligned in the x-direction (x-y plane), the first gradient pulse (δ) twists the magnetization along the z-axis creating corkscrew shape of the magnetization vectors, the corkscrew effect depends on the strength of the gradient pulse, stronger gradient pulse equals a stronger corkscrew effect of the magnetization vectors. During the diffusion time (Δ), the magnetization vectors of the samples diffuse in the vertical direction. The second gradient pulse 'decodes' the first gradient pulse, the resulting magnetization signals depend on the extend of diffusion from the nuclei in the vertical direction. [30,31]

$$I = I_o e^{-D\gamma^2 g^2 \delta^2 (\Delta - \delta/3)} \qquad \textbf{(1.11)}$$

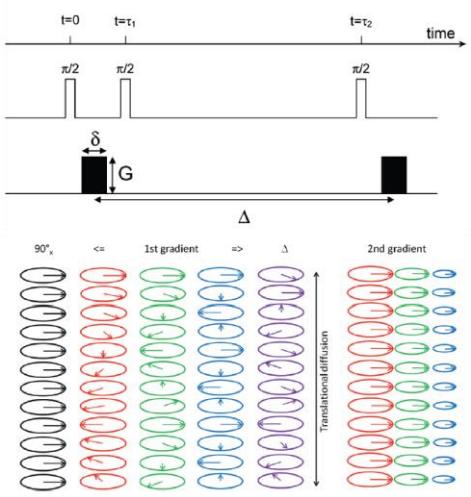

Figure 1.7 Basic pulse sequence of a DOSY measurement (Top Panel), Magnetization of NMR active nuclei during pulse gradients (Bottom Panel)

1.3 Concluding Remarks

The work of this thesis was inspired by natural light harvesting systems that were fine-tuned by nature through billions of years of evolution, the focus of this research aims to mimic nature's approach of capturing solar energy by constructing a self-assembled, artificial light-harvesting antennae capable of efficient electronic energy transfer (EET). The platform of this work focuses on pairing oppositely charged conjugated polyelectrolytes (CPEs) as a donor-acceptor system. Their light harvesting backbones together with their charged side chains enable the self-assembly of 'soft' supra-molecular complexes capable of EET. The aim of past and current projects has been to form a fundamental understanding of the structural self-assembly behavior of CPE Complexes with and without ternary agents.

The results from **Chapter 2** lay the foundation to build a higher order CPE based donor-acceptor assemblies. It was shown that oppositely charged CPEs may be complexed together in aqueous solution at certain molar charge ratios. Complexation of the donor PFPI CPE and an acceptor CPE re-PTAK lead to rapid electronic energy transfer upon photoexcitation even at both dilute and concentrated concentrations. In addition, the complexation lead to excited state emergent properties associated with the unwinding and binding of the acceptor ra-PTAK, that lead to photoluminescence ~20 factor quantum yield increase.

In **Chapter 3**, the same pair of donor/acceptor CPEs, PFPI and re-PTAK were used to study the self-assembly of the CPEs in the presence of ionic surfactants. The ionic self-assembly of CPEs was found to be highly dependent on the charge of the head group as well on the surfactant concentration. Results indicate that the solution structure of

the we can alter the solution structure of CPEs-surfactant complexes can be altered which in turn leads to control of electronic energy transfer efficiencies. Addition of the anionic surfactant (SDS) leads to extended locally ordered structures. In addition, results indicate a stronger PFPI-SDS binding interaction that outcompete the PFPI-PTAK interaction. While addition of the cationic surfactant (DTAC) lead to compressed disordered structures. However, in contrast to the above PFPI-SDS interaction. PTAK-DTAC-PFPI showed signs of a more cooperative interaction. Addition of PFPI to PTAK-DTAC complexes lead to increased conjugation of the PTAK backbone strongly supported by the spectroscopy.

From **Chapter 3** it was evident that the ionic nature surfactant head group played a significant role in the CPEs microstructure and therefore photo-physics. In **Chapter 4** the micellar composition was varied as a fraction of ionic to nonionic surfactant, thus we investigated the influence of surface charge density and sign of the surface charge on the CPE/micelle interactions. It was found that both the micelle charge density and the precise arrangement of charged sidechains along the CPE together result in either contorted or highly extended CPE microstructures that lead to charge density dependent CPE excited states.

In **Chapter 5**, a panchromatic layer-by-layer (LBL) CPE assembly was constructed. The PFPI (donor) – ra-PTAK (acceptor) pair CPEs were absorbed onto a cationic liposome (DOTAP). The successful assembly lays the foundation for the future ionically assembled antennae. Future work can build from this by incorporating electron acceptors into the lipid bilayer, further mimicking nature's architecture and organization for the capture of solar energy.

1.4 References

1. Wang, Y. *et al.* Organic and solution-processed tandem solar cells with 17.3% efficiency. **1098**, 1094–1098 (2018).

2. Jung, B. & Theato, P. Chemical Strategies for the Synthesis of Protein – Polymer Conjugates. *Adv. Polym. Sci.* 1–34 (2012). doi:10.1007/12

3. Frischmann, P. D., Mahata, K., Wu, F. & Wu, F. Chem Soc Rev. 1847–1870 (2013). doi:10.1039/c2cs35223k

4. Cheng, Y. & Fleming, G. R. Dynamics of Light Harvesting in Photosynthesis. (2009). doi:10.1146/annurev.physchem.040808.090259

5. Chenu, A. & Scholes, G. D. Coherence in Energy Transfer and Photosynthesis. *Annu. Rev. Phys. Chem.* **66**, 69–96 (2015).

6. Jiang, H., Taranekar, P., Reynolds, J. R. & Schanze, K. S. Conjugated polyelectrolytes: synthesis, photophysics, and applications. *Angew. Chem. Int. Ed. Engl.* **48**, 4300–16 (2009).

7. Wang, F. *et al.* Synthesis and Characterization of Water-Soluble Polythiophene Derivatives for Cell Imaging. *Sci. Rep.* **5**, 1–8 (2015).

8. Knaapila, M. *et al.* Conjugated polyelectrolyte (CPE) poly[3-[6-(N-methylimidazolium)hexyl]-2,5-thiophene] complexed with aqueous sodium dodecylsulfate amphiphile: synthesis, solution structure and "surfactochromic" properties. *Soft Matter* **7**, 6863 (2011).

9. Kasha, M. Energy Transfer Mechanisms and the Molecular Exciton Model for Molecular Aggregates. *Radiat. Res.* **20**, 55–70 (1963).

10. Spano, F. C. & Silva, C. H- and J-Aggregate Behavior in Polymeric Semiconductors. (2014). doi:10.1146/annurev-physchem-040513-103639

11. Niles, E. T. *et al.* J-aggregate behavior in poly-3-hexylthiophene nanofibers. *J. Phys. Chem. Lett.* **3**, 259–263 (2012).

12. Clark, J., Silva, C., Friend, R. H. & Spano, F. C. Role of intermolecular coupling in the photophysics of disordered organic semiconductors: Aggregate emission in regioregular polythiophene. *Phys. Rev. Lett.* **98**, 1–4 (2007).

13. Scholes, G. D. Long Range Resonance Energy Transfer in Molecular Systems. *Annu. Rev. Phys. Chem.* **54**, 57–87 (2003).

14. Scholes, G. D. Quantum-coherent electronic energy transfer: Did nature think of it first? *J. Phys. Chem. Lett.* **1**, 2–8 (2010).

15. Gerritsen, H. & Biophysics, M. Förster Resonance Energy Transfer.

16. Stewart, M. H. *et al.* Complex Förster Energy Transfer Interactions between Semiconductor Quantum Dots and a Redox-Active Osmium Assembly. **6**, 5330–5347 (2012).

17. Braslavsky, S. E. *et al.* Pitfalls and limitations in the practical use of Förster's theory of resonance energy transfer. *Photochem. Photobiol. Sci.* **7**, 1444–1448 (2008).

18. Sedlak, M. & Republic, S. What can be seen by static and dynamic light scattering in polyelectrolyte solutions and mixtures? *Langmuir* **15**, 4045–4051 (1999).

19. Tscharnuter, W. Photon Correlation Spectroscopy in Particle Sizing. *Encycl. Anal. Chem.* 5469–5485 (2000). doi:10.1002/9780470027318.a1512

20. Scotti, A. *et al.* The CONTIN algorithm and its application to determine the size distribution of microgel suspensions. *J. Chem. Phys.* **142**, 234905 (2015).

21. Kynde, S. A. R. *et al.* Small-angle scattering gives direct structural information about a membrane protein inside a lipid environment. *Acta Crystallogr. Sect. D*

Biol. Crystallogr. **70**, 371–383 (2014).

22. Zemb, T. & Diat, O. What can we learn from combined SAXS and SANS measurements of the same sample containing surfactants? *J. Phys. Conf. Ser.* **247**, (2010).

23. Behzadi, N. B. & Sharifi, S. Light scattering and SAXS of spherical to cylindrical transition of AOT/H2O/cyclohexane/PI. *Phys. Chem. Liq.* **52**, 428–435 (2014).

24. Weyerich, B. & Glatter, O. Small-angle scattering of interacting particles . II . [2] Generalized indirect Fourier transformation under consideration of the effective structure factor for polydisperse systems. (1999). doi:10.1107/S0021889898011790

25. Glatter, O.; Kratky, O. *Small Angle X-ray Scattering*. (Academic Press, 1982).

26. Fritz, G., Bergmann, A. & Glatter, O. Evaluation of small-angle scattering data of charged particles using the generalized indirect Fourier transformation technique. *J. Chem. Phys.* **113**, 9733–9740 (2000).

27. Fritz, G. & Glatter, O. Structure and interaction in dense colloidal systems: Evaluation of scattering data by the generalized indirect Fourier transformation method. *J. Phys. Condens. Matter* **18**, (2006).

28. Iampietro, D. J., Brasher, L. L., Kaler, E. W., Stradner, A. & Glatter, O. Direct Analysis of SANS and SAXS Measurements of Catanionic Surfactant Mixtures by Fourier Transformation. *J. Phys. Chem. B* **102**, 3105–3113 (1998).

29. Fritz, G. *et al.* Structure and interaction in dense colloidal systems : evaluation of scattering data by the generalized indirect Fourier transformation method Structure and interaction in dense colloidal systems : evaluation of scattering data by the generalized indirect Fourier transformation method. (2006). doi:10.1088/0953-8984/18/36/S14

30. Valentini, M. *et al.* Diffusion NMR Spectroscopy for the Characterization of the Size and Interactions of Colloidal Matter : The Case of Vesicles and

Nanoparticles. 2142–2147 (2004). doi:10.1021/ja037247r

31. Groves, P. Diffusion ordered spectroscopy (DOSY) as applied to polymers. *Polym. Chem.* **8**, 6700–6708 (2017).

Chapter 2

Exciton Transfer and Emergent Excitonic States in Oppositely Charged Conjugated Polyelectrolyte Complexes

Abstract

Photosynthetic organisms have mastered the use of "soft" macromolecular assemblies for light absorption and concentration of electronic excitation energy. Nature's design centers on an optically-inactive protein-based backbone that acts as a host matrix for an array of light-harvesting pigment molecules. The pigments are organized in space such that excited states can migrate between molecules, ultimately delivering the energy to the reaction center. Here we report our investigation of an artificial light-harvesting energy transfer antenna based on complexes of oppositely charged conjugated polyelectrolytes (CPEs). The conjugated backbone and the charged sidechains of the CPE lead to an architecture that simultaneously functions as a structural scaffold and an electronic energy "highway". We find that the process of ionic complex formation leads to a remarkable change in the excitonic wavefunction of the energy acceptor, which manifests in a dramatic increase in the fluorescence quantum yield. We argue that the extended backbone of the donor CPE effectively templates a planarized acceptor polymer, leading to excited states that are highly delocalized along the polymer backbone.

2.1 Introduction

Over billions of years, natural organisms such as bacteria and plants have evolved the exceedingly complex, supramolecular light-harvesting machinery to ensure efficient conversion of sunlight to chemical potential energy.[1-4] Given the nearly inexhaustible source of solar photons and the success of natural photosynthesis, light-harvesting architectures based on the general principles employed by Nature are attractive for solar generation of chemical fuels. This involves directionally funneling photogenerated electronic excited states (excitons) to a molecular interface, where generation of electron/hole pairs and their subsequent spatial separation takes place. Upon separation, charges cascade down an electron transport chain to the protein assemblies that subsequently drive fuel-generating biochemical reactions.[5]

The elegance of natural supramolecular organization and its associated efficiency of light harvesting inspires us to mimic this photosynthetic machinery in the laboratory. We seek to construct a *modular*, "soft" artificial photosystem capable of efficient light absorption, electronic energy transfer (EET) and long-lived charge generation. This goal requires creating a supramolecular assembly with subunits capable of carrying out the above photophysical processes. To increase the effective absorption cross-section of the photosystem, Nature uses an array of peripheral proteins that serve as an optically-inactive structural scaffolding for pigment molecules. These complexes are collectively known as light-harvesting antennae (LHA). Excitons generated in pigments within LHA are directionally funneled via a combination of coherent and incoherent EET to a "reaction center", where the exciton

is energetically trapped prior to generation of electron/hole pairs via electron transfer. Thus, efficient EET is of paramount importance for LHA function.[4, 6-9]

A large body of work exists describing the synthesis of covalently-linked LHA and reaction centers. Fairly large porphyrin arrays coupled to fullerene electron acceptors,[10-13] as well as more exotic systems containing built-in energy gradients have been prepared to date,[14] among many others. However, it has been recognized that modularity in Nature is key for successful photosystem function.[2] Thus, self-organization appears to be a more attractive avenue for construction of "soft" photosystems. This is because assembly of modular subunits allows for greater flexibility and optimization of the individual parts, as opposed to the need to synthesize the entire collection "from scratch" if the system must be altered in one or more of its functions to suit a particular energetic, structural or stability requirement.

A particularly attractive candidate to serve as the cornerstone for a supramolecular LHA assembly is the conjugated polyelectrolyte (CPE) – an amphiphilic polymer with a conjugated backbone and ionized (or ionizable) sidechains.[15] Due to their π-electron-rich backbones and ionic sidechains, CPEs hold great promise as electronic energy highways and macromolecular scaffolds.[16-19] The electrostatic coupling leads to strong interactions, while controlling the charge density allows for tuning the cooperative strength of this interaction. Furthermore, the strong influence of the backbone microstructure on its optoelectronic properties, as well as sensitivity to the local electric field, allows one to tune the environment to control EET, akin to how the polypeptide scaffolding environment can tune the energy levels of natural pigments. Using CPEs in light-harvesting assemblies largely obviates the

need for an optically inactive scaffolding, thereby raising the density of subunits that directly contribute to excited state generation.

In this manuscript, we describe assembly of oppositely charged CPEs as LHA with complementary electronic absorption and emission spectra, resulting in thermodynamically-allowed EET between the complexed CPEs. To the best of our knowledge, this is the first time that a multi-CPE complex assembly in solution has been studied. We show that both in solution and the solid state, oppositely-charged CPEs readily form ionic complexes that undergo inter-CPE EET. Further, we show that complex formation drastically modulates the nature of the emitting excitonic wavefunction relative to isolated CPEs. Our results demonstrate that oppositely charged complexes of donor/acceptor CPEs display rich photophysics and intriguing assembly behavior, underscoring the potential of these materials to function as tunable exciton relays for LHA applications.

2.2 Experimental Methods

2.2.1 Sample Preparation

The cationic conjugated polyelectrolyte poly([fluorene]-alt-co-[phenylene]) (PFPI) with an average molecular weight (MW) of 21,000 Da and polydispersity index (PDI) of 1.2 was obtained from Solaris Chem Inc. The anionic conjugated polyelectrolyte poly(alkylcarboxythiophene) derivative (PTAK) with an MW of 16,000 Da and a PDI of 2.2 was obtained from Rieke Metals. Both materials were used as received.

Stock Solutions of PFP3I and PTAK (10.0 mg/mL) were prepared in Milli-Q water and then mixed in desired molar ratios to form CPECs. The PTAK stock solution was stirred at ~ 70 °C for 24 hours. The PFPI stock solution was stirred at ~ 55 °C for 72 hours. Care was taken to minimize exposure to ambient lights. CPEC solutions with PFPI:PTAK charge ratios of PFPI to PTAK (1 : 0.01, 1 : 0.05, 1 : 0.25) were prepared based on the number of chargers per monomer unit. The PFPI monomer carries a charge of 2+, and the ionized PTAK monomer carries a 1- charge. The PFPI concentration was fixed at 1 mg/mL for all CPEC solutions. The forward addition method is as follows. PFPI from the stock solution was added to Milli-Q water, after which PTAK stock was added dropwise to the solution while stirring at room temperature to achieve the desired charge ratio. The order of CPE addition is switched in the reverse order. CPEC solutions were then stirred at ~ 55 °C for 24 hours. In solutions with a solid/liquid phase coexistence, mixtures were centrifuged at 3400 rpm for 30 minutes, after which the phases were separated for further measurements.

2.2.2 Steady-State Spectroscopy

Optical density measurements were taken in 1.0 nm increments with a Shimadzu UV-2700 Spectrophotometer with an integration time of 0.1 seconds and a 2.0 nm slit width over the range of 300-800 nm. Photoluminescence measurements were taken using a Horiba Fluromax-4 spectrofluorometer in a right-angle geometry in cuvettes with 1mm pathlengths, with excitation wavelengths scanned in 5.0 nm increments and emissions measured in 1.0 nm increments over the range of 300-800

nm. Liquid samples were measured with a Rayleigh masking slit width of 5.0 nm and an integration time of 0.1 seconds. Solid samples were placed at an 87° angle relative to the incident beam and measured with a Rayleigh masking slit width of 2.0 nm and an integration time of 0.05 seconds.

2.2.3 Dynamic Light Scattering (DLS)

Solutions were filtered using 0.65 μm Millipore filter directly into borosilicate glass test tubes. Samples were immersed in decalin to match the index of refraction of glass (n ~ 1.33). All DLS measurements were made on a Brookhaven BI-200SM goniometer system using a TurboCorr Photon Counter and digital correlator at room temperature. The light source was a CW Mini-L30 solid-state diode laser outputting 637 nm light with adjustable power limited to 35 mW. The laser power and optical density filter were adjusted in order not to exceed a signal intensity of 200 kilocounts per second. Scattered photons were detected by an avalanche photodiode detector. The normalized intensity correlation functions were transformed to the normalized electric-field field correlation function using the Siegert regulation. The field correlation functions were analyzed using CONTIN, which is a regularized inverse Laplace transform algorithm originally written in FORTRAN by Provencher and since emulated by Marino in MATLAB. Distribution of relaxation times were obtained for scattering angles of 20 and 90 degrees with the regulation parameter (α) set to 0.1. Various choices for α as well as various grid densities for the relaxation time space were explored. We found that relaxation times obtained with different choices of α were similar. A larger value of α was avoided so as to not overly smooth

the relaxation time distribution. Hydrodynamic radius values were obtained using the Stokes-Einstein equation.

2.2.4 Small-Angle X-ray Scattering (SAXS)

SAXS measurements were performed at beam line 4-2 at the Stanford Synchrotron Radiation Laboratory (SSRL) using a Rayonix MX225-HE detector. Samples in thin-wall quartz capillary cell were irradiated by a 11 keV X-ray (1.17 Å) at a sample to detector distance of 3.5m. A set of 10 consecutive 1 second X-ray exposures were made on each sample at room temperature. The scattering of the background (Milli-Q water) was subtracted from solution scattering. To avoid degradation, the samples were oscillated during data collection. SasTool, a software package developed at SSRL, was used to convert collected 2D TIFF images to intensity vs scattering vector and to subtract solvent scattering.

Time-Resolved Photoluminescence Spectroscopy

Time-correlated single photon counting (TCSPC) was carried out on a home-built apparatus. The excitation source was a pulsed Super K EXTREME (NKT Photonics) supercontinuum laser coupled to a Super K SELECT (NKT Photonics) acousto-optic filter and external RF driver (NKT Photonics) to select the wavelength of the excitation pulse. Measurements were carried out at a 78MHz pulse repetition rate with either 15.4μW (420nm) or 97.6μW (600nm) power, as measured near the sample. Both excitation and emission beams were horizontally polarized by mounted Glan-Thompson polarizers (Thorlabs). Emission light was collimated and refocused by a set of achromatic doublets (Thorlabs). Long pass filters were used to minimize

the influence of the reflected excitation beam. Emission wavelengths were selected by an Acton Spectra Pro SP-2300 monochromator (Princeton Instruments), on which two detectors were mounted for steady-state and time-resolved measurements. An air-cooled PIXIS 100 CCD (Princeton Instruments) was used to record the steady-state spectra on the fly. A hybrid PMT with minimal after-pulsing (Becker and Hickl) was used to record the time-resolved fluorescence decay. An SPC-130 photon counting module (Becker and Hickl) coupled to a Simple-Tau 130 table top TCSPC system was used for photon counting. Emitted photons were collected for 5 seconds, and each measurement was repeated 50 times prior to averaging and subsequent analysis.

2.3 Results and Discussion

This investigation focuses on an oppositely charged pair of CPEs, the chemical structures of which are shown in **Figure 2.1A**. The iodide salt of the cationic poly(fluorene-co-phenylen) (PFPI) derivative serves as the excitonic donor, and the potassium salt of an anionic, regioregular poly(thiophene) (PTAK) derivative acts as the energy acceptor. **Figure 2.1B** shows that the emission spectrum of PFPI spectrally overlaps the optical density (OD) of PTAK, indicating that energy transfer is thermodynamically allowed. Since both CPEs emit readily detectable photoluminescence (PL), and because the chain microstructure is strongly coupled to the polymer photophysics, PL spectroscopy forms the basis for this investigation. Aqueous CPE concentrations were chosen to be large enough so as to observe phase

separation beyond a critical polycation/polyanion charge ratio, allowing us to compare the photophysics of the liquid and solid phases.

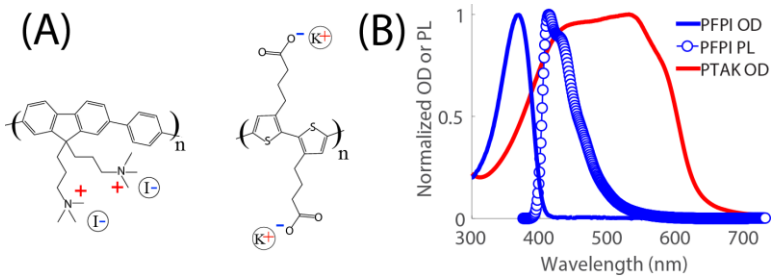

Figure 2.1~~2~~ (A) Chemical structures of PFPI (left) and PTAK (right). (B) Optical density (OD) and photoluminescence (PL) of PFPI and PTAK solutions. The overlap of PFPI PL with OD of PTAK indicates that excitons can undergo energy transfer from the excited PFPI donor to the PTAK acceptor.

Figure 2 shows steady-state PL contour maps with excitation and emission wavelengths plotted vertically and horizontally, respectively, of both isolated CPE solutions and their mixed solutions. The PL map of 1 mg/mL PFPI is shown in **Figure 2.1A**. As expected, the PL intensity is concentrated in the region that corresponds to strong PFPI absorption, as shown in **Figure 2.1**. However, because of the very large extinction coefficient of PFPI, at these concentrations the PL map appears as two PL bands as a function of excitation wavelength (λ_{ex}). This is a consequence of the fact that PL intensity was collected at 90° with respect to the excitation beam, resulting in imperfect spatial overlap of PL signal due to excitations

near the OD peak with the capture cross-section of the detector.

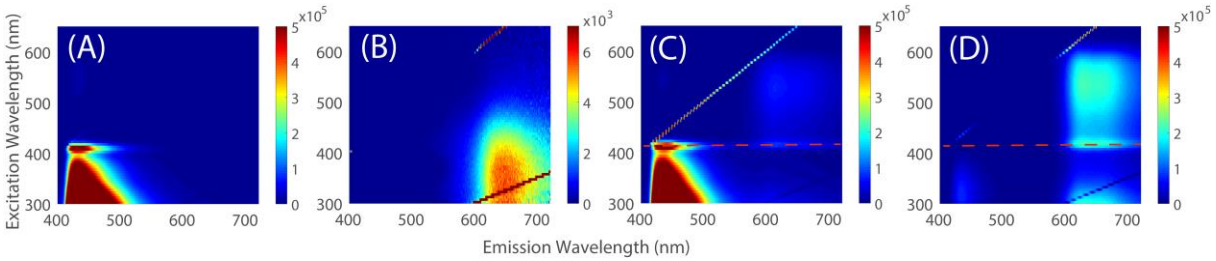

Figure 2.2 Aqueous solution 2D PL maps of (A) PFPI at 1 mg/mL, (B) PTAK mole-matched to the 1:0.25 charge ratio CPEC, (C) 1:0.01 PFPI:PTAK CPEC, and (D) 1:0.25 CPEC. The bright pixels falling on a diagonal line in the upper left corner are due to reflections of the excitation wavelength. The red dashed, horizontal line in (C) and (D) indicates the excitation wavelength that gives rise to PFPI emission and to simultaneous PTAK emission. The sharp enhancement of the latter cannot be explained by the PTAK absorption spectrum, indicating evidence of EET from PFPI to PTAK. The same enhancement is seen at lower excitation wavelengths as well. Though isolated PTAK emits in this region as well, in a CPEC this PTAK PL is drastically more intense, as indicated by the change in scale between (B) and (D).

Figure 2.2B shows PL due to an aqueous PTAK solution at a concentration matched to the PFPI:PTAK complex at the 1:0.25 molar charge ratio (**Figure 2.2**). A contrast scale that was different from the rest of the samples had to be used for this particular sample due its very low PL intensity; in fact, at these instrumental parameters, PL from lower concentration solutions was barely measurable. In addition to the observation that PTAK solutions fluoresce weakly, it is important to note that there is negligible PL arising at λ_{ex} that give rise to peak absorption. In this context, it is worth mentioning that the *solution* absorption spectrum of PTAK is quite similar to that of a *thin film* of neutral, regioregular poly(3-hexylthiophene) – a well-studied poly(thiophene) derivative, P3HT – which is also known to have low PL quantum yields.[20-23]

Figure 2.2C and **Figure 2.2D** show PL maps from solutions of oppositely-charged CPE complexes (CPECs) at the specified polycation:polyanion molar charge ratios. Here, the PFPI concentration has been fixed at 1 mg/mL, and the charge ratio is varied by varying the concentration of PTAK. The 2D PL map for the 1:0.01 CPEC (Figure 2C) shows the characteristic PFPI emission band, but in addition, the PTAK region at emission wavelengths (λ_{em}) > 550 nm now also shows several PL bands. First, there is PTAK PL peaked in a narrow λ_{ex} range corresponding to the excitation of low-energy PFPI chromophores; as such, this PTAK band falls on the same horizontal line (λ_{ex} = constant) as PFPI, labeled with a red dashed line. Second, there is measurable PL coming from PTAK throughout its absorption band. Control PTAK solution at this concentration do not show any intensity on this contrast scale.

When the charge ratio is further increased to 1:0.25, the solution phase separates into a liquid phase and a dense CPE network phase, which resembles a loose precipitate. **Figure 2.2D** shows the PL of the solution phase at this charge ratio. The Figure shows that PFPI PL has been substantially quenched. Concomitantly, PTAK PL is substantially enhanced both over the λ_{ex} that give rise to PFPI PL. Additionally, PTAK PL arising from the bulk of its absorption (λ_{ex} > 450 nm) is now quite strong, in stark contrast to the weak PL from the control PTAK solution at the same nominal concentration (Figure 2B).

To understand the difference between the steady-state PTAK photophysics in isolation vs. as part of a CPEC, we have displayed representative OD spectra of PTAK in isolation vs. in the complexed state in **Figure 2.3A**. Both samples show comparable OD magnitudes; however, there are notable differences. The isolated

PTAK spectrum is slightly red-shifted relative to the CPEC, and the latter has enhanced oscillator strength over the main excitonic absorption band.

To quantify differences in PL intensities between the different PTAK samples, Figure 3B shows the PL excitation (PLE) spectrum for different charge ratios *exclusively in the PTAK emission region*, generated by plotting the PL intensity at λ_{em}

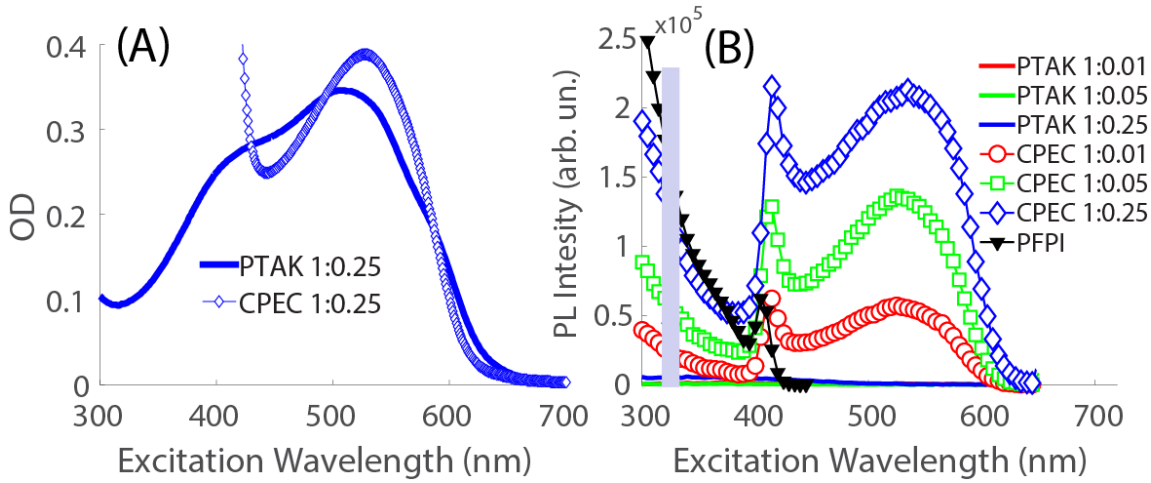

Figure 2.3 (A) OD of isolated PTAK and PTAK complexed to PFPI (CPEC) at the same nominal PTAK concentrations. (B) PL excitation (PLE) spectra collected at an emission wavelength that exclusively corresponds to PTAK PL. For comparison, PLE of PFPI in a CPEC (collected near PFPI PL peak and scaled for clarity) is also shown with black filled diamonds. The PLE intensity of PTAK complexed to PFPI is orders of magnitude larger than that of PTAK on its own. The enhancement in complexed PTAK's PL at wavelengths that correspond to PFPI PL yet do not correspond to sharp PTAK OD features is strong evidence of inter-CPE EET from photoexcited PFPI to PTAK. The grey bar masks the specular reflection of the excitation light.

close to the peak of the PTAK emission spectrum as a function of λ_{ex}. In the CPEC, there is clear enhancement in PTAK PL precisely at λ_{ex} that give rise to strong PL from PFPI (black diamonds; also seen in Figures 2A and 2C), both at the relatively

sharp band at λ_{ex} ~ 420 nm and at lower wavelengths. This enhancement in PTAK's PL precisely at λ_{ex} that give rise to strong PFP PL is even more clear at lower concentrations, due to a more uniform spatial distribution of excited states.. The combination of the following observations constitutes strong evidence of EET from PFPI to PTAK: a) PTAK PL enhancement tracks the PFPI PLE intensity as a function of λ_{ex}; b) PFPI emission is progressively quenched with increasing PTAK concentrations. This then directly implies that oppositely-charged PFPI and PTAK readily form a supramolecular complex in aqueous solution, leading to efficient EET from the donor to the acceptor CPE. Photoexcited electron transfer from PFPI to PTAK can be ruled out as a primary quenching mechanism for PFPI PL, as this would produce electron polarons on PTAK that would not give rise to enhanced PL.

Closer inspection of **Figure 2.3B** shows a striking result: The PTAK PL intensity in isolation is approximately two orders of magnitude lower than that of PTAK in a CPEC solution. To elucidate what is responsible for such a drastic difference in PL quantum yields, in **Figure 2.4** we have plotted normalized PTAK emission spectra exciting at λ_{ex} = 450 nm. This λ_{ex} was chosen because at longer wavelengths, the very weak PL signal to noise ratio of isolated PTAK becomes too low for quantitative analysis, though the same trends persist regardless of λ_{ex}.

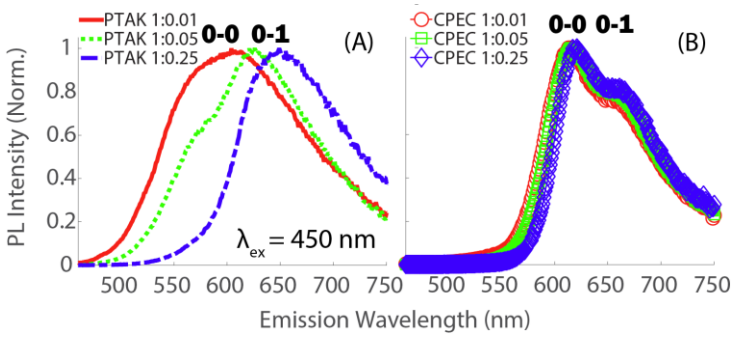

Figure 2.4 Normalized PL of PTAK in isolated aqueous solution (A) vs. that of the CPEC (B) exciting at 450 nm. The data show that the apparent 0-0/0-1 vibronic ratio differs substantially between the same CPE in different environments: < 1 in isolation and > 1 in the CPEC.

Figure 4A shows PL spectra of control PTAK solutions, and Figure 4B shows emission spectra from CPEC solutions corresponding to the same nominal PTAK concentrations as the controls in (A). 0-0 and 0-1 vibronic peak positions are labeled in bold. **Figure 2.4A** demonstrates that the apparent 0-0/0-1 peak ratio is less than unity for all three PTAK concentrations (corresponding to the three CPEC charge ratios), and the ratio progressively decreases with concentration. We interpret the peak red shift with increasing concentration as a signature of enhanced inter-chain π-stacking. In stark contrast, the apparent 0-0/0-1 ratio is larger than unity for PTAK when it is complexed to PFPI (**Figure 2.4B**), with a negligible change as the PTAK concentration is increased.

To understand emission spectra from conjugated polymers, the molecular exciton model, developed for dye aggregates by Kasha[24] and extended to polymers by others has been found to be particularly useful. Within this model, the 0-0/0-1

vibronic ratio < 1 in chromophore aggregates is associated with H-type excitons, which have low emission quantum yields. We interpret the weak emission from isolated PTAK solutions with a 0-0/0-1 ratio < 1 as arising from predominantly H-like emitting states, which are primarily physically associated with π-stacked inter-chain species.[25] The latter might arise due to interactions between separate chains or between two or more distinct segments of the same coiled chain. This interpretation is consistent with the observation that the absorption spectrum of isolated PTAK is similar to that of a P3HT film. Such absorption in P3HT has previously been shown to give rise to H-like emitting states.[23, 26]

On the other hand, a 0-0/0-1 ratio approximately equal to or greater than unity is primarily associated with excitons having substantial J-like character, and which give rise to strongly allowed light emission.[27] When complexed to PFPI, the fact that PTAK PL spectra show nominal 0-0/0-1 ratios ~ 1, and the fact that the PL intensity is several orders of magnitude larger in the complexed state, leads us to conclude that within a CPEC, PTAK excitons are primarily J-like. Thus, oppositely-charged complex formation leads to *emergent excitonic states* in the regioregular PTAK that are wholly absent for the EET acceptor CPE in isolation.

To further test this interpretation, we have measured time-resolved PL (TRPL) via time-correlated single-photon counting. **Figure 2.5A** shows the TRPL decays on a semi-logarithmic scale of a pure PFPI solution along with CPECs and PTAK controls excited at 420 nm with emission collected at 442 nm, which corresponds to the peak of the PL spectrum of PFPI. We find that for the lowest charge ratio CPEC, there is a moderate yet significant drop in intensity, which tracks the steady state PL. A blowup

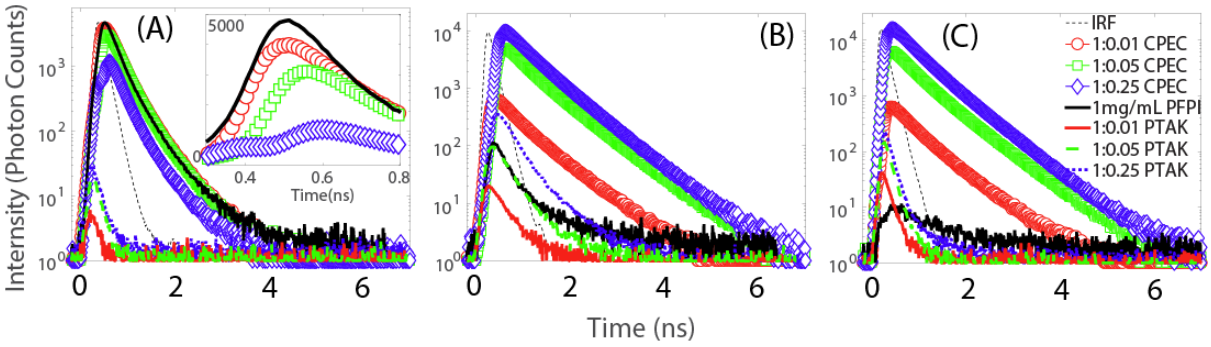

Figure 2.5 Time-resolved PL decays (collected for the same duration) of CPECs at varying polyion charge ratios as well as pure CPE solution controls prepared at concentrations corresponding to their respective CPEC solutions. The legend is shown on the far right; pure PTAK controls are labeled with the corresponding CPEC chare ratio. The instrument response function (IRF) is shown as a thin dashed line in all panels. (A) λ_{ex} = 420 nm and λ_{em} = 442 nm. Emission is collected near the peak of PFPI PL. The inset shows PFPI and CPEC solutions plotted on a linear scale. The data show that PFPI PL is progressively quenched with increasing relative charge ratio, which we attribute to EET from PFPI to PTAK. (B) λ_{ex} = 420 nm and λ_{em} = 615 nm. Emission at the latter comes overwhelmingly from PTAK. The curves show that upon complexation with PFPI, PTAK emission intensity increases by ~ two orders of magnitude and lasts substantially longer than that of pure PTAK. We attribute this to emergence of extended, J-like excitonic states largely delocalized over the conjugated PTAK backbone. (C) λ_{ex} = 600 nm and λ_{em} = 680 nm. In this case, the lowest-energy excitons of PTAK are excited with vanishing PFPI excitation. Similar to the data shown in (B), the decays display long-lived PL and are due to delocalized J-like excitons.

of this data on a linear scale is shown in the inset.

At the two higher ratios, there is pronounced quenching of the PFPI emission, consistent with steady-state results. **Figure 2.5B** shows TRPL decays excited at the same λ_{ex} but with emission detected at 615 nm, strictly corresponding to PTAK PL. This panel shows that across all PTAK concentrations, there is a drastic increase in the intensity of emission from the CPEC relative to the corresponding PTAK controls. The increase in fluorescence is several times greater than what would be expected just from the increase in total polymer concentration in solution. While this change in total fluorescence intensity tracks the decrease in CPEC fluorescence at 442 nm (quenching of PFPI emission), the fractional changes in the magnitudes are not similar. In fact, the increase in fluorescence at 615 nm between concentrations is approximately 5-10 times larger than the associated decrease in PFPI emission, depending on the sample. Thus, in addition to EET, the increase in the PL lifetime of PTAK bound to PFPI is again consistent with emission from J-like states.

Finally, to better understand the PL that comes from PTAK excitons generated in the red tail of the CPEC absorption - corresponding to the most delocalized excited states - **Figure 2.5C** displays TRPL curves collected at λ_{ex} = 600 nm and λ_{em} = 680 nm. As in **Figure 2.5B**, we again see that the total fluorescence of the CPECs far exceeds what would be expected just by increasing the total polyelectrolyte concentration. This suggests that whether excited by energy transfer from PFPI or excited directly, PTAK excitons are relaxing through the same highly emissive J-like excitons. Therefore, complexation appears to preclude strong formation of intra- and inter-chain H-aggregation, leading to J-like states instead.

In an effort to connect the photophysics to the physical structure of the complexes, we have characterized CPECs at varying charge ratios using both dynamic (visible) light scattering (DLS)[28-30] and small-angle X-ray scattering[31-32] (SAXS). In DLS measurements, we collected self-beating intensity autocorrelation functions[33] (ACFs) $g^1(t)$ at scattering angles of 20°. **Figure 2.6** shows a composite ACF plot of CPEC solutions at varying charge ratios, as well as relaxation time distribution functions obtained using the CONTIN algorithm, which performs a regularized inverse Laplace transform.[34]

DLS relaxation times, associated diffusion coefficients and mean hydrodynamic radii are summarized in **Table 2.1**. Inspection of **Figure 2.6** demonstrates that the mean relaxation time for the lowest charge ratio is longest, which means that the mean size is largest. The 1:0.01 charge ratio yielded a predominantly bimodal distribution with two characteristic particle sizes, the smaller

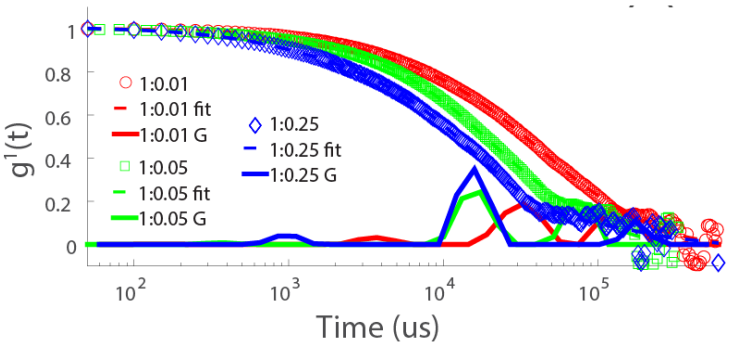

Figure 2.6 Normalized DLS electric field autocorrelation functions for CPEC solutions collected at a 20° scattering angle. Circles correspond to data, dashed lines to CONTIN-generated fits, and solid lines to relaxation time distribution times obtained from CONTIN, labeled in the legend as G.

of which was 87 nm. Particles corresponding to the smaller of the two sizes shrank progressively with increasing charge ratio to 46 nm at 1:0.05 and 42 nm at 1:0.25. Additionally, we find that for all three charge ratios, we observe large particle sizes in excess of 100 nm. These results imply that as more PTAK is added to PFPI, the mean complex size progressively shrinks as charges on one polymer are compensated by its oppositely charged partner. This is possibly due to a propensity to lower the interfacial area between the hydrophobic conjugated backbones of the CPEs and the highly polar solvent as the effective charge density of the complex diminishes. The decrease in size is consistent with a slight red shift in PTAK PL when complexed to PFPI (Figure 4B), which we attribute with a mild increase in inter-chain π-stacking.

Table 2.1 CONTIN fit results of DLS autocorrelation functions from CPEC solutions at two scattering angles.

PFP3I:PTAK Molar Charge Ratio	Relaxation time (us)	R_H (nm) [a]	Relative Size Distribution (%)
1:0.01	3.3×10^4	87	47.4
1:0.01	3.7×10^3	10	7.9
1:0.01	1.3×10^5	342	44.7
1:0.05	1.7×10^4	46	55.6
1:0.05	6.8×10^4	180	44.4
1:0.25	1.6×10^4	42	76.4
1:0.25	1.7×10^5	462	23.7

[a] Intensity-weighted hydrodynamic radius from dynamic light scattering.

To characterize the electron density contrast between water and CPECs as a function of charge ratio, we carried out synchrotron solution SAXS measurements. These results are shown in **Figure 2.7** on a double logarithmic plot, where we compare pure PFPI to that of the CPECs for both addition orders. We find that all the

curves except the 1:0.25 CPEC exhibit similar limiting power law exponents at high *Q*, suggesting that interfaces internal to the CPE coil do not differ substantially between pure PFPI and CPECs at the lower charge ratio. At 1:0.25, the decrease in the slope could possibly be due to a more fractal internal geometry, though a more

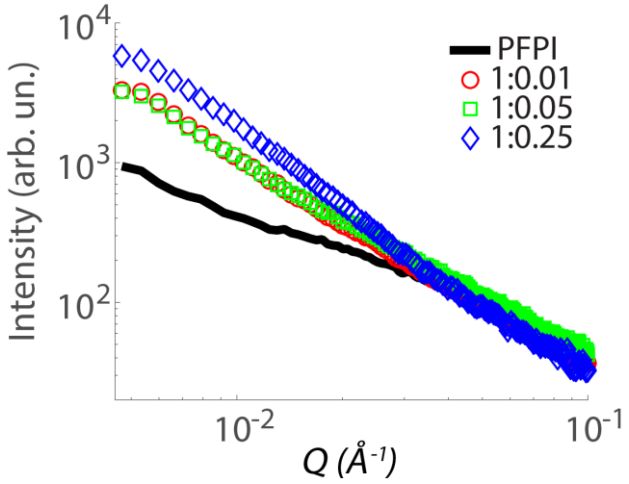

Figure 2.7 SAXS intensities vs. scattering vector *Q* for 1 mg/mL PFPI solution (solid black) and CPEC solutions at 1:0.01 (red circles), 1:0.05 (green squares) and 1:0.25 (blue diamonds) charge ratios.

systematic investigation of this observation is beyond the scope of this paper.

At low *Q*, however, all CPEC curves show an excess in scattering intensity relative to pure PFPI. This is reasonable, since when the oppositely charged CPEC forms, we expect that the electron density contrast between pure solvent and the complex will be larger than that of the isolated CPE. Curves for 1:0.01 CPECs can be roughly captured with a single power law decay. In 1:0.05 CPECs curves begin to

depart from a power law as they show signs of a developing (yet relatively poorly-defined) Guinier region at low *Q*. At the 1:0.25 ratio, the SAXS curve displays a hint of Guiner behavior, indicating formation of a more well-defined CPEC particle shape relative to pure PFPI and the lowest charge ratio complex. Taken together with DLS results, this suggests that the decrease in mean particle size at larger charge ratios leads to solution complexes with greater packing density, as implied by the rise in scattering intensity at low *Q*.

Having characterized CPEC solutions, we now turn to examining the dense CPEC network phase. Phase separation occurs at charge ratios exceeding 1:0.05. The dense phase was spread on a glass substrate as a paste and allowed to dry prior to collecting PL, which is shown in Figure 8 for two charge ratios. The first striking feature is that PL from PFPI is effectively absent, save for a weak band at the PFPI:PTAK charge ratio of 1:0.25. There is a pronounced enhancement in PL from PTAK when exciting between ~ 320 and 420 nm. This corresponds well to the OD of PFPI; however, PTAK has (relatively low) absorption in this region as well, and isolated PTAK solutions also showed PL when exciting in this region. It is worth noting that a pure spin-coated PTAK film does not give rise to measurable PL (not shown), which is in contrast to the CPEC films shown in **Figure 2.8**.

Although we cannot rule out direct excitation of PTAK and its subsequent emission as contributing to PTAK's PL in the 320-420 nm excitation region, there are several observations that suggest that this PL at least partially contains emission from PTAK excitons that are populated directly as a result of EET from PFPI in the solid state. First, the enhancement of PTAK PL at these λ_{ex} differs qualitatively from the

solution PL shown in **Figure 2.3**. Second, if this PL was simply due to pure PTAK, we would expect strong self-quenching, as we observed in spin-coated PTAK films; this is not the case. Third, **Figure 2.1A** shows that there is an additional enhancement in PTAK PL in the 1:0.063 ratio film at λ_{ex} ~ 410 nm, which resembles solution behavior. Taken together, we believe that a fairly significant fraction of PTAK PL originating from λ_{ex} between 320 nm and 420 nm is due to direct EET from PFPI to PTAK.

In both films shown in Figure 8, λ_{ex} between 450 nm and 600 nm corresponds to a PL band that appears to roughly track the absorption spectrum of CPEC thin films. The fact that this PL persists for both charge ratios suggests that these PTAK chains are strongly associated with PFPI. These observations again suggest that PTAK chains preferentially associate with PFPI, and inter-PTAK π-stacking is not prevalent.

Thus it is clear that both solution and the solid state, PFPI and PTAK readily form ionically bound complexes, which exhibit EET from PFPI to PTAK. We have

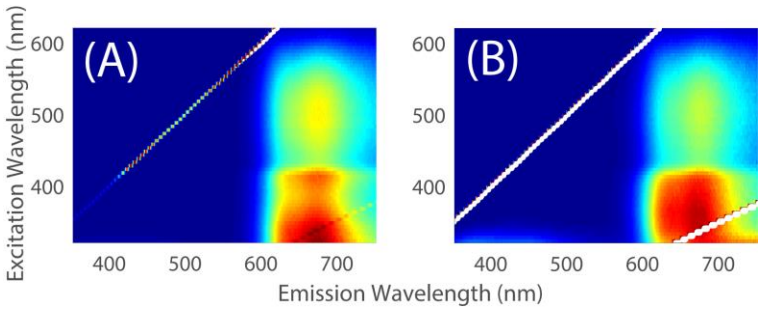

Figure 2.8 2D PL maps of the solid CPEC dense phase isolated from CPEC solutions of varying polycation/polyanion charge ratios: (A) 1:0.063; (B) 1:0.25. The solid was spread on a substrate as a paste and allowed to dry. PFPI PL is nearly completely quenched, and PTAK PL is enhanced in the excitation region corresponding to strong PFPI emission when PFPI is in isolation.

also shown that in solution, PTAK excitons are converted from H-like to J-like in the process of complexation with PFPI. With increasing charge ratio, the average complex size shrinks, but the primary J-like excitonic states remain. According to work by Spano *et al.* and Barford *et al.*, J-like excitons in conjugated polymers are primarily viewed as arising from head-to-tail arrangements of transition dipoles localized on each monomer unit, which together add in phase.[22, 24, 27, 35-36] In the limit of vanishing disorder, this leads to excitons highly delocalized over a single polymer chain. If multiple relatively straight chains are in proximity, excitons are expected to exhibit both J-like and H-like character. In the context of this model, we interpret J-like emission from PTAK within a CPEC as arising from excitons largely delocalized over a single chain akin to a 1D molecular wire in the low disorder limit. A cartoon of

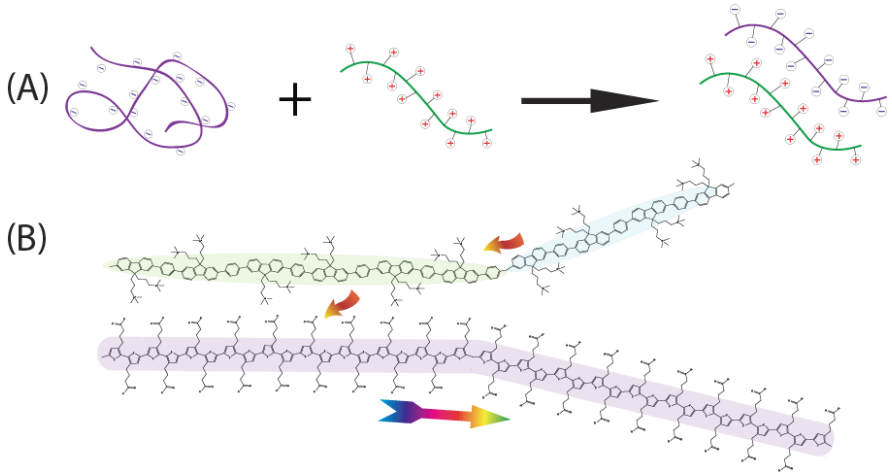

Figure 2.9 (A) Cartoon illustrating the change in PTAK chain microstructure going from isolated solution to the CPEC. The result is a planarization of the PTAK backbone relative to isolated solutions. (B) Cartoon of PFPI and PTAK chains in a solution-phase CPEC. The backbones of both CPEs are fairly extended, leading to coherent excitonic wavefunction delocalization over a large backbone segment. One consequence of this backbone planarization due to CPEC formation is a drastic increase in the PL quantum yield of PTAK (bottom CPE), consistent with emission from J-like excitonic states. Arrows indicate directional transfer of electronic energy.

this is shown in **Figure 2.9**. This result is very intriguing, as the highly delocalized nature of the intra-chain J-like exciton will lead to facile electronic energy migration down the chain and may additionally result in an interplay between coherent and incoherent EET. The former has been observed for conjugated polymers in room temperature solution.[37] Such a combination of EET mechanisms has been invoked as possibly being essential for efficient directional funneling of excitons in natural light harvesting systems.[5] These observations underscore the potential that CPEs and their complexes have for light-harvesting antenna applications.

2.4 Conclusions

To conclude, to the best of our knowledge we have reported on the very first preparation and characterization of an oppositely charged conjugated polyelectrolyte complex in aqueous solution capable of electronic energy transfer. We found that the oppositely-charged complex undergoes EET both in solution and the solid state. Importantly, we have also found that the excitonic wavefunction of the accepter polyelectrolyte changed qualitatively in the complex compared to the polyelectrolyte in isolation. This work highlights the fact that a) conjugated polyelectrolyte complexes present highly intriguing photophysics that are in need of fundamental investigation, and b) that modular assemblies of excitonic donor/acceptor conjugated polyelectrolytes hold substantial promise for artificial light harvesting applications.

2.5 References

1. Barter, L. M.; Durrant, J. R.; Klug, D. R. A Quantitative Structure-Function Relationship for the Photosystem II Reaction Center: Supermolecular Behavior in Natural Photosynthesis. *Proc. Natl. Acad. Sci. U S A* **2003**, *100*, 946-51.

2. Croce, R.; van Amerongen, H. Natural Strategies for Photosynthetic Light Harvesting. *Nat. Chem. Biol.* **2014**, *10*, 492-501.

3. McConnell, I.; Li, G.; Brudvig, G. W. Energy Conversion in Natural and Artificial Photosynthesis. *Chem. Biol.* **2010**, *17*, 434-47.

4. Scholes, G. D.; Fleming, G. R.; Olaya-Castro, A.; van Grondelle, R. Lessons from Nature About Solar Light Harvesting. *Nat. Chem.* **2011**, *3*, 763-74.

5. Blankenship, R. E. *Molecular Mechanisms of Photosynthesis*; Wiley, 2014.

6. Fassioli, F.; Dinshaw, R.; Arpin, P. C.; Scholes, G. D. Photosynthetic Light Harvesting: Excitons and Coherence. *J. R. Soc., Interface* **2014**, *11*, 20130901.

7. Olaya-Castro, A.; Scholes, G. D. Energy Transfer from Förster–Dexter Theory to Quantum Coherent Light-Harvesting. *Int. Rev. Phys. Chem.* **2011**, *30*, 49-77.

8. Scholes, G. D. Long-Range Resonance Energy Transfer in Molecular Systems. *Annu. Rev. Phys. Chem.* **2003**, *54*, 57-87.

9. Stirbet, A. Excitonic Connectivity between Photosystem IX Units: What Is It, and How to Measure It? *Photosynth. Res.* **2013**, *116*, 189-214.

10. Bhosale, S. V.; Bhosale, S. V.; Shitre, G. V.; Bobe, S. R.; Gupta, A. Supramolecular Chemistry of Protoporphyrin Ix and Its Derivatives. *Eur. J. Org. Chem.* **2013**, *2013*, 3939-3954.

11. Bottari, G.; Trukhina, O.; Ince, M.; Torres, T. Towards Artificial Photosynthesis: Supramolecular, Donor–Acceptor, Porphyrin- and Phthalocyanine/Carbon Nanostructure Ensembles. *Coord. Chem. Rev.* **2012**, *256*, 2453-2477.

12. Elemans, J. A. A. W.; van Hameren, R.; Nolte, R. J. M.; Rowan, A. E. Molecular Materials by Self-Assembly of Porphyrins, Phthalocyanines, and Perylenes. *Adv. Mater.* **2006**, *18*, 1251-1266.

13. Fukuzumi, S. Development of Bioinspired Artificial Photosynthetic Systems. *Phys. Chem. Chem. Phys.* **2008**, *10*, 2283-97.

14. Hayashi, H.; Sobczuk, A.; Bolag, A.; Sakai, N.; Matile, S. Antiparallel Three-Component Gradients in Double-Channel Surface Architectures. *Chem. Sci.* **2014**, *5*, 4610-4614.

15. Jiang, H.; Taranekar, P.; Reynolds, J. R.; Schanze, K. S. Conjugated Polyelectrolytes: Synthesis, Photophysics, and Applications. *Angew. Chem. Int. Ed. Engl.* **2009**, *48*, 4300-16.

16. Costa, T.; Garner, L. E.; Knaapila, M.; Thomas, A. W.; Rogers, S. E.; Bazan, G. C.; Burrows, H. D. Aggregation Properties of P-Phenylene Vinylene Based Conjugated Oligoelectrolytes with Surfactants. *Langmuir* **2013**, *29*, 10047-58.

17. Evans, R. C.; Knaapila, M.; Willis-Fox, N.; Kraft, M.; Terry, A.; Burrows, H. D.; Scherf, U. Cationic Polythiophene-Surfactant Self-Assembly Complexes: Phase Transitions, Optical Response, and Sensing. *Langmuir* **2012**, *28*, 12348-56.

18. Knaapila, M.; Evans, R. C.; Garamus, V. M.; Almasy, L.; Szekely, N. K.; Gutacker, A.; Scherf, U.; Burrows, H. D. Structure and "Surfactochromic" Properties

of Conjugated Polyelectrolyte (Cpe): Surfactant Complexes between a Cationic Polythiophene and Sds in Water. *Langmuir* **2010**, *26*, 15634-43.

19. Pinto, S. M.; Burrows, H. D.; Pereira, M. M.; Fonseca, S. M.; Dias, F. B.; Mallavia, R.; Tapia, M. J. Singlet-Singlet Energy Transfer in Self-Assembled Systems of the Cationic Poly{9,9-Bis[6-N,N,N-Trimethylammonium)Hexyl]Fluorene-Co-1,4-Phenylene} with Oppositely Charged Porphyrins. *J. Phys. Chem. B* **2009**, *113*, 16093-100.

20. Guo, S.; Ruderer, M. A.; Rawolle, M.; Korstgens, V.; Birkenstock, C.; Perlich, J.; Muller-Buschbaum, P. Evolution of Lateral Structures During the Functional Stack Build-up of P3ht:Pcbm-Based Bulk Heterojunction Solar Cells. *ACS Appl. Mater. Interfaces* **2013**, *5*, 8581-90.

21. Roehling, J. D.; Arslan, I.; Moulé, A. J. Controlling Microstructure in Poly(3-Hexylthiophene) Nanofibers. *J. Mater. Chem.* **2012**, *22*, 2498-2506.

22. Yamagata, H.; Spano, F. C. Interplay between Intrachain and Interchain Interactions in Semiconducting Polymer Assemblies: The HJ-Aggregate Model. *J. Chem. Phys.* **2012**, *136*, 184901.

23. Clark, J.; Chang, J.-F.; Spano, F. C.; Friend, R. H.; Silva, C. Determining Exciton Bandwidth and Film Microstructure in Polythiophene Films Using Linear Absorption Spectroscopy. *Appl. Phys. Lett.* **2009**, *94*, 163306.

24. Spano, F. C.; Silva, C. H- and J-Aggregate Behavior in Polymeric Semiconductors. *Annu. Rev. Phys. Chem.* **2014**, *65*, 477-500.

25. Schwartz, B. J. Conjugated Polymers as Molecular Materials: How Chain Conformation and Film Morphology Influence Energy Transfer and Interchain Interactions. *Annu. Rev. Phys. Chem.* **2003**, *54*, 141-172.

26. Spano, F. C.; Clark, J.; Silva, C.; Friend, R. H. Determining Exciton Coherence from the Photoluminescence Spectral Line Shape in Poly(3-Hexylthiophene) Thin Films. *J. Chem. Phys.* **2009**, *130*, 074904.

27. Yamagata, H.; Spano, F. C. Vibronic Coupling in Quantum Wires: Applications to Polydiacetylene. *J. Chem. Phys.* **2011**, *135*, 054906.

28. Chu, B.; Wang, Z.; Yu, J. Dynamic Light Scattering Study of Internal Motions of Polymer Coils in Dilute Solution. *Macromolecules* **1991**, *24*, 6832-6838.

29. Tsunashima, Y.; Nemoto, N.; Kurata, M. Dynamic Light Scattering Studies of Polymer Solutions. 2. Translational Diffusion and Intramolecular Motions of Polystyrene in Dilute Solutions at the Θ Temperature. *Macromolecules* **1983**, *16*, 1184-1188.

30. Sedlák, M. The Ionic Strength Dependence of the Structure and Dynamics of Polyelectrolyte Solutions as Seen by Light Scattering: The Slow Mode Dilemma. *J. Chem. Phys.* **1996**, *105*, 10123.

31. Combet, J.; Lorchat, P.; Rawiso, M. Salt-Free Aqueous Solutions of Polyelectrolytes: Small Angle X-Ray and Neutron Scattering Characterization. Eur. Phys. J. : Spec. Top. **2012**, *213*, 243-265.

32. Glatter, O.; Kratky, O. *Small Angle X-Ray Scattering*; Academic Press, 1982.

33. Berne, B. J.; Pecora, R. *Dynamic Light Scattering: With Applications to Chemistry, Biology, and Physics*; Dover Publications, 2013.

34. Scotti, A.; Liu, W.; Hyatt, J. S.; Herman, E. S.; Choi, H. S.; Kim, J. W.; Lyon, L. A.; Gasser, U.; Fernandez-Nieves, A. The Contin Algorithm and Its Application to Determine the Size Distribution of Microgel Suspensions. *J. Chem. Phys.* **2015**, *142*, 234905.

35. Barford, W.; Marcus, M. Theory of Optical Transitions in Conjugated Polymers. I. Ideal Systems. *J. Chem. Phys.* **2014**, *141*, 164101.

36. Marcus, M.; Tozer, O. R.; Barford, W. Theory of Optical Transitions in Conjugated Polymers. II. Real Systems. *J. Chem. Phys.* **2014**, *141*, 164102.

37. Collini, E.; Scholes, G. D. Coherent Intrachain Energy Migration in a Conjugated Polymer at Room Temperature. *Science* **2009**, *323*, 369-373.

Chapter 3

Disassembly of an Inter-Conjugated Polyelectrolyte Complex using Ionic Surfactants

Abstract

The ability to manipulate the state of assembly of light-harvesting molecular materials can be important to control light-induced damage at high illumination intensities. Disassembly of such materials is thus an important consideration from a photoprotection perspective. Here, we show that an artificial light-harvesting antenna based on an inter-conjugated polyelectrolyte complex can be disassembled using ionic surfactants in aqueous solution. We demonstrate that both anionic and cationic surfactants can do so with comparable efficiency, thereby shutting electronic energy transfer between the exciton donor and acceptor conjugated polyelectrolytes. However, the structural evolution of the aqueous complexes both above and below the critical micelle concentration differed significantly depending on the sign of the ionic surfactant and the relative polyion charge ratio.

3.1 Introduction

Conjugated polyelectrolytes (CPEs) – conjugated polymers appended with ionic sidechains – are fascinating materials because of their strong coupling between ionic and electronic degrees of freedom. This results in photophysics and dynamics that depend sensitively on the chain microstructure in polar solvents. The charged sidechains of CPEs can be utilized in aqueous ionic self-assembly to spontaneously form nanoscale complexes, whose structure and electronic properties can be tuned with excess ions or by the presence of other small and macro molecules. These effects can in turn be leveraged in sensing, biomedical and materials applications. [1–13] Specifically, much work has been done on the complexation of CPEs with ionic surfactants in water, resulting in substantial changes in the CPE spectroscopy and conformation depending on the surfactant chain length and polar group head. [9–27] Further, qualitatively different photophysical regimes of the CPE-surfactant complex were uncovered below and above the critical micelle concentration (cmc).

We have previously shown that under certain conditions oppositely charged CPEs may be complexed together in aqueous solution, and if the electronic properties of the two CPEs are properly chosen, complexation can lead to rapid electronic energy transfer upon photoexcitation even at dilute concentrations.[28,38] Additionally, we showed that the process of inter-CPE complexation in aqueous solution could lead to formation of emergent excitonic states associated with substantial chain straightening and break-up of intramolecular π-stacks. The result is that the acceptor CPE photoluminescence quantum yield increases by a factor of ~ 20. This phenomenon is

rooted in the CPE backbone connectivity of the ionic sidechains and has no analogue with ionic dye molecules.

Inter-CPE complexation is a correlated process that involves ion pairing of many oppositely charged partners on the two CPEs. At relative ionic stoichiometry, the complex is unstable with respect to phase separation in low-salt solutions. The phase-separated solid state that forms is highly resistant to disassembly with respect to strongly acidic and surfactant-rich solutions alike. However, at non-stoichiometric polyion compositions, the aqueous complex is stable over a broad range of compositions. Can the two CPEs in the nonstoichiometric complex be uncoupled in solutions with low excess salt? Since an ionically assembled CPEC can function as an artificial electronic energy transfer (EET) antenna, understanding possible CPEC disassembly can lead to better control of photoprotection in ionic materials. In this work our goal is to address the following specific question: Can ionic surfactants be used as uncoupling agents for nonstoichiometric CPECs, and, if so, is there a dependence on relative polyion composition? That is, we seek to determine whether CPE-ionic surfactant interactions out-compete inter-CPE complexation, or whether ionic surfactants act synergistically to manipulate EET between the excited-state donor and acceptor CPEs without shutting it off.

To answer these questions, we have used a pair of energy transfer donor/acceptor CPEs based on a cationic energy donor, poly(fluorene-alt-phenylene), and an anionic energy acceptor, poly(thiophene). The general behavior of CPEs interacting with oppositely charged surfactants as a function of aliphatic surfactant length is relatively well-understood. Thus, here we focus on a thoroughly investigated,

representative dodecyl surfactants. We examined the photophysics of the complexes at varying CPE and surfactant stoichiometries to systematically interrogate the ternary macromolecular system. We used two model surfactants with oppositely charged headgroups and identical aliphatic tails, as there is prior work showing that there is reason to suspect that the sign of the headgroup charge may be important to complexation.[42] We find evidence that at symmetric polyion compositions, both the anionic and cationic surfactants were effective at disassembling the CPEC in salt-free aqueous solution, thereby largely shutting off EET. This took place both below and above the critical surfactant micelle concentration. However, the evolution of the CPE photophysics in the ternary solution showed intriguing differences between cationic and anionic surfactants. We believe this difference can be largely traced to the dominant conformation assumed by the polyelectrolytes when surrounded by its oppositely charged surfactant partner.

3.2 Experimental Methods

Sample Preparation

The doubly cationic CPE PFPI (MW = 21,000 Da; polydispersity = 1.2) was obtained from Solaris Chem Inc. The singly anionic CPE PTAK (MW = 16,000 Da; polydispersity = 2.2) was obtained from Rieke Metals. Sodium dodecyl sulfate (SDS, ≥ 99%) and dodecyltrimethylammonium chloride (DTAC, ≥ 99%) were obtained from Sigma Aldrich. All materials were used as received.

The CPEC solutions were prepared at different molar charge ratios with respect to the charge per CPE monomer unit. The PFPI concentration was fixed at 0.1 mg/mL for nearly all CPEC solutions. The sole exception was for the 0.25:1 CPEC samples

(with and without DTAC) used for spectroscopic measurements, which was done to eliminate self-absorption issues that were found to be significant for this sample set.

The CPEC solutions were prepared as follows. For CPEC solutions with anionic surfactant (SDS), solutions at the desired SDS concentration were diluted from an SDS stock (100 mg/mL) with HPLC water as the solvent. PFPI was first added drop-wise from a prepared stock solution to the diluted SDS solutions, after which PTAK was added drop-wise from its corresponding stock solution while stirring at room temperature to achieve the desired charge ratio. Similarly, diluted DTAC solutions were first prepared at a desired concentration and were diluted from a DTAC stock (50 mg/mL) with HPLC water as the solvent as well. PTAK was first added drop-wise from a prepared stock solution to the diluted DTAC solution, after which PFPI was added drop-wise from its corresponding stock solution while stirring at room temperature to achieve the desired charge ratio. The CPEC-Surfactant solutions were then stirred at ~70 °C for 24 hours. We have shown previously that at this elevated temperature, solutions containing PFPI and PTAK in the absence of surfactant or excess salt readily form CPECs. Solutions that showed solid/liquid phase separation were centrifuged at 1500 rpm for 15 min, after which the liquid phases were separated for further measurements.

Steady-State Spectroscopy

Optical density measurements were taken with a Shimadzu UV-2700 Spectrophotometer with an integration time of 0.1s and a 2.0 nm slit width over the desired range. Photoluminescence measurements were taken using a Horiba

Fluoromax-4 spectrofluorometer in a right-angle geometry in cuvettes with 1 mm pathlengths. The measured integration time was 0.1s. Both the emission and excitation slit widths were 2 nm.

Dynamic Light Scattering (DLS)

DLS measurements were conducted as detailed in a previous publication.[28] To extract the distribution of relaxation times, the CONTIN algorithm was used.[31] Relaxation time distributions were determined for scattering angles of 20° and 90° with the CONTIN regularization parameter α set to 0.2. α values and grid densities were varied in order to have confidence in the relaxation times.

Small-Angle X-ray Scattering (SAXS)

SAXS measurements were performed at beamline 4−2 at the Stanford Synchrotron Radiation Laboratory (SSRL) using a Rayonix MX225-HE detector. The incident photon energy was 11 keV X-ray (1.17 Å), and the sample-detector distance was 2.5 m. Multiple 1s exposures were taken and averaged prior to analysis. To avoid degradation, samples were oscillated during data collection. SasTool (SSRL) was used to convert collected 2D TIFF images to intensity vs scattering vector length and to subtract solvent scattering (HPLC water). Pair distance distribution functions were calculated using the indirect Fourier Transform (Glatter). To investigate the influence of possible inter-particle scattering contributions in samples with relatively large surfactant concentrations, the generalized version of the indirect Fourier transform (GIFT) was used. Specifically, we employed the charged spheres model with a Yukawa

interaction potential along with the HNC closure relation.[43]

3.3 Results

The chemical structures of the polycation PFPI, polyanion PTAK and ionic surfactants used in this work are shown in **Figure 3.1**. We focus on a fixed surfactant alkyl length (dodecyl) and vary the polar head from an anionic sulfate to a cationic quaternary ammonium group. We have chosen the alkyl length based on the previously available characterization to aid our interpretation herein. Previous work by Burrows *et al*. showed that when a CPE highly analogous to PFPI is added to an aqueous solution containing the oppositely charged dodecyl sulfate (SDS), the photoluminescence (PL) spectrum of the cationic CPE is seen to undergo substantial changes. [22] Specifically, both the PL quantum yield and the PL spectrum shape change in a manner that depends on the concentration of SDS, ultimately leading to significantly brighter, more

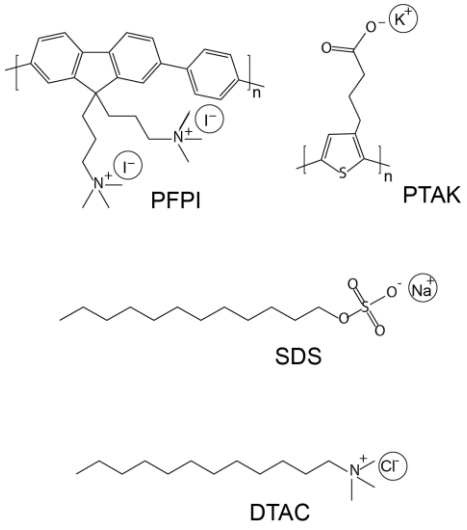

Figure 3.1 Chemical structures of conjugated polyelectrolytes and ionic surfactants used herein.

structured emission above the cmc relative to the isolated CPE. We have reproduced these findings herein, which are shown in the Supporting Information.

CPE Complexes with Anionic Surfactants

Figure 3.2 shows optical density (OD) and PL spectra of CPECs as a function of SDS concentration. The PFPI:PTAK ionic charge ratio has been fixed at 1:0.25 (or 80/20 charge percentage ratio), which corresponds to a charge-nonstoichiometric

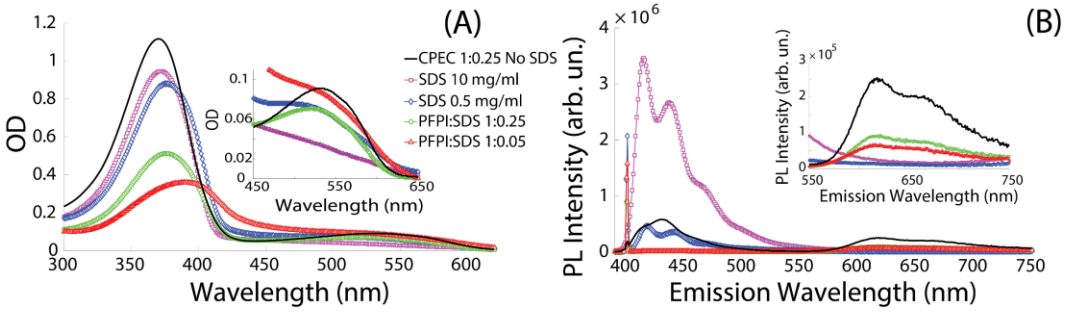

Figure 3.2 (A) OD and (B) PL spectra of CPEC-SDS complexes in aqueous solution with varying SDS concentrations. Increased surfactant concentration leads to an increased red shift of the PFPI λ_{max}. CPEC-SDS complexes below the molar charge equivalence of PFPI:SDS lead to increased precipitation of charge-neutralized, hydrophobic CPEC-SDS complexes. Above PFPI:SDS molar charge equivalence, the PFPI PL shows a well resolved vibronic structure. The inset in (A) shows a zoomed-in region of the PTAK OD, whereas the inset in (B) magnifies the PTAK PL region.

composition with excess cationic PFPI sites. The sharp absorption centered about 365 nm and characterized by a relatively large molar extinction coefficient is due to PFPI, whereas the broader, less intense absorption peaked around 550 nm is due to PTAK.

Figure 3.2A shows that with addition of relatively small amounts of SDS (1:0.05 and 1:0.25 PFPI charge to SDS charge ratio), the PFPI OD drops substantially relative to the CPEC in the absence of SDS. We interpret this as association of PFPI and SDS with some subsequent PFPI:SDS complex precipitation. The situation

changes qualitatively when the SDS concentration begins approaching its cmc (~ 2.39 mg/mL in isolation) [41]: The PFPI OD is now again comparable to the control CPEC solution, and the peak shift is consistent both with previous work and our results based on PFPI:SDS solutions (see Supporting Information). Interestingly, around the SDS cmc, the inset shows that the low-energy PTAK absorption changes in a subtle yet distinct manner compared to the control CPEC sample.

Figure 3.2B shows PL spectra excited at 400 nm for the same samples. The CPEC solution without SDS shows a relatively small amount of PFPI emission centered about 425 nm, which is quenched by ~50% relative to isolated PFPI at the same concentration. The peak is fairly featureless, with a nominal 0-0/0-1 vibronic peak ratio < 1. The area between 600 and 700 nm is due to PTAK emission. As we showed previously, PTAK emission in the CPEC corresponds to a drastic increase in the PL quantum yield compared to isolated PTAK solutions. [28] The native PTAK conformation in isolation is that of a relatively collapsed coil with a significant density of intrachain π-stacked regions – a situation that corresponds to low PL intensities of H-aggregate-like excited states. This change in the PTAK quantum yield is due to both the uncoiling of PTAK chains upon binding to PFPI, as well as direct resonant energy transfer from PFPI to PTAK.

When the SDS concentration reaches 0.5 mg/mL, the PFPI PL becomes much more structured, and the PTAK PL intensity drops precipitously. Further increasing the SDS concentration to 10 mg/mL, which is well in excess of its nominal cmc, the highly structured PFPI PL grows by a factor of ~7.5, while PTAK PL remains largely quenched. To understand these spectral changes, we refer to the molecular exciton

model developed by Kasha for aggregated dye molecules and extended to conjugated polymers by Spano.[30] The basic premise of the model is that the ratio of vibronic PL peaks can be used to (at least qualitatively) evaluate the relative strength of intramolecular and intermolecular interactions. For conjugated polymers, when the inter-monomer *intrachain* coupling dominates, the vibronic 0-0/0-1 peak ratio > 1. When chromophores either on the same chain or between more than one chain π-stack, the interchain coupling becomes significant; if it dominates, one expects 0-0/0-1 peak ratio < 1. The former situation (J-like excited-states) is associated with relatively large PL quantum yields, while the latter (H-like excited states) leads to relatively low quantum yields.

Figure 3.2B shows that above the SDS cmc, the nominal PFPI 0-0/0-1 intensity ratio is clearly > 1, indicating emissive states characterized by an extended chain conformation with a highly delocalized excitonic wavefunction. Closer inspection of the inset in **Figure 3.2A** shows that the rise in structured PFPI PL appears correlated with development of some subtle low-energy structure in the PTAK OD. This not a mere coincidence: The low-energy PTAK OD structure is consistent with an increase in the concentration of π-stacked regions, which is characteristic of the isolated PTAK state in water. We would expect that in such a circumstance, the PTAK PL should be very low given the H-like excited-state nature – precisely what we observe. Thus, the steady-state photophysics strongly imply that above the cmc, the PFPI:SDS interaction outcompetes that due to PFPI:PTAK, leading to (at least partial) CPEC dissociation and regeneration of poorly emissive PTAK states. We stress that this was observed independent of the order of surfactant addition. That is, we observed minimal PFPI-to-

PTAK energy transfer upon introduction of SDS (both above and below the cmc), regardless of whether the ternary solution was heated at elevated temperatures or whether SDS was added *after* a CPEC was formed and cooled to room temperature.

To characterize the changes in complex solution morphology that accompany these spectroscopic changes, we first turn to dynamic light scattering (DLS). To create a basis for comparison, we first examine the SDS concentration behavior of PFPI:SDS complexes alone before describing the ternary macromolecular system.

The scattered intensity autocorrelation functions (ACFs) of the PFPI-SDS complexes (Figure 3A) differ significantly below and above the cmc of SDS. **Figure**

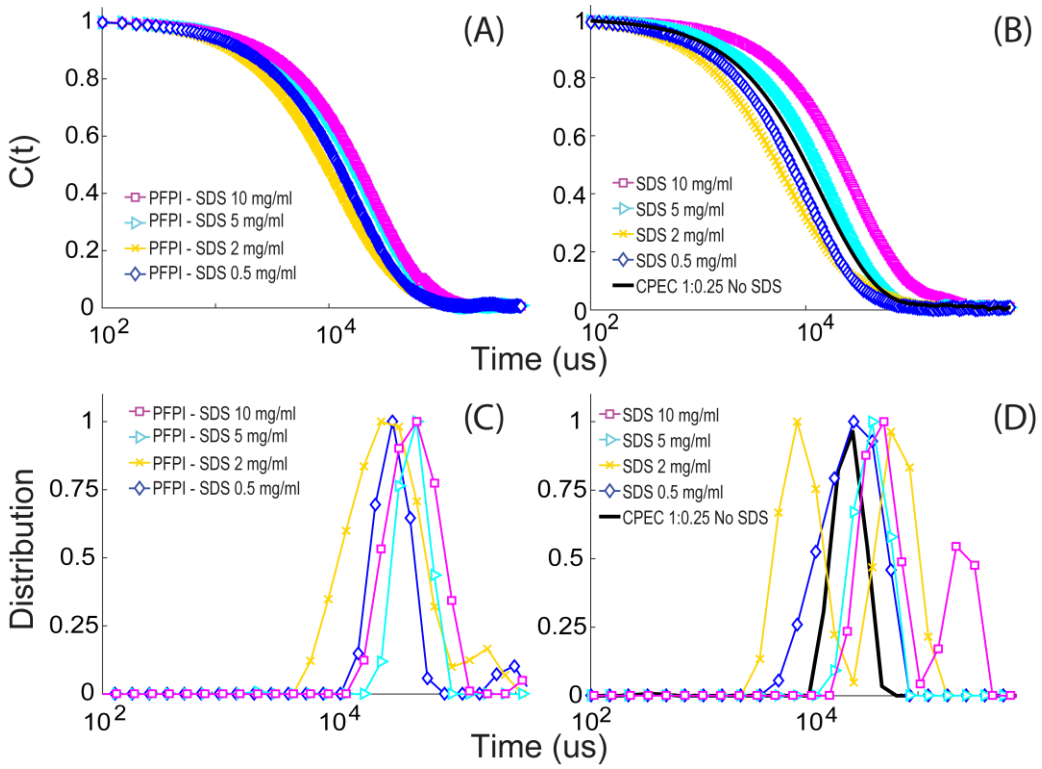

Figure 3.3 Normalized scattered intensity autocorrelation functions of (A) PFPI-SDS complexes and (B) CPEC-SDS complexes. Relaxation time distributions for (C) PFPI-SDS complexes and (D) CPEC-SDS ternary complexes were obtained by the CONTIN program. Isolated PFPI is not shown due to its poor scattering.

3.3C shows relaxation time distributions obtained by applying the CONTIN algorithm to scattered-field ACFs following application of the Siegert relation. [31,32] To gain confidence in the physical significance of the solutions, we systematically varied the regularization parameter to ensure that results were robust.

Addition of SDS at all concentration leads to a monomodal distribution of PFPI-SDS complexes. The mean relaxation time clearly shrinks from 3.4 x 10^4 μs to 2.8 x 10^4 μs in going from 0.5 to 2 mg/mL SDS, which is just below the nominal cmc for SDS in isolation. [29] Using the Stokes-Einstein equation [33], this corresponds to a decrease in mean complex size from 90 nm to 74 nm. However, above the cmc, the mean relaxation time begins to increase, reaching 5.6 x 10^4 μs (148 nm) at 10 mg/mL SDS. SDS concentrations just below the cmc (~2.39 mg/mL) and with excess micelles in solution (10 mg/mL) lead the broadest distribution of relaxation times. The fit results are summarized in **Table A2.1.**

When varying concentrations of SDS are added to CPEC solutions, the DLS trend is qualitatively similar (**Figure 3.3B** and **Figure 3.3D**). However, there are important distinctions that are worth highlighting. First, right around the cmc, the relaxation time distribution clearly becomes bimodal. At 5 mg/mL SDS, the (broad) distribution again becomes monomodal, with a mean size that substantially exceeds that of 2 mg/mL solution (102 nm). This change in mean size corresponds well to the behavior of PFPI:SDS complexes alone. Interestingly, at 10 mg/mL SDS, the distribution again shows bimodality; the mean sizes corresponding to the first and second peak are 129 and 717 nm, respectively. The lower size again agrees with the peak of the corresponding PFPI:SDS complex. Evidently, the slow diffusive mode

characterized by the larger relaxation time is thus native to the ternary PFPI:PTAK:SDS complex.

To further characterize the nanoscale solution morphology of the complexes and, importantly, to verify that we have in fact formed micelles, we have performed small-angle X-ray scattering measurements. Scattering intensities as a function of scattering vector length, Q, are shown in **Figure 3.4A** for PFPI:SDS and PFPI:PTAK:SDS solutions. At these relatively low concentrations used in optical measurements, the scattering intensity (relative to the solvent background) at low SDS concentrations is relatively modest. Nevertheless, the signal-to-noise ratio of samples

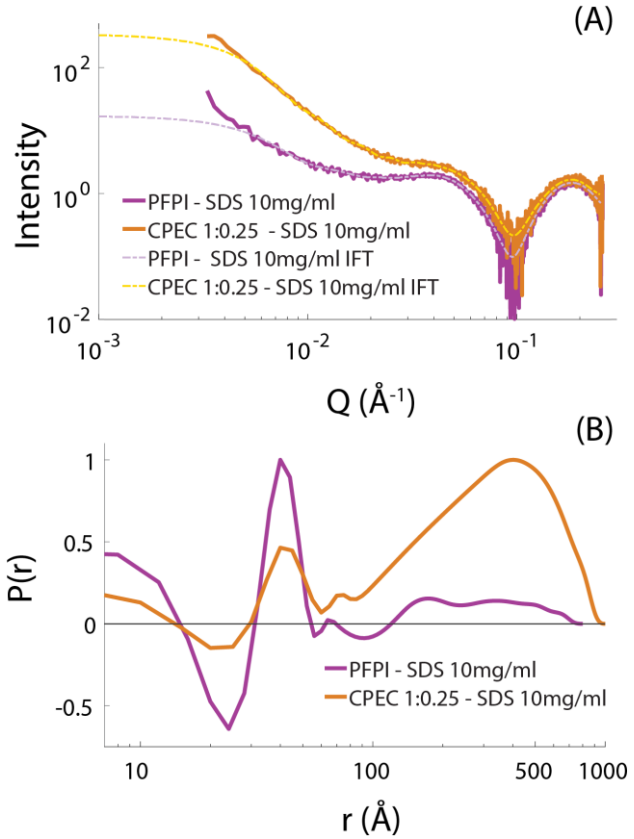

Figure 3.4 (A) SAXS profiles of aqueous solutions of PFPI-SDS complexes and CPEC-SDS complexes above the cmc of SDS. (B) Corresponding pair distance distribution functions P(r) obtained by an indirect Fourier transform.

above the nominal cmc allows for quantitative modeling, which we have performed using the indirect Fourier transform (IFT) technique. [34] Application of the IFT yields a pair-distance distribution function (PDDF) that characterizes the spatial correlation of the particle's scattering contrast. IFT interpolates the intensity in the low-Q region, which is experimentally unavailable. The resulting PDDFs are shown with logarithmic r scaling in **Figure 3.4B** for PFPI:SDS and PFPI:PTAK:SDS solutions, respectively, to highlight structural features at both short and long distances.

Because the solutions were relatively dilute, it may be reasonable to consider ignoring inter-particle scattering contributions, such that the scattering data could be converted to real-space using the IFT. To test the validity of this assumption, the generalized IFT (GIFT) was applied to concentrated surfactant solutions (10 mg/mL).[34] This was done to ensure that excess micelles in solution weren't contributing to inter-particle scattering as has been done before in similar micellar systems.[36] Very similar PDDFs were obtained, building confidence with our IFT results. Nevertheless, care must be taken when interpreting the large-r regions of the PDDF.

At 10 mg/mL SDS, the scattering intensity shows a clear oscillation, which gives rise to the oscillatory feature in the PDDF at low values of the intraparticle coordinate r. This is precisely what is expected from a micelle-containing solution and is consistent with prior literature. [36] The zero crossing in the PDDF corresponds to a change in mean contrast within the particle, as expected for a particle containing a polar headgroup corona and an aliphatic interior. Thus, this data confirms the presence of micelles at this SDS concentrations with a size of ~6nm. There is, however, no clear sign of a Guinier plateau; thus, we refrain from assigning physical significance to the

PDDF behavior at large r. Nevertheless, we can definitively say that at these CPE concentrations, the presence of both PFPI and PTAK does not disrupt SDS micelle formation.

CPE Complexes with Cationic Surfactants

Keeping the aliphatic tail length constant but varying the nature of the surfactant head group, we investigated the interaction of the individual cationic (PFPI) and anionic (PTAK) CPEs with cationic surfactant dodecyltrimethylammonium chloride (DTAC) both above and below its cmc (~5.8 mg/mL). [41] The steady-state spectroscopy of PFPI:DTAC and PTAK:DTAC solutions is displayed in the Supporting Information.

We first examined the interaction of DTAC with the oppositely charged PTAK below (0.5 mg/mL) and above (10 mg/mL) DTAC's cmc. Addition of DTAC at both concentrations leads to a drastic blue shift of the PTAK OD: λ_{max} decreases from 505 to 405 nm. This indicates a large decrease in the effective conjugation length along the PTAK backbone. Concomitantly, we observe a break-up of most inter-chromophore interactions, which gave rise to the red shoulder near the OD onset in isolated PTAK solution. Addition of DTAC at both concentrations also leads to a significant increase in the PTAK emission intensity, as shown in the Supporting Information.

We examined the influence of DTAC on the formation of the PFPI:PTAK complex by concentrating on two relative PFPI:PTAK charge ratios of 1:0.25 and 0.25:1. In the latter case, as with SDS above, the CPE that will predominantly interact with the surfactant molecule is in molar excess relative to the oppositely charged CPE. We first describe the photophysics of the ternary PFPI:PTAK:DTAC system at the 1:0.25 PFPI:PTAK charge ratio. **Figure 3.5A** and **Figure 3.5B** show the OD and PL spectra of the 1:0.25 PFPI:PTAK CPEC with DTAC, respectively. The inset in **Figure 3.5A** focuses on a zoomed-in region centered about the PTAK absorption spectrum, which shows that at 0.5 mg/mL DTAC, the drastic ~100 nm blue-shift is not observed, in contrast to PTAK:DTAC solutions. Instead, the PTAK OD is diminished. Upon

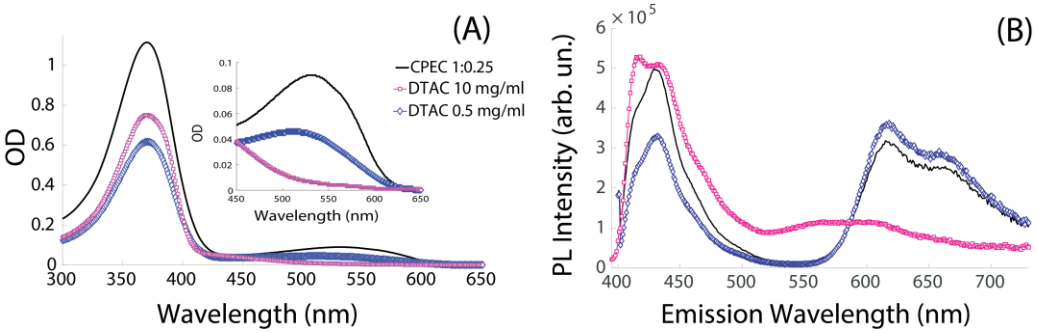

Figure 3.5 (A) OD and (B) PL spectra of CPEC-DTAC complexes with excess PFPI (1(+):0.25(-) molar charge ratio) in aqueous solution concentrations of DTAC above its cmc and below its cmc. Inset in figure 5A shows the zoomed in OD region of PTAK. CPEC with excess PFPI leads to distinct 0−0/0−1 vibronic ratios in the PFPI emission dependent on the concentration of DTAC. The excitation wavelength is 400 nm.

increasing the DTAC concentration to 10 mg/mL, a large blue shift is indeed observed.

Figure 3.5B shows PL spectra of the CPEC-DTAC samples upon 400 nm excitation. Compared to the CPEC control with no added surfactant, the PTAK PL increases slightly, while the PFPI intensity further decreases by 40% beyond the native quenching of PFPI PL in the presence of PTAK. It is important to note that at this

DTAC concentration, the OD for both PFPI and PTAK decrease relative to the control CPEC. This means that the increase in PTAK PL per unit OD – a proxy for the PL quantum yield – is somewhat larger than the PL intensity suggests. Evidently, below the DTAC cmc, the PTAK:DTAC interaction is insufficient to decouple PTAK from PFPI. In contrast, increasing the DTAC concentration to 10 mg/mL instead leads to an increase in the PFPI PL relative to both the 0.5 mg/mL DTAC and the pure CPEC solution. At the same time, the PFPI vibronic 0-0/0-1 intensity ratio similarly increases as the PTAK PL blue-shifts, the latter being analogous to the OD. The increase in the PFPI PL intensity and the concomitant drop in the PTAK PL likely corresponds to a partial decoupling or "loosening" of the PFPI:PTAK complex, thereby lowering the apparent energy transfer rate.

To get a more detailed understanding of the influence of DTAC on energy transfer from PFPI to PTAK, we collected the PL excitation spectra (**Figure 3.A3**) at a fixed emission wavelength corresponding *exclusively* to PTAK PL. The excitation spectrum thus tells us which excited states give rise to PTAK PL. **Figure 3.A3**shows that the control CPEC and the CPEC with 0.5 mg/mL DTAC resemble a linear combination of PTAK and PFPI absorption spectra. This indicates that upon excitation of PFPI, energy is transferred from PFPI to PTAK, leading to enhancement in PTAK PL over the wavelengths where PFPI absorbs. Evidently, the influence of 0.5 mg/mL DTAC on the net enhancement of PTAK PL in the CPEC is fairly mild, with some reshuffling in PL intensity between 300 and 400 nm. The small PL enhancement upon addition of 0.5 mg/mL DTAC at 400 nm shown in **Figure 3.5B** is thus not maintained at all excitation wavelengths. Upon raising the DTAC concentration to 10 mg/mL, the

PL intensity drops as the long-wavelength onset of the excitation spectrum blue-shifts, again consistent with the OD. What is also apparent is that as the DTAC concentration is raised above its cmc, the contribution to the PTAK PL excitation spectrum at short wavelengths that correspond to maximal PFPI absorption becomes significantly diminished.

There are some indications that the manner in which DTAC alters the CPEC may differ from that of SDS when the PFPI:PTAK charge ratio in the CPEC is 1:0.25, corresponding to a molar excess of PFPI. However, in this case we expect that the majority of PTAK charges are initially tied up via interactions with PFPI. We thus next examine the charge-symmetric case, that is, when PTAK is in molar excess, to determine whether in such a circumstance both surfactants ultimately lead to a similar

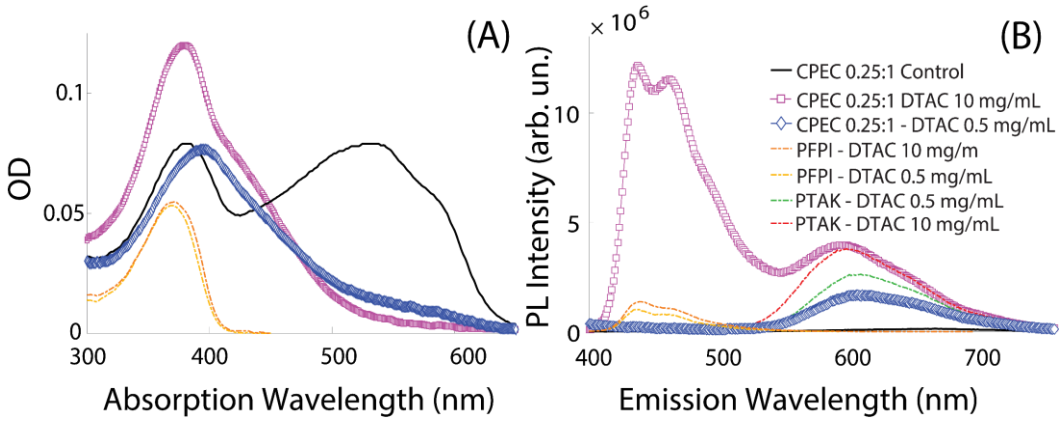

Figure 3.6. (A) OD and (B) PL spectra of CPEC-DTAC complexes with excess PTAK (0.25(+):1(-) molar charge ratio) in aqueous solution concentrations of DTAC above its cmc and below its cmc .and PFPI-DTAC solutions at the same DTAC concentrations. Panel (B) shows the PL spectra of PTAK-DTAC solutions at the same DTAC concentrations. Complexation of PTAK to DTAC leads to a turning on and blue-shift of the PL spectra at both concentrations of DTAC with and without the presence of PFPI. The PFPI PL shows more dependence on the concentration of DTAC and presence of PTAK.

break-up of the CPEC. In this case, there is significant excess PTAK charge density available to interact with DTAC.

Figure 3.6 shows the evolution of the CPEC photophysics upon addition of DTAC at the 0.25:1 PFPI:PTAK charge ratio. We note that because of self-absorption effects, the total molar CPE concentration used in spectroscopic measurements was an order of magnitude lower in the 0.25:1 CPEC. The spectra show intriguing differences, both compared to SDS results and DTAC results at the 1:0.25 PFPI:PTAK charge ratio. The OD for the 0.25:1 CPEC (**Figure 3.6A**) shows that the low-energy structure in the PTAK spectrum in the 1:0.25 complex resembles isolated PTAK more than it does PTAK in the 1:0.25 CPEC, consistent with our recent findings.[38] Upon introduction of DTAC at 0.5 mg/mL, the OD of PTAK undergoes a substantial blue-shift. Evidently, the effect of increasing DTAC concentration is to progressively shift oscillator strength from the red to the blue, similar to the symmetric 1:0.25 ratio CPEC above the DTAC cmc (see also **Figure 3.A2**). Figure 6B shows PL spectra for the 0.25:1 CPEC as a function of DTAC concentration, along with several relevant control samples. Due to significant changes in the OD spectrum at various DTAC concentrations, we have plotted the PL normalized by corresponding OD at the excitation wavelength (370 nm).

First, we see that for the 0.25:1 with no DTAC as well as in the presence of DTAC at 0.5 mg/mL, there is discernable PL signal due to PFPI. We previously showed that in the bare CPEC at the 0.25:1 composition, all PFPI excitons rapidly transfer to PTAK. The near-complete PL quenching of PFPI PL in the 0.25:1 CPEC at the 0.5 mg/mL DTAC concentration may suggest that EET between PFPI and PTAK continues

to be highly effectively, as the PTAK OD becomes strongly blue-shifted due to its interaction with DTAC. The blue-shift of the PTAK PL leads to an increase in the spectral overlap integral between PFPI PL and PTAK OD. Within the Förster model, the EET rate scales as the spectral overlap, SO. [39,40] This quantity scales as follows:

$$SO \propto \int_{E_1}^{E_2} \widetilde{PL}_{PFPI}(E) \times \widetilde{OD}_{PTAK}(E) \frac{dE}{E^4} \qquad \textbf{(eqn.1)}$$

where $\widetilde{PL}_{PFPI}$ is the PL intensity of the exciton donor normalized by its spectral area, and $\widetilde{OD}_{PTAK}$ is the OD of the exciton acceptor normalized by its spectral area. We find that the integral in **Equation 3.1** increases slightly from 1.94 in the absence of surfactant to 2.26 in the presence of 10 mg/mL DTAC.

At 10 mg/mL DTAC, PL signal due to PFPI rises by more than an order of magnitude compared to the 0.5 mg/mL sample. Such a sharp rise would be consistent with a significant lowering in the inter-CPE EET efficiency. We see that PL due to the PTAK control at 10 mg/mL DTAC perfectly traces out the corresponding CPEC spectrum on the red side. To determine whether the total CPEC spectrum reflects a fractional lowering of the EET rate or a complete uncoupling of the CPEC and thus the vanishing of the rate, we must determine the extent of PFPI PL quenching when compared to the corresponding PFPI control at the same DTAC concentration. Figure 6B shows that the PL intensity of the corresponding PFPI/DTAC control solution is in fact *lower* than the 0.25:1 CPEC at 10 mg/mL DTAC! This observation is somewhat surprising, and it has several implications. First and foremost, since PFPI in the absence of DTAC is highly emissive, the PL quantum yield of PFPI must be significantly lowered in the presence of the similarly charged DTAC, both below and above the DTAC cmc. A lowering of the conjugated polymer PL quantum yield is often

associated with chain coiling and a concomitant increase in the number density of inter-chromophore π-stacks. The latter act as poorly emissive exciton sinks. Because of this, we believe that the electrostatic repulsion and physical crowding due to the presence of a relatively large concentration of cationic surfactants lead to the collapse of the PFPI chain. Thus, this eliminates the PFPI:DTAC sample as a proper "unquenched" control for EET of the corresponding 0.25:1 CPEC.

Second, the observation that PFPI PL was largely quenched in the 0.25:1 CPEC in the presence of 0.5 mg/mL DTAC discussed above must be revisited in light of the results from PFPI:DTAC controls. This is because it may no longer be appropriate to suppose that a small PFPI PL intensity implies a significant inter-CPE EET rate at the 0.25:1 ratio in the presence of DTAC. To shed light on this complication, we again turned to PL excitation spectra, which can provide significant additional insight to this matter. **Figure 3.7A** shows the normalized OD of the 0.25:1 CPEC at 0.5 mg/mL DTAC, along with normalized PL excitation spectra for the same CPEC and the PTAK:DTAC control. The emission wavelength has again been fixed at 650 nm, which corresponds to PTAK only. Interestingly, while the OD spectrum of the CPEC resembles a linear combination of absorption due to PFPI, blue-shifted PTAK and a small fraction of distinct PTAK transitions at the red edge, this is not the case for the excitation spectra. It is clear that the CPEC excitation spectrum is missing the region with the distinct red-absorbing states, indicating that PTAK excitons that absorb

between 550 nm and 650 nm have vanishing PL quantum yields, consistent with spectroscopically dark, π-stacked inter-chromophore species

Further, on the blue side, the normalized PL excitation intensity is lower than the normalized OD. Further, the CPEC excitation spectrum displays excellent overlap with the corresponding PTAK:DTAC control. This strongly suggests that even below the DTAC cmc, inter-CPE EET is at least partially disrupted compared to the CPEC in the absence of DTAC. We find a similar situation at 10 mg/mL DTAC, which is shown

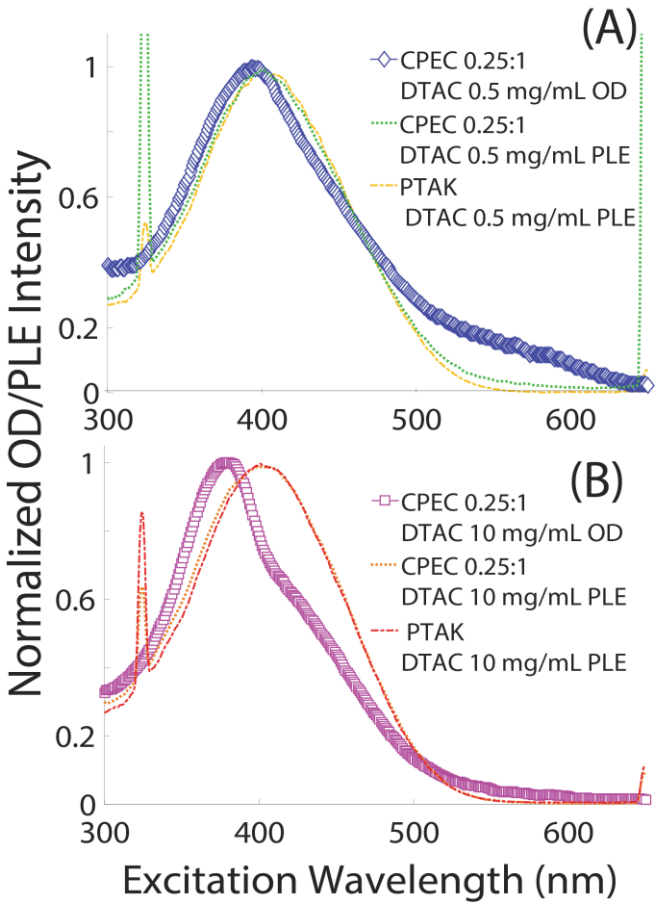

Figure 3.7 Normalized OD and PL excitation (PLE) spectra of the 0.25:1 CPEC in the presence of DTAC at (A) 0.5 mg/mL and (B) 10 mg/mL. PL excitation (PLE) spectra was collected at emission wavelength of 650 nm, exclusive to PTAK PL.

in **Figure 3.7B**. The significant departure on the blue side of the PTAK PL excitation spectrum in the CPEC from that of the corresponding (normalized) OD is again suggestive of CPEC uncoupling, leading to a lowering in the inter-CPEC EET efficiency. To characterize changes in structure that accompany these spectroscopic changes, we again performed DLS and SAXS measurements on PTAK/DTAC and ternary PFPI/PTAK/DTAC solutions.

Figure 3.8A shows SAXS intensity curves for PTAK:DTAC and CPEC:DTAC solutions at 10 mg/mL DTAC. SAXS results confirm that at 10 mg/mL, micelles of

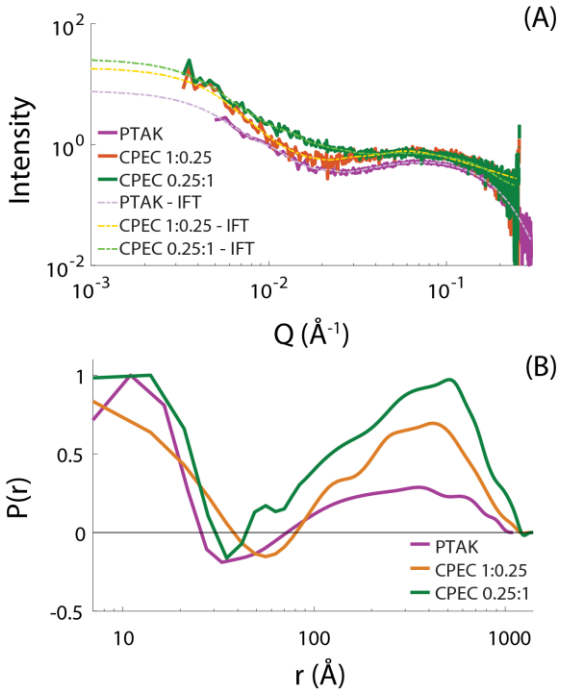

Figure 3.8 (A) SAXS profiles of aqueous solutions of PTAK-DTAC complexes and CPEC-DTAC complexes above the cmc of DTAC. (B) Corresponding PDDFs obtained by an indirect Fourier transform.

DTAC are present. The functional form of the PDDF (Figure 8B) shows a characteristic zero-crossing due to a change in the scattering contrast sign, indicative of the micelle's

core-shell structure in solution. We estimate the diameter of the micelles to be ~5 nm.[41] Scattering intensities at 0.5 mg/mL DTAC over this scattering vector range were significantly smaller and did not display the oscillation indicative of micelles. This is shown in the Supporting Information.

Figure 3.9A, **Figure 3.9B** and **Figure 3.9C** displays ACFs for PTAK:DTAC, 1:0.25 CPEC:DTAC and 0.25:1 CPEC:DTAC solutions, respectively. The respective plots of the relaxation time distributions are shown **Figure 3.9D**, **Figure 3.9E** and **Figure 3.9F**. **Figure 3.9D** shows that in PTAK:DTAC control solutions, increasing the DTAC concentration from 0.5 to 10 mg/mL leads to a mean size contraction but also a broadening, with the peak of the distribution decreasing from 30 nm to 22 nm. We note that pure PTAK solutions at this concentration do not give rise to sufficiently large light-scattering intensities to allow us to collect a high-quality ACF. A similar size contraction effect is seen upon introduction of DTAC to the 1:0.25 CPEC solution. For the 0.25:1 CPEC in **Figure 3.9F**, DTAC at 0.5 mg/mL leads to a relatively small size contraction relative to the control CPEC sample. At 10 mg/mL DTAC, the mean size diminishes further as the distribution becomes bimodal. Comparing to the PTAK:DTAC sample at 10 mg/mL DTAC in **Figure 3.9D**, it appears as if the broad distribution centered about 8.4×10^3

(22 nm) bifurcates into two narrow distribution characterized by a lower and a higher peak relaxation time of 4.0 x 10^3 μs (11 nm) and 1.9 x 10^4 μs (50 nm), respectively.

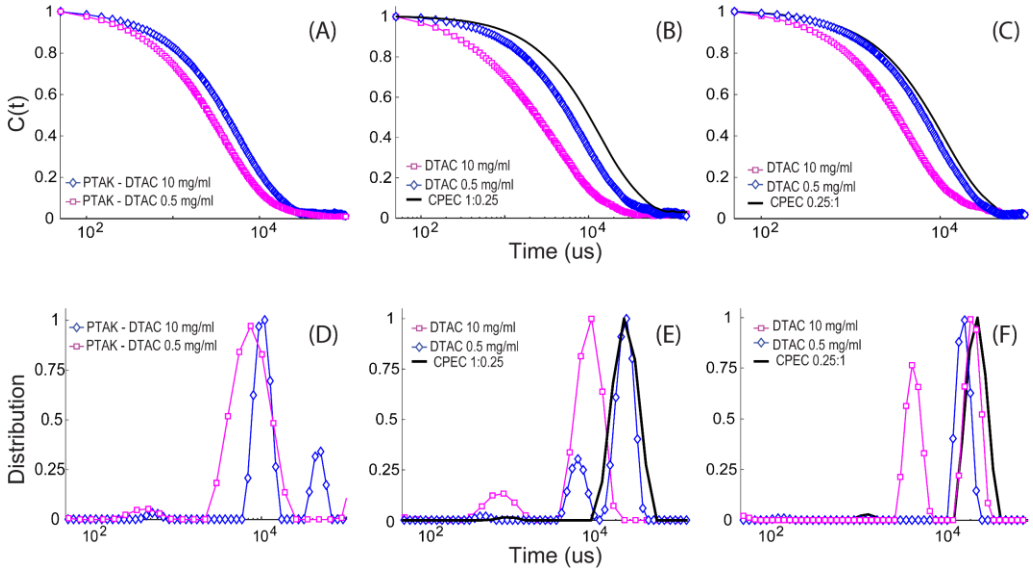

Figure 3.9 Normalized autocorrelation functions of (A) PTAK-DTAC complexes (B) CPEC-DTAC complexes with PFPI:PTAK at molar charger ratio of 1:0.25 and (C) CPEC-DTAC complexes with PFPI:PTAK at molar charger ratio of 0.25:1. Corresponding relaxation time spectra profiles for (D) PTAK-DTAC complexes, (E) CPEC-DTAC complexes with PFPI:PTAK at molar charger ratio of 1:0.25 and (F) CPEC-DTAC complexes with PFPI:PTAK at molar charger ratio of 0.25:1 were obtained by the CONTIN program are shown below. Isolated PTAK is not shown due to its poor scattering.

3.4 Discussion

Our results show that, for nonstoichiometric CPECs, micelles containing ionic surfactants with a charge opposite to the excess CPE are effective at uncoupling the CPEC and thereby shutting off inter-CPE EET. Neither the absolute sign of the charge on the ionic surfactant nor the precise chemical structure of the excess CPE seem to be important. Unlike initial formation of a CPEC, micelle-induced CPEC disassembly readily takes place at room temperature or if heated to ~ 70 ºC, implying that this

process has a low activation barrier and a relatively large thermodynamic driving force. Though there are significant similarities between the influence of SDS and DTAC on the corresponding CPEC, here are several differences between the two systems that are worth highlighting. We note in passing that our preliminary work suggests that replacing the charged group on the dodecyl surfactant with nonionic tetra- or penta-ethyleneoxide groups does not lead to decoupling of the CPEs within the CPEC. At relatively large concentrations well in excess of the critical micelle concentration, the CPEC/nonionic surfactant system appears undergo liquid/liquid phase separation phase separation, the detailed investigation of which is beyond the scope of this paper.

First, in the case of PFPI, increasing concentrations of SDS progressively increased the mean size of the scattering particles. The PL spectrum indicated that relatively extended PFPI chains formed in solution both below and above the nominal SDS cmc. Given that EET is effectively largely shut off when the concentration of SDS exceeds its nominal cmc, what is the nature of the large structures formed in solution at these SDS concentrations? We believe that the bimodal DLS relaxation time distribution provides a hint. The evidently significantly stronger interaction between PFPI and SDS relative to PFPI and PTAK leads to PFPI binding to SDS micelles, which induces chain straightening, leading to an increase in the PL quantum yield of PFPI. Above the cmc of SDS, the smaller size of 129 nm likely corresponds PFPI chains wrapped around several SDS micelles. The slow mode corresponding to 717 nm is likely then associated with a large cluster of many SDS micelles bridged via a single or multiple PFPI chains.

In contrast, the steady-state photophysics of corresponding DTAC-containing solutions showed that the PTAK chain becomes more kinked, leading to shorter conjugation lengths, compared to the CPEC in the absence of DTAC. This suggests that the physical structure of the PTAK/DTAC assembly. The significant blueshift observed in PTAK OD and PL takes place well below the DTAC cmc, indicating that its origin is not due to micelle formation. We propose that the PTAK backbone itself templates a cylindrical-micelle-type phase, where each monomer sidechain is ionically associated with multiple surfactant molecules, which effectively form a shell around the polymer. For this structure to be thermodynamically stable, and because the total molar concentration of DTAC is substantially larger than PTAK, DTAC must be in molar *local* excess with respect to PTAK sidechains, effectively over-charging the PTAK:DTAC assembly. It is possible that the reason the PTAK conjugation length is lowered in the presence of DTAC is because this maximizes aliphatic interactions between the tails of PTAK-bound surfactants. This is illustrated in the cartoon in Figure 10. We speculate that the larger inter-monomer repulsion due to doubly charged PFPI sidechains largely precludes formation of such kinked short-conjugation structures.

There is another intriguing difference between the 1:0.25 and 0.25:1 CPECs with both SDS and DTAC above their respective cmc's. In the case of SDS, the spectroscopy data suggested that the solution could be described as a combination of isolated PTAK and PFPI:SDS assembly spectra. In the case of DTAC, this was no longer the case: Although EET was similarly largely shut off between the two CPEs, PFPI assumed a fairly emissive state. This was in stark contrast to control PFPI:DTAC solutions, where the PFPI was found to be coiled into a poorly emissive state. This implies that the state

of PFPI in the presence of DTAC is qualitatively altered in the presence of PFPI. It is surprising that PTAK is able to influence PFPI despite being separated from it through a distance, over which EET is inefficient. This suggests that PFPI may be incorporated into PTAK:DTAC assemblies surfactant molecules bridging the two CPEs. We believe that the larger structures seen in the DLS of CPEC/DTAC solutions at 10 mg/mL DTAC correspond to such ternary assemblies that lack intimate contact between the two CPEs. However, the precise nature of such assemblies is difficult to ascertain at the moment.

3.5 Conclusion

In summary, we have investigated the influence of ionic surfactants of opposite charge but the same aliphatic tail on complexation and energy transfer between oppositely charged CPEs in water. Although the inter-conjugated polyelectrolyte complex is thermodynamically quite stable, we find that ionic surfactants of either sign can uncouple the complex and thereby shut off inter-polyelectrolyte electronic energy transfer at room temperature. This is significant from the point of view of photoprotection, where the ability to manipulate the light-harvesting efficiency via the state of assembly at different illumination flux levels can help prevent photoinduced damage. Although the sign of the surfactant seems to relatively unimportant, nevertheless, the structural evolution of each polymer does appear to depend on the sign of the surfactant charge and the polymer structure. In future work, the influence of polymer backbone microstructure and ionic charge density on the structural evolution should be deconvolved from the influence of surfactant sign.

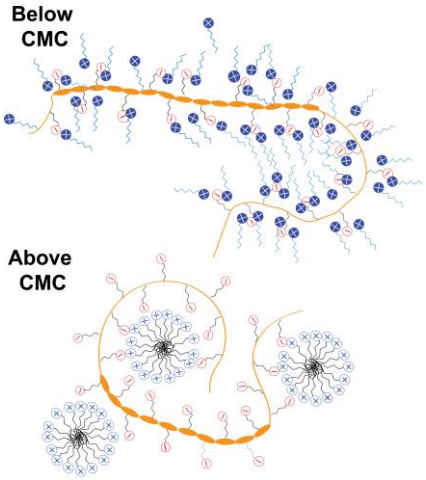

Figure 3.10. Cartoon illustrating the influence DTAC above and below its cmc on the conjugation length of the PTAK backbone.

3.6 References

1. Duarte, A.; Pu, K. Y.; Liu, B. & Bazan, G. C. Recent Advances in Conjugated Polyelectrolytes for Emerging Optoelectronic Applications. *Chem. Mater.* **2011,** 23, 501–515.
2. Choi, H.; Mai, C.K.; Kim, H.B.; Jeong, J.; Song, S.; Bazan, G.C.; Kim, J.Y.; Heeger, A.J. Conjugated Polyelectrolyte Hole Transport Layer for Inverted-Type Perovskite Solar Cells. *Nat. Commun.* **2015,** 6, 7348.
3. Liu, X.; Fan, Q.; Huang, W. DNA Biosensors Based on Water-Soluble Conjugated Polymers. *Biosens. Bioelectron.* **2011,** 26, 2154–2164.
4. Liu, Y.; Ogawa, K.; Schanze, K. S. Conjugated Polyelectrolytes as Fluorescent Sensors. *J. Photochem. Photobiol. C Photochem. Rev.* **2009,** 10, 173–190.
5. Wang, F.; Li, M.; Wang, B.; Zhang, J.; Cheng, Y.; Liu, L.; Lv, F.; Wang, S. Synthesis and Characterization of Water-Soluble Polythiophene Derivatives for Cell Imaging. *Sci. Rep.* **2018,** 5, 1–8.
6. Huang, Y.; Song, C.; Li, H.; Zhang, R.; Jiang, R.; Liu, X.; Zhang, G.; Fan, Q.; Wang, L.; Huang, W. Cationic Conjugated Polymer/Hyaluronan-Doxorubicin Complex for Sensitive Fluorescence Detection of Hyaluronidase and Tumor-Targeting Drug Delivery and Imaging. *ACS Appl. Mater. Interfaces* **2015,** 7, 21529–21537.
7. Feng, G.; Mai, C. K.; Zhan, R.; Bazan, G. C.; & Liu, B. Narrow Band Gap Conjugated Polyelectrolytes for Photothermal Killing of Bacteria. *J. Mater. Chem. B* **2015,** 3, 7340–7346.
8. Wang, Y.; Schanze, K. S.; Chi, E. Y.; Whitten, D. G. When worlds collide:

Interactions at the Interface between Biological Systems and Synthetic Cationic Conjugated Polyelectrolytes and Oligomers. *Langmuir* **2013,** 29, 10635–10647.

9. Costa, T.; Marques, A.T.; Seixas de Melo, J.S.; Thomas, A.W.; Garner, L.E.; Logan, E.; Scherf, U.; Bazan, G.C.; Burrows, H.D. Self-Assembly of Poly{1,4-phenylene-[9,9-bis(4-phenoxy-butylsulfonate)]fluorene-2,7-diyl} with Oppositely Charged Phenylenevinylene Oligoelectrolytes. *J. Phys. Chem. B* **2014,** 118, 613–23.
10. Fan, C.; Wang, S.; Hong, J.W.; Bazan, G.C.; Plaxco, K.W.; Heeger, A. J. Beyond Superquenching: Hyper-Efficient Energy Transfer from Conjugated Polymers to Gold Nanoparticles. *Proc. Natl. Acad. Sci.* **2003,** 100, 6297–6301.
11. Marques, A. T.; Burrows, H.D.; Melo, J. S. S. d.; Valente, A. J. M.; Justino, L. L. G.; Scherf, U.; Fron, E.; Rocha, S.; Hofkens, J.; Snedden, E.W.; Monkman, A. P. Spectroscopic Properties, Excitation, and Electron Transfer in an Anionic Water-Soluble Poly(fluorene-alt-phenylene)-perylenediimide Copolymer. *J. Phys. Chem. B* **2012,** 112, 7548–7559.
12. Evans, R. C. Harnessing Self-Assembly Strategies for the Rational Design of Conjugated Polymer Based Materials. *J. Mater. Chem. C* **2013,** 27, 4190.
13. Evans, R. C.; Knaapila, M.; Willis-Fox, N.; Kraft, M.; Terry, A.; Burrows, H.D.; Scherf, U. Cationic Polythiophene-Surfactant Self-Assembly Complexes: Phase Transitions, Optical Response. *Langmuir* **2012,** 28, 12348–56.
14. Li, D.; Wagner, N. J. Universal Binding Behavior for Ionic Alkyl Surfactants

with Oppositely Charged Polyelectrolytes. *J. Am. Chem. Soc.* **2013,** 135, 17547–17555 (2013).

15. Treger, J. S.; Ma,V.Y.; Gao, Y.; Wang, C.C.; Wang, H.L.; Johal, M.S. Tuning the Optical Properties of a Water-Soluble Cationic Poly(p-phenylenevinylene): Surfactant Complexation with a Conjugated Polyelectrolyte. *J. Phys. Chem. B* **2008,** 112, 760–763.
16. Costa, T.; Garner, L.E.; Knaapila, M.; Thomaks, A.W.; Rogers, S.E.; Bazan, G.C.; Burrows, H.D. Aggregation Properties of P-phenylene Vinylene Based Conjugated Oligoelectrolytes with Surfactants. *Langmuir* **2013,** 29, 10047–58.
17. Stewart, B.; Burrows, H. D. Molecular Dynamics Study of Self-Assembly of Aqueous Solutions of in the Presence of Pentaethylene Glycol. Materials **2016**, 9, 379.
18. Costa, T.; Azevedo, D. D.; Stewart, B.; Knaapila, M.; Valente, A. J. M.; Kraft, M.; Scherf, U.; Burrows, H. D. Interactions of a Zwitterionic Thiophene-Based Conjugated Polymer with Surfactants. *Polym. Chem.* **2015,** 6, 8036–8046.
19. Knaapila, M.; Evans, R.C.; Gutacker, A.; Garamus, V.M.; Szekely, N. K.; Schef, U.; Burrows, H.D. Conjugated Polyelectrolyte (CPE) Poly[3-[6-(N-methylimidazolium)hexyl]-2,5-thiophene] Complexed with Aqueous Sodium Dodecylsulfate Amphiphile: Synthesis, Solution Structure and "Surfactochromic" Properties. *Soft Matter* **2011,** 7, 6863.
20. Knaapila, M.; Stewart, B.; Costa, T.; Rogers, S. E.; Pragana, J.; Fonseca, S.M.; Valente, A. J. M.; Ramos, M. L.; Murtinho, D.; Costa Pereira, J.; Mallavia, R.;

Burrows, H. D. Incorporation of a Cationic Conjugated Polyelectrolyte CPE within an Aqueous Poly(vinyl alcohol) Sol. *Macromolecules* **2016,** 49, 9119–9131.

21. Monteserín, M.; Burrows, H. D.; Valente, A. J. M.; Lobo, V. M. M.; Mallavia, R.; Tapia, M. J.; Garcia-Zubiri, I. X.; Di Paolo, R. E.; Macanita, A. L. Modulating the Emission Intensity of Poly-(9,9-bis(6‘- *N* , *N* , *N* - trimethylammonium)hexyl)-Fluorene Phenylene) Bromide Through Interaction with Sodium Alkylsulfonate Surfactants. *J. Phys. Chem. B* **2007,** 111, 13560–13569.
22. Knaapila, M.; Almasy, L.; Garamus, V. M.; Pearson, C.; Pradhan, S.; Petty, M. C.; Scherf, U.; Burrows, H.D.; Monkman, A. P. Solubilization of Polyelectrolytic Hairy-Rod Polyfluorene in Aqueous Solutions of Nonionic Surfactant. *J. Phys. Chem. B* **2006,** 110, 10248–10257.
23. Burrows, H. D. Valente, A. J. M.; Costa, T.; Stewart, B.; Tapia, M. J.; Scherf, U. What Conjugated Polyelectrolytes Tell us About Aggregation in Polyelectrolyte/Surfactant Systems. *J. Mol. Liq.* **2015,** 210, 82−99.
24. Knaapila, M.; Evans, R. C.; Garamus, V. M.; Almasy, L.; Szekely, N.; Gutacker, A.; Schef, U.; Burrows, H.D. Structure and ‘Surfactochromic’ Properties of Conjugated Polyelectrolyte (CPE): Surfactant Complexes Between a Cationic Polythiophene and SDS in Water. *Langmuir* **2010,** 26, 15634–15643.
25. Monteserín, M.; Burrows, H. D.; Mallavia, R.; Di Paolo, R. E.; Maçanita, A. L.; Tapia, M. J. How to Change the Aggregation in the

DNA/Surfactant/Cationic Conjugated Polyelectrolyte System through the Order of Component Addition: Anionic versus Neutral Surfactants. *Langmuir* **2010,** 26, 11705–14.

26. Burrows, H. D.; Knaapila, M.; Monkman, A. P.; Tapia, M. J.;Fonseca1, S. M.; Ramos, M. L.; Pyckhout-Hintzen, W.; Pradhan, S.; Scherf,U. Structural Studies on Cationic Poly { 9 , 9- bis [6- (N , N , N -trimethylammo- nium) alkyl] fluorene- co -1 , 4-phenylene } Iodides in Aqueous Solutions in the Presence of the Non-Ionic Surfactant Pentaethyleneglycol Monododecyl Ether (C 12 E 5). *J. Phys. Condens. Matter* **2018,** 20, 104210.
27. Burrows, H. D.; Tapia, M. J.; Silva, C. L.; Pais, A. A. C. C.; Fonseca, S. M.; Pina, J.; Seixas de Melo, J.; Wang, Y.; Marques, E. F.; Knaapila, M.; Monkman, A. P.; Garamus, V. M.; Pradhan, S.; Scherf, U. Interplay of Electrostatic and Hydrophobic Effects with Binding of Cationic Gemini Surfactants and a Conjugated Polyanion: Experimental and Molecular Modeling Studies. *J. Phys. Chem. B* **2017,** 111, 4401–4410.
28. Hollingsworth, W. R.; Segura, C.; Balderrama, J.; Lopez., Schleissner, P.; Ayzner, A., Exciton Transfer and Emergent Excitonic States in Oppositely-Charged Conjugated Polyelectrolyte Complexes. *J. Phys. Chem. B* **2016,** 120, 7767–7774.
29. Paillet, S., Grassl, B. & Desbrières, J. Rapid and Quantitative Determination of Critical Micelle Concentration by Automatic Continuous Mixing and Static Light Scattering. *Anal. Chim. Acta* **2009,** 636, 236–241.
30. Spano, F. C. & Silva, C. H- and J-aggregate Behavior in Polymeric

Semiconductors. *Annu. Rev. Phys. Chem.* **2014,** 65, 477–500.

31. Provencher, S. W. Contin: A General Purpose Constrainded Regularization Program for Inverting Noisy Linear Algebraic and Integral Equations. *Comput. Phys. Commun.* **1984,** 35, C-818-C-819.

32. Scotti, A.; Liu, W.; Hyatt, J. S.; Herman, E. S.; Choi, H. S.; Kim, J. W.; Lyon, L. A.; Gasser, U.; Fernandez-Nieves, A. The CONTIN Algorithm and its Application to Determine the Size Distribution of Microgel Suspensions. *J. Chem. Phys.* **2015,** 142, 234905.

33. Sedlak, M.; Republic, S. What Can Be Seen by Static and Dynamic Light Scattering in Polyelectrolyte Solutions and Mixtures? *Langmuir* **1999,** 15, 4045–4051.

34. Fritz, G., Bergmann, A.; Glatter, O. Evaluation of Small-Angle Scattering Data of Charged Particles using the Generalized Indirect Fourier Transformation Technique. *J. Chem. Phys.* **2000,** 113, 9733–9740.

35. Fu, J., Fares, H. M.; Schlenoff, J. B. Ion-Pairing Strength in Polyelectrolyte Complexes. *Macromolecules* **2017,** 50, 1066–1074.

36. Ospinal-Jiménez, M. & Pozzo, D. C. Structural Analysis of Protein Complexes with Sodium Alkyl Sulfates by Small-Angle Scattering and Polyacrylamide Gel Electrophoresis. *Langmuir* **2011,** 27, 928–935.

37. Glatter, O.; Kratky, O. *Small Angle X-ray Scattering*; Academic Press: New York, 1982: p 119-213.

38. Hollingsworth, W. R.; Magnanelli, T.J.; Segura, C.; Young, J.D.; Bragg, A.E.; Ayzner, A.L. Polyion Charge Ratio Determines Transition between Bright and

Dark Excitons in Donor/Acceptor Conjugated Polyelectrolyte Complexes. *J. Phys. Chem. C* **2018,** 122, 22280-22293.

39. Olaya-Castro, A. & Scholes, G. D. Energy Transfer from Förster-Dexter Theory to Quantum Coherent Light-Harvesting. *Int. Rev. Phys. Chem.* **2011,** 30, 49–77.

40. Scholes, G. D. Long -Range Resonance Energy Transfer in Molecular Systems . *Annu. Rev. Phys. Chem.* **2003,** 54, 57–87.

41. Prévost, S. & Gradzielski, M. SANS Investigation of the Microstructures in Catanionic Mixtures of SDS/DTAC and the Effect of Various Added Salts. *J. Colloid Interface Sci.* **2009,** 337,472–484.

42. Shang, B. Z., Wang, Z.; Larson, R. G. Effect of Headgroup Size, Charge, and Solvent Structure on Polymer-Micelle Interactions, Studied by Molecular Dynamics Simulations. *J. Phys. Chem. B* **2009,** 133, 15170–15180.

43. Klein,R.; D'Aguanno, B.. *Light Scattering. Principles and Development*, Chapter Static Scattering Properties of Colloidal Suspensions, Oxford University Press, 1996; pages 30‑102.

44. Tu, G. L.; Li, H. B.; Forster, M.; Heiderhoff, R.; Balk, L. J.; Sigel, R.; Scherf, U. Amphiphilic Conjugated Block Copolymers: Synthesis and Solvent-Selective Photoluminescence Quenching. *Small* **2007**, 3, 1001–1006.

Appendix of Supporting Information

Disassembly of an Inter-Conjugated Polyelectrolyte Complex using Ionic Surfactants

Carmen Segura, Marcos Lucero, Alexander L. Ayzner*

Spectroscopy of CPE Complexes with Anionic Surfactant

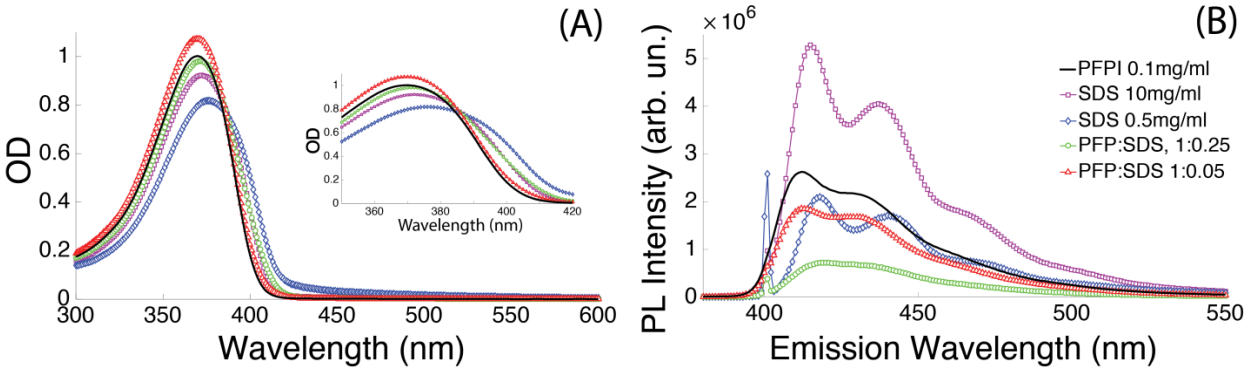

Figure A1. (A) UV-vis spectra and (B) emission spectra exciting at 400nm of aqueous solutions of PFPI-SDS complexes with varying concentrations of SDS at constant PFPI concentration of 0.1mg/ml for all complexes. Increased surfactant concentration above the molar charge equivalence of PFPI:SDS leads to an increased red shift as shown by the inset in panel (A). Above this molar charge equivalence of PFPI:SDS, the PFPI emission spectra shows a well resolved vibronic structure.

Spectroscopy of CPE Complexes with Cationic Surfactant

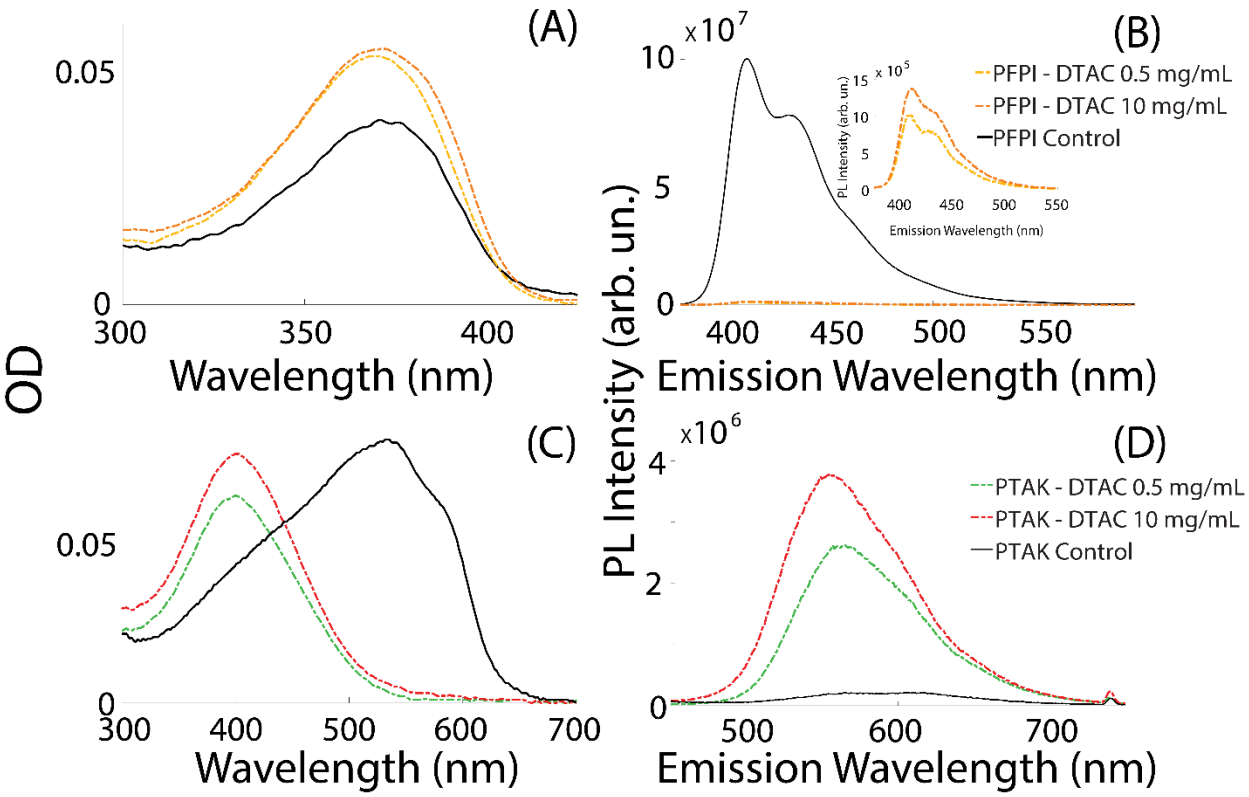

Figure A2. Top row shows the (A) UV-vis spectra and (B) emission spectra exciting at 400nm of aqueous solutions of PFPI-DTAC complexes with varying concentrations of DTAC. Due to the quenched emission of PFPI in the presence of DTAC, inset in panel (B) shows zoomed emission of PFPI in the presence of DTAC. Bottom row shows the (C) UV-vis spectra of and (D) emission spectra exciting at 400nm of aqueous solutions of PTAK-DTAC complexes with varying concentrations of DTAC.

PL Excitation Spectra of CPE Complexes with Cationic Surfactant

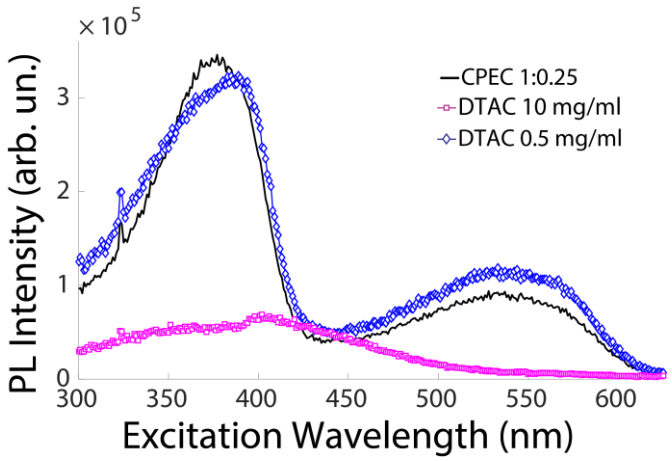

Figure A3. PL excitation spectra collected solely at a PTAK emission wavelenth (650 nm) for CPEC-DTAC complexes at the 1:0.25 CPEC composition above and below DTAC's cmc.

Small Angle X-ray Scattering

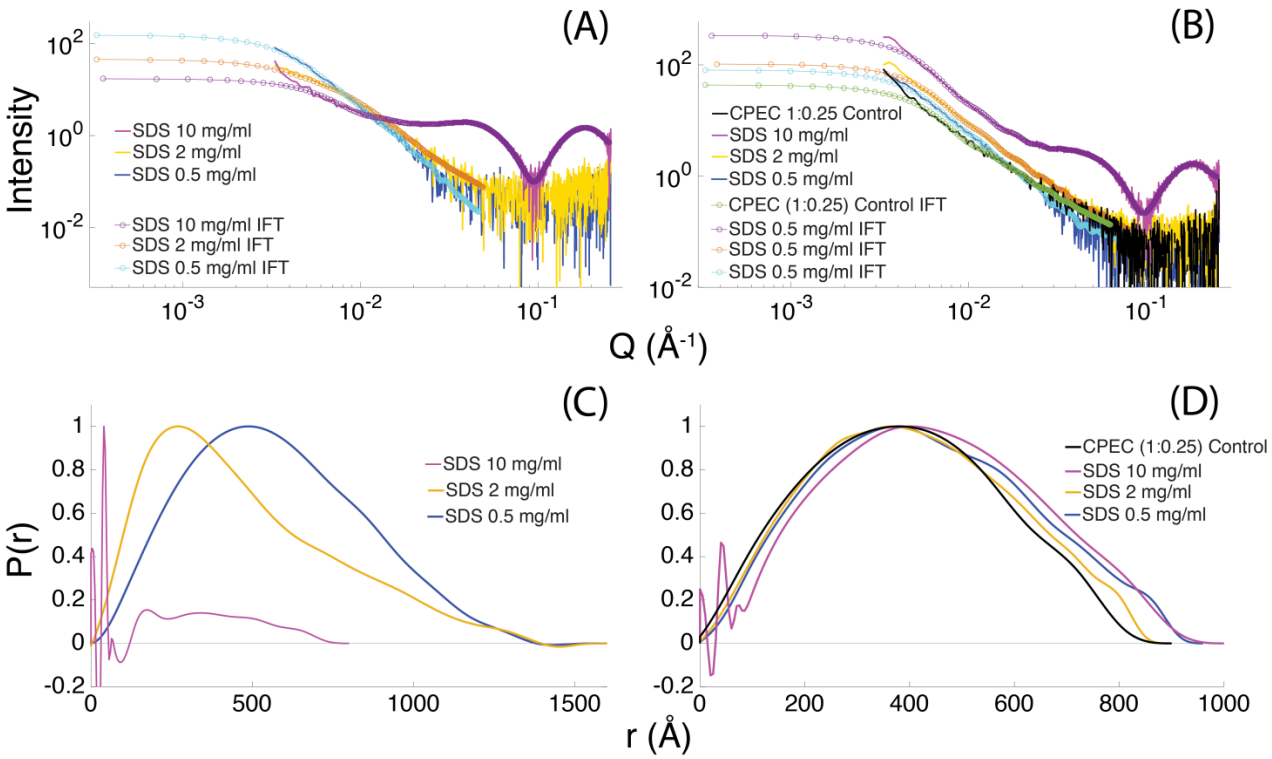

Figure A4. SAXS profiles of aqueous solutions of (A) PFPI-SDS complexes and (B) CPEC-SDS complexes. Corresponding pair distance distribution functions P(r) for (C) PFPI-SDS complexes and (D) CPEC-SDS complexes obtained by an indirect Fourier transformation process using the GIFT program are shown below.

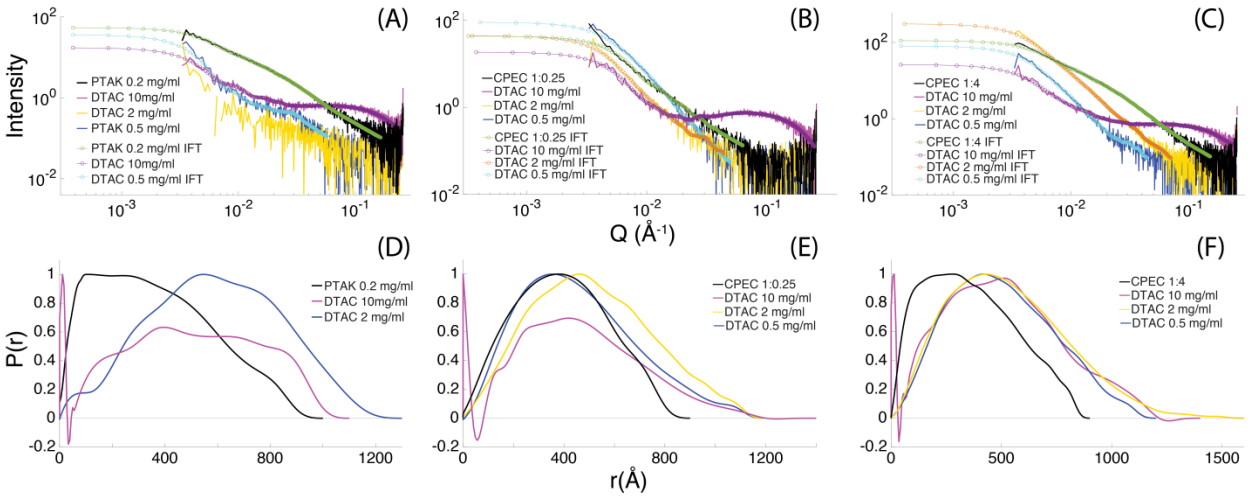

Figure A5. SAXS profiles of aqueous solutions of (A) PTAK-DTAC complexes (B) CPEC-DTAC complexes with PFPI:PTAK at molar charger ratio of 1:0.25 and (C) CPEC-DTAC complexes with PFPI:PTAK at molar charger ratio of 0.25:1. Corresponding pair distance distribution functions P(r) for (D) PTAK-DTAC complexes (E) CPEC-DTAC complexes with PFPI:PTAK at molar charger ratio of 1:0.25 and (F) CPEC-DTAC complexes with PFPI:PTAK at molar charger ratio of 0.25:1 obtained by an indirect Fourier transformation process using the GIFT program are shown below.

Dynamic Light Scattering

Table A3.1 CONTIN fit results of DLS autocorrelation functions from CPEC/surfactant solutions.

CPE	Surfactant	Surfactant Concentration (mg/ml)	Relaxation time (us)	R_H (nm) [a]	Relative Size Distribution (%)
PFPI	SDS	0.5	3.4×10^4	90	100
	SDS	2.0	2.8×10^4	90	100
	SDS	5.0	5.5×10^4	147	100
	SDS	10.0	5.6×10^4	148	100
PTAK	DTAC	0.5	1.1×10^4	30	79
			5.1×10^4	135	21
	DTAC	10	8.4×10^3	22	74
			1.6×10^5	431	26
CPEC (PFPI:PTAK)	**Surfactant**	**Surfactant Concentration (mg/mL)**	**Relaxation time (us)**	**R_H (nm) [a]**	**Relative Size Distribution (%)**
1:0.25	-	-	2.5×10^4	67	100
1:0.25	SDS	0.5	3.0×10^4	79	100
	SDS	2.0	8.7×10^3	23	48
			6.1×10^4	162	52
	SDS	5.0	3.9×10^4	102	100
	SDS	10.0	4.9×10^4	129	62
			2.7×10^5	717	38
1:0.25	DTAC	0.5	2.6×10^4	68	100
	DTAC	10.0	1.0×10^4	27	100
0.251:14	-	-	2.6×10^4	68	100
	DTAC	0.5	1.9×10^4	50	100
	DTAC	10.0	4.0×10^3	11	43
			1.9×10^4	50	57

[a] Intensity-weighted hydrodynamic radius from dynamic light scattering.

Chapter 4

Influence of Micelle Charge Density on Adsorption and Exciton Delocalization of Conjugated Polyelectrolytes

Abstract

Light harvesting with soft materials continues to be a diverse and highly active field. Among the large set of molecular light harvesters, conjugated polyelectrolytes (CPE) stand apart due to the chain connectivity of ionic subunits, and to the strong coupling between electronic and ionic degrees of freedom. This leads to a rich parameter space, within which the electronic structure and thus exciton dynamics of CPEs may be altered via ionic self-assembly in aqueous solution. Given the complexity of CPE interactions, substantial questions remain about precisely how soft molecular scaffolds can be used to tune the backbone electronic structure. In this manuscript, we have used ionic micelles as model soft assemblies, wherein by tuning the micelle composition, we have investigated the influence of surface charge density and sign of the surface charge on the CPE/micelle interaction. We find that both the micelle charge density and the precise arrangement of charged sidechains along the CPE together result in either contorted or highly extended CPE excitons.

4.1 Introduction

Motion of charge and energy along 1D and quasi-1D structures continues to be of general interest to chemists. This area includes highly diverse systems such as inorganic nanowires and DNA. Among soft-matter systems, quasi-1D conjugated-polymer-based materials have been attracting considerable attention for some time. This is primarily due to the dependence of their electronic and optical properties on the physical structure of the polymer chain – a property that has found use in several applications, including sensors,[1-3] solar cells,[4-5] transistors,[6-8] and hierarchical assemblies.[9] Backbone delocalization of π-electrons is responsible for the transport of both electric charge and excitation energy along the chain. Transport in these systems is highly anisotropic: Charge and energy transfer along the chain, and between π-stacked chains, is characterized by much larger mobilities than in the sidechain direction.[10]

Most conjugated polymers are soluble in organic solvents; however, for biomedical, sensing and general environmentally friendly applications, processability in water is often highly desired. This has given rise to a subset of conjugated polymers that bear ionic sidechains known as conjugated polyelectrolytes (CPEs).[11-12] CPEs possess fascinating characteristics due to the strong coupling between the electronic (backbone) and ionic (sidechain) degrees of freedom, leading to a strong simultaneous sensitivity of their photophysics to both ionic and hydrophobic interactions. Significant work has been done to take advantage of this coupling. In the biomedical field, it has been found that the interaction between certain CPEs and proteins can help identify different pathological protein states.[13-14] Further, the complexation of CPEs with

amyloid fibers has been implicated in a possible therapeutic role in Alzheimer's disease pathogenesis.[15-19] These and numerous additional examples highlight the promise and utility of CPEs in materials science.

CPEs are complex materials, and their interaction with biological systems is expected to be comparably complex. Simplified systems with a tractable degree of complexity are thus needed to elucidate the nature and strength of CPE-based interactions with other macromolecules. To this end, CPE-surfactant systems have received significant attention due to the ability to tune the surfactant phase in a relatively well-defined manner. These investigations have spanned several CPE chemical structures and surfactant types, including ionic and nonionic amphiphiles.[20-27] Though it remains challenging to form general conclusions, some specific results are worth highlighting. It is now well-established that CPEs interact strongly with ionic surfactants, forming complexes that can wildly vary the electronic absorption spectrum and the photoluminescence quantum yield of the CPE. Particularly remarkable changes in CPE photophysics appear to take place near the critical micelle concentration (cmc).[20] On the other hand, the interaction between CPEs and nonionic surfactants is evidently weaker compared to their ionic counterparts, though these systems can still alter the polymer chain conformation and aggregation.[26] The dependence of CPE optical properties on the length of the aliphatic tail of the surfactant is now relatively well-understood.[20]

Near the cmc, certain surfactants such as sodium dodecyl sulfate (SDS) not only modify the PL quantum yield of CPEs but also lead to a remarkable structuring of the PL spectrum, resulting in pronounced vibronic peaks.[20-21, 28] This implies that on

average the CPE backbone becomes significantly more planarized relative to its isolated state in aqueous solution, leading to a substantial increase in the π-electron delocalization length. This is quite intriguing, as the more delocalized the backbone valence electrons are, the more rapid the motion of charge and excitation energy along the backbone. Thus, such a modification of the CPE electronic wavefunction upon aqueous self-assembly is highly attractive for light-harvesting and sensing applications. Though this observation has been made with more than one CPE system, the fact that such backbone straightening is not observed for all CPEs and all oppositely charged micelles is interesting. This raises questions about the combined roles of CPE chemical structure, micelle surface charge and composition in determining the optical properties of the resulting complex. Additionally, it is important to characterize the nature of the CPE-macromolecule interaction for biomedical applications. The fact that the micelle charge and composition may be readily varied makes understanding the significantly more tractable CPE/micelle interaction of substantial biomedical relevance.

Furthermore, understanding the influence of micelle charge and surface composition on the optical properties of CPE/micelle complexes is of fundamental interest to light harvesting with soft ionic assemblies. Calver and Cosa, *et al.* have shown that CPEs may be adsorbed onto liposome surfaces along with small molecules that act as exciton acceptors with respect to the CPE.[28] In so doing, a directional, surface-bound exciton-transfer antenna is ionically assembled, which can be used to harvest a significant fraction of the visible spectrum. Understanding how to manipulate the electronic structure and thus the energy transfer rate as a function of the surface structure is expected to lead to more sensitive control of the light-harvesting efficiency.

In this manuscript, we focus on the following questions: How does the charge and composition of surfactant micelles alter their interaction with an oppositely charged CPE, andhow does the CPE backbone microstructure and charge density dictate the nature of its interaction with micelles of a given surface composition? To vary the surface charge/composition of the surfactant assemblies, we have varied the mole ratio of ionic and nonionic surfactant molecules with the same aliphatic tail length.[29] We find that, not only is the micelle charge critical to determining the photophysics of the assembly, but that the manner in which the composition of the micelle dictates optical properties of the CPE is highly sensitive to the chemical structure of the CPE backbone . Our results have important implications for the design of exciton-harvesting, polymer-based super-structures formed via ionic self-assembly.

4.2 Experimental Methods

Sample Preparation

The surfactants: sodium dodecyl sulfate (SDS, nominal cmc = 8mM) ≥99.0%, dodecyl trimethylammonium chloride (DTAC, nominal cmc = 20mM) ≥ 99.0% and pentaethylene glycol monododecyl ether ($C_{12}E_5$) ≥ 98.0% were obtained from Sigma-Aldrich. Mixed SDS/$C_{12}E_5$ micelle solutions of varying surfactant molar ratios were prepared to a total surfactant concentration of 35 mM. Mixed DTAC/$C_{12}E_5$ micelle solutions of varying surfactant molar ratios were prepared to a total surfactant concentration of 70 mM. Micelle solutions were heated while stirring for 2 hours at 70°C then allowed to cool to room temperature and equilibrate for two hours before characterization.

The cationic CPE derivative of poly(fluorene-alt-phenylene) (PFPI, average MW = 21,000 Da, PDI = 1.2) was obtained from Solaris Chem. A 10mg/ml stock solution of PFPI was prepared by heating the polymer in HPLC water at 70°C for 72 hours. The regioregular CPE derivative poly(butycarboxythiophene) derivative (RR PTAK, average MW=16,000 Da, PDI = 2.2) was obtained from Rieke Metals. Regiorandom PTAK (RA PTAK, average MW = 8,000 Da, PDI = 1.8) was obtained from Rieke Metals. The anionic conjugated polyelectrolyte poly(cyclopentadithieno-alt-phenylene) derivative (PDTPNa, average MW = 40,000 Da, PDI = 3) was obtained from 1-Material. 10mg/ml stock solutions of all three anionic conjugated polyelectrolytes were prepared by dissolving the conjugated polyelectrolytes in HPLC water and heating the stocks while stirring at 70°C for 24 hours. All materials were used as received.

Mixed SDS/$C_{12}E_5$ micelle solutions containing PFPI underwent the same preparation as control micelle solutions, where 0.1 mg/ml of PFPI was added after the 2-hour cooling period. Mixed DTAC/$C_{12}E_5$ micelle solutions containing anionic CPEs underwent the same preparation as control micelle solutions. The PTAK concentration was fixed to 0.12 mg/ml for both the regioregular and regiorandom PTAK. The PDTPNa concentration was fixed to 0.16 mg/mL for the DTAC/C12E5 mixed micelle solutions. Anionic conjugated polyelectrolytes were added to the mixed micelle solutions after the 2hr cooling period. All mixed micelle/CPE solutions were stirred for another 2 hours after CPE addition before characterization.

Small-Angle X-ray Scattering (SAXS)

SAXS measurements were performed at beamline 4−2 at the Stanford Synchrotron Radiation Laboratory (SSRL) using a fast readout photon counting detector (Pilatus3 X 1M). Samples in thin-wall quartz capillary cell were irradiated by a 11 keV X-ray (1.17 Å) at a sample to detector distance of 2.5 m. A set of 10 consecutive 1 s X-ray exposures were made on each sample at room temperature. The scattering of the background (HPLC water) was subtracted from solution scattering. To avoid degradation, the samples were oscillated during data collection. SasTool, a software package developed at SSRL, was used to convert collected 2D TIFF images to intensity vs scattering vector and to subtract solvent scattering. SAXS measurements were also performed at the Advanced Light Source (ALS, Lawrence Berkeley National Laboratory). Experiments were conducted with a 1.5 m sample-to-detector distance at 11 keV at the SIBYLS beamline. We found excellent agreement between measurements made at both synchrotron facilities.

Steady-State Spectroscopy

Optical density measurements were taken in 1.0 nm increments in a 1mm pathlength cuvette using a Shimadzu UV-2700 spectrophotometer over the range of 300−800 nm. Photoluminescence measurements were taken using a Horiba Fluoromax-4 spectrofluorometer in a right-angle geometry in cuvettes with 1 mm pathlengths. Emission spectra were measured at 1.0 nm increments exciting in the vicinity of λ_{max} from absorption spectra of the CPE/mixed-micelle solutions. Emission spectra were

corrected for the spectral responsivity of the detector and the wavelength dependent efficiency of the monochromators using factory-generated correction factors.

Time-Resolved Photoluminescence

Time-correlated single photon counting was carried out on a home-built apparatus. The excitation source was a pulsed Super K EXTREME (NKT Photonics) supercontinuum laser coupled to a Super K SELECT (NKT Photonics) acousto-optic filter and external RF driver (NKT Photonics) to select the wavelength of the excitation pulse. Measurements were carried out at a 78 MHz pulse repetition rate. The native largely horizontally polarized excitation pulse was first rotated 90° via an achromatic ½-λ plate (Thorlabs) before being linearly polarized via a Glan-Thompson polarizer (Thorlabs). Polarization of emitted light was selected using the same Glan-Thompson polarizer. Rotation of the polarization stages was controlled via motorized rotational stages (Thorlabs) under computer control. Emitted light was collimated and refocused onto the monochromator entrance slit by a set of achromatic doublets (Thorlabs). Long pass filters were used to minimize the influence of the reflected excitation beam. The emission wavelength was selected by an Acton Spectra Pro SP-2300 monochromator (Princeton Instruments), on which two detectors were mounted perpendicular to each other for steady-state and time-resolved measurements. An air-cooled PIXIS 100 CCD (Princeton Instruments) was used to record the steady-state spectra on the fly. A hybrid PMT with minimal after-pulsing (Becker and Hickl) was used to record time-resolved fluorescence decays. An SPC-130 photon counting module coupled to a Simple-Tau 130 table top TCSPC system (Becker and Hickl) was used for photon counting. For

magic-angle measurements, collection was carried out until approximately 10,000 photon counts were reached in the main channel. For anisotropy measurements, collection was carried out until approximately 10,000 counts were reached in the main channel under vertical-vertical conditions. The vertical-horizontal measurements were then carried out for the same amount of time.

After collection, magic-angle data was baselined by subtracting the average of the first 30 collected data points (prior to rise onset). All magic-angle decays were time-shifted such that the nominal t_0 occurred at the peak of the decay. Anisotropy data were time-shifted such that the half-rise time of respective VV and VH measurements were the same.

Fluorescence lifetimes were determined using the DecayFit MATLAB package due to Søren Preus, which utilizes non-linear least squares fitting to minimize the chi-square value obtained when convolving a trial multi-exponential decay function with the measured instrument response function (IRF). The IRF was measured using a scattering LUDOX solution. Goodness of fit was determined by minimized chi-square parameter and by visual inspection of the plotted residuals.

4.3 Results

In this work we have focused on two ionic surfactants with the same aliphatic tail length but opposite charge: sodium dodecyl sulfate (SDS) and dodecyl trimethylammonium chrloride (DTAC). We further focus on a single nonionic surfactant of the same aliphatic tail length and 5 ethylene oxide groups comprising the polar unit: $C_{12}E_5$ (E=ethylene oxide). The dependence of the CPE/surfactant interaction on the length of the surfactant's aliphatic and polar nonionic groups has previously

been explored. For ionic surfactants, it has been shown that the optical properties of CPE/surfactant complexes evolve in a nontrivial fashion below the surfactant cmc. Above the cmc, the optical density (OD) and the photoluminescence (PL) spectrum positions, intensities and shapes eventually reach a plateau. Since our interest is in understanding the interaction of CPEs with mixed micelles at the same total surfactant concentration, we have ensured that over the range of surfactant mixture compositions, both the nonionic and ionic surfactants remain above their mixed-micelle cmc. To correlate micelle structure with CPE chain microstructure and the resulting photophysics, we have performed a combination of solution small-angle

X-ray scattering (SAXS), steady-state OD and PL, as well as time-resolved PL and PL anisotropy measurements.

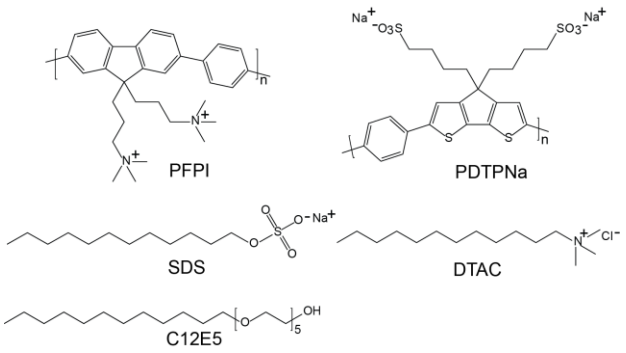

Figure 4.1 Chemical structures of the cationic CPE PFPI, the anionic surfactant SDS and the nonionic surfactant $C_{12}E_5$.

Mixed Anionic Micelles

We first examined mixed sodium dodecyl sulfate (SDS) micelles due to the preponderance of studies involving cationic CPEs with pure SDS. To probe the influence of SDS micelle composition, we used a derivative of poly(fluorene-alt-phenylene) (PFPI), whose chemical structure, along with those of SDS and the

nonionic surfactant $C_{12}E_5$, is shown in **Figure 4.1**. Micelle morphology before and after CPE addition was investigated by SAXS. **Figure 4.2A** shows the SAXS curves for

mixed micelles in the presence of PFPI. The trend in scattering from mixed micelles alone is nearly identical to that in the presence of PPFI; this is shown in the Supporting Information. Evidence of electron density contrast indicative of micelle dimensions is represented by two scattering peaks at low and high scattering vector length, q. A decrease in scattering intensity at low q is accompanied by a shift in the peak maximum at high q as the fraction of SDS, X_{SDS}, decreases. This trend suggests

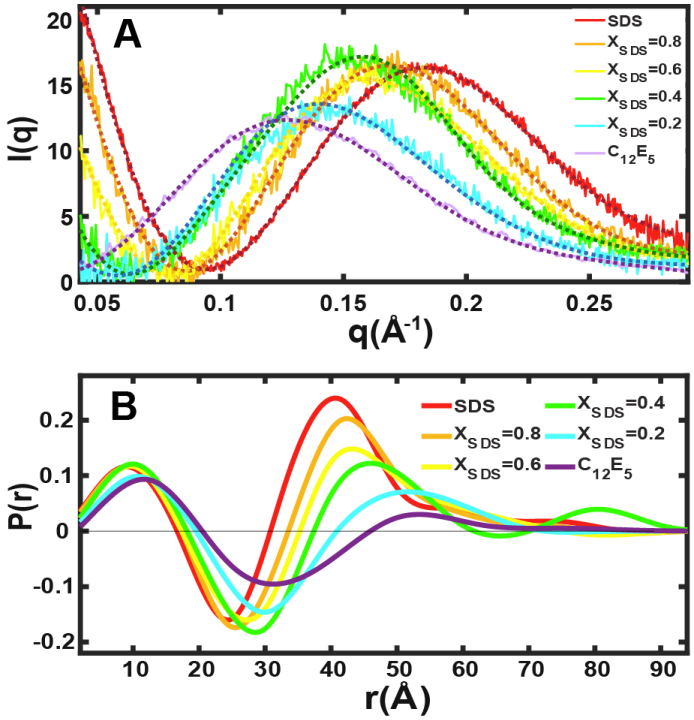

Figure 4.2 SAXS of mixed micelles with PFPI as a function of SDS mole fraction. (A) SAXS intensity as a function of q along with the corresponding Indirect Fourier Transform (IFT) fits (dashed curves). (B) Pair-distance distribution functions corresponding to the SAXS curves.

an increase in micelle size upon addition of $C_{12}E_5$. The intensity I(q) was analyzed via

Glatter's Indirect Fourier Transform method to obtain the real-space pair-distance distribution function, P(r) (**Figure 4.2B**).[30-35] The first peak in the P(r) has been attributed to the inner micelle structure, while the decay of the second peak defines the maximum dimension of the particle (D_{max}).[1] D_{max} for pure SDS micelle was found to be 81 Å corresponding to a radius of 40.5 Å. Considering the expected minimum dimension of SDS micelles with an extended chain and polar head group is 21.3 Å[1], the results suggest the formation of ellipsoidal micelles with a long-axis radius range of ~30-45 Å. Previous studies have shown that SDS and mixed anionic/nonionic micelles both preferentially form with an ellipsoidal morphology, while $C_{12}E_5$ alone is known to form lamellar type micelles.[1,4-6] The P(r) peak shifts also indicate micelle growth as the ratio of anionic to nonionic surfactant decreases. This can be attributed to the decrease in electrostatic repulsions between the SDS sulfate headgroups, as well as a possible decrease in steric interaction of the ethylene oxide headgroups when intercalating ionic and nonionic surfactant monomers. This decrease in steric free energy has been proposed to lead to micelles which adopt a lower-curvature structure, further supporting the possibility of ellipsoidal micelle formation.[29] Interestingly, the pure nonionic micelle solution is only found to scatter appreciably after the addition of PFPI, suggesting interactions between the ethylene oxide headgroups and PFPI may act as a nucleation site for micelle growth.

Visible clouding of mixed-micelle solutions was observed after the addition of polymer, while the pure surfactant micelle solutions remained clear after CPE addition. This suggests polymer addition leads to formation of large aggregated micelle-polymer complexes, which is accompanied by a noticeable drop in OD. These complexes remained stable at least on the time scale of multiple days. **Figure 4.3A** shows a clear drop in OD with a minimum absorbance found for X_{SDS} = 0.4. This is accompanied by the appearance of a long-wavelength light-scattering OD tail. **Figure 4.3B** shows that

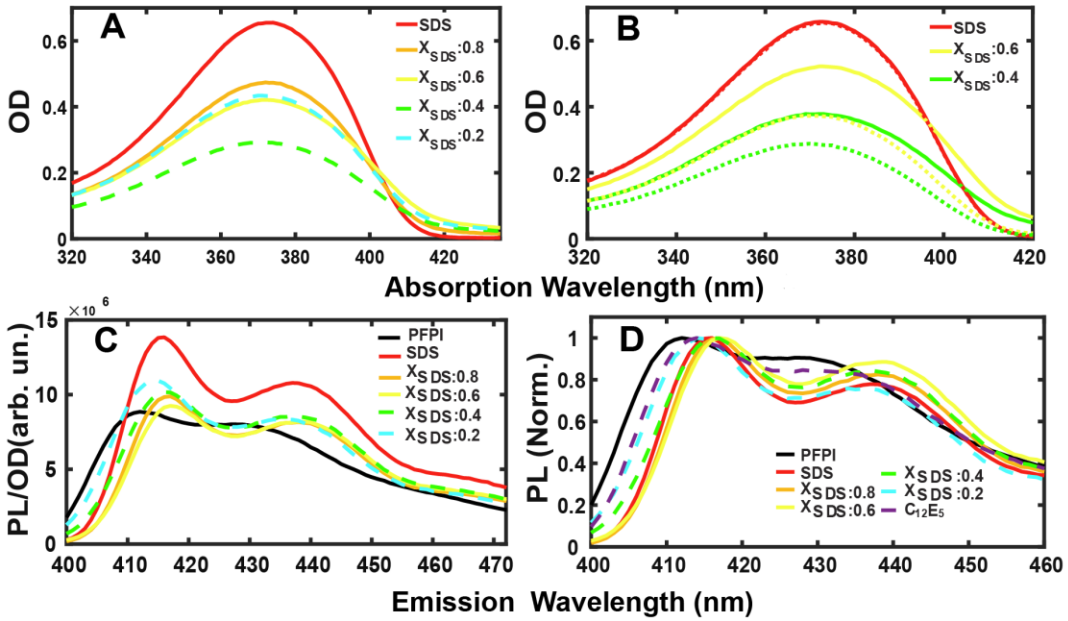

Figure 4.3 (A) OD of PFP/mixed SDS complexes. (B) OD of select mixed micelle compositions before and after centrifugation. Dashed lines represent samples after centrifugation, while solid lines of the same color represent samples as prepared. (C) PL spectra exciting at 370 nm normalized to the OD at the excitation wavelength. (D) PL spectra normalized to the maximum-intensity peak. The shorter-wavelength peak corresponds to the 0-0 vibronic transition, while the adjacent peak at longer wavelengths corresponds to the 0-1 transition.

upon centrifugation, a clear OD drop is observed for the turbid samples, while the absorbance of the pure SDS solution remains unchanged. Solutions prepared at X_{SDS} = 0.9 and X_{SDS} = 0.1 were also found to form clear solutions with minimal change in

absorbance after centrifugation. This suggests the stability of morphology of micelle/PFPI complexes is very sensitive to the anionic/nonionic surfactant ratio.

Changes in OD occur concomitantly with changes in the vibronic structure of PFPI emission upon addition of the CPE to micelle solutions at each micelle composition. Previous work has shown that the interaction of nonionic surfactants above the cmc with polyfluorene-based CPEs lead to the sharp structuring of emission spectrum accompanied by peak shifts.[7,8] The sharpening of the vibronic peaks is associated with a narrowing of the conformational CPE distribution, and the dominance of the 0-0 vibronic intensity near the spectrum onset implies that the PFPI backbone is significantly extended in the presence of SDS micelles. The molecular exciton model predicts that the nominal intensity ratio of the shorter-wavelength 0-0 to the adjacent longer-wavelength 0-1 vibronic peaks, S_R, reflects a competition between the intra-chain and inter-chain electronic couplings.[36] When the intra-chain coupling dominates, the 0-0 intensity contains a large fraction of the total PL intensity, thus increasing S_R above unity. In the opposite limit where inter-chain interactions lead to (partial) exciton delocalization over multiple chains or multiple chromophores along the same chain, the 0-0 intensity drops, thus lowering S_R.

Our mixed micelle-polymer systems show similar behavior with an increase in PL quantum yield observed with decreasing X_{SDS}. **Figure 4.3B** shows redshifts for all micelle compositions relative to pure PFPI. The largest redshift occurs for X_{SDS} where SDS dominates. This suggests micelles with larger surface charge ratios induce greater conformational changes of PFPI than micelles dominated by nonionic surfactant. However, electrostatic interactions as well as steric interactions play a role in PFPI

conformation as indicated by vibronic structuring and slight red shift of emission found for the nonionic micelle system.

Mixed Cationic Micelles

Is the CPE chain extension unique to the SDS micelle interaction, or can the CPE and micelle charges be reversed without qualitatively changing this observation? To answer this question, we examined the interaction of a CPE with a relatively similar backbone structure, with the fluorene subunit replaced by a dicyclopentathieno groups and bearing butylsulfate sidechains (PDTPNa), with DTAC. The respective chemical structures are shown in Scheme 1.

Figure 4.4 shows the SAXS curves and corresponding P(r) for DTAC micelles at various X_{DTAC} in the presence of PDTPNa. The data shows the presence of a micelle region and a monotonic change in the scattering intensity on the high-q end. Unlike with SDS, we do not observe a progressive shift in the micelle peak to lower q. The P(r) for the different SAXS curves shows a progressive change in the effective scattering contrast between the aliphatic interior and the polar surface. Decreasing X_{DTAC} leads to a shift to the high-q region shifts to higher q, which leads to a contraction of D_{max} by ~10 Å.

Figure 4.5A shows the influence of X_{DTAC} on the OD of PDTPNa, which is seen to be relatively mild. However, **Figure 4.5B** shows that the PL spectrum intensity depends strongly and nonmonotonically on X_{DTAC}, which is reminiscent of the behavior of PFPI. The big difference is that in its native state PDTPNa is very weakly emissive, and upon adding micelles at any composition, the polymer emission undergoes a large increase relative to the isolated polymer in aqueous solution. Interestingly, like PFPI, the vibronic structure of PDTPNa in the presence of micelles is highly pronounced with an $S_R > 1$, indicating substantial extension of the CPE backbone. This is highlighted by

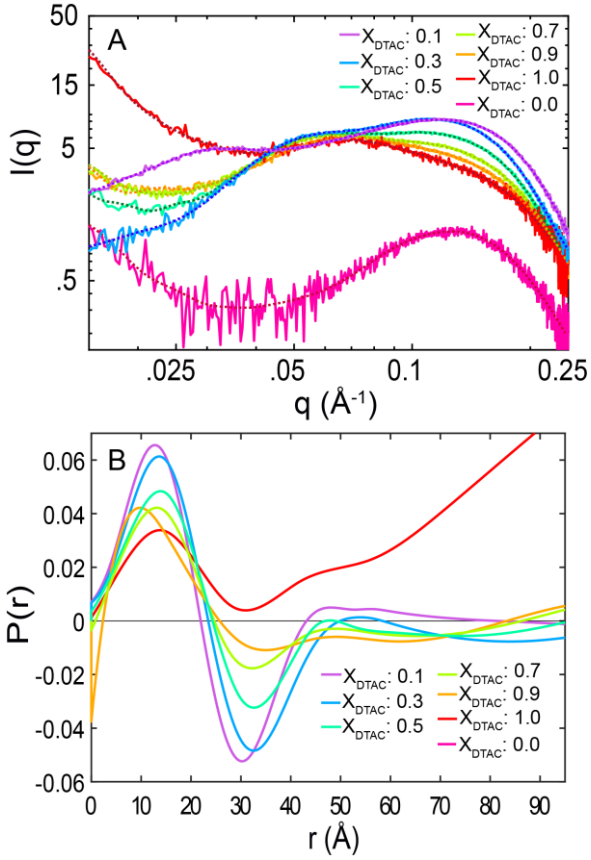

Figure 4.4 SAXS of mixed micelles with PDTPNA as a function of DTAC mole fraction. (A) SAXS intensity as a function of q along with the corresponding IFT fits (dashed curves). (B) Pair-distance distribution functions corresponding to the SAXS curves.

normalizing the PL spectrum to the 0-0 transition (**Figure 4.5C**). Like PFPI, $X_{DTAC} = 0$ corresponds to the most blue-shifted PL spectrum.

To elucidate whether the different trends we observe for the oppositely charged ionic micelles are due to the CPE charge density, we further examined the photophysics of regiorandom and regular poly(butylcarboxythiophene) (RA and RR PTAK, respectively) as a function of X_{DTAC}. Both of these CPE isomers have a singly charged monomer, which sidechain orientation varies rapidly as a function of position along the polymer backbone. **Figure 4.6A** and **Figure 4.6C** show the OD and the PL of RA PTAK, respectively. The data show that pure DTAC micelles lead to a drastic blueshift

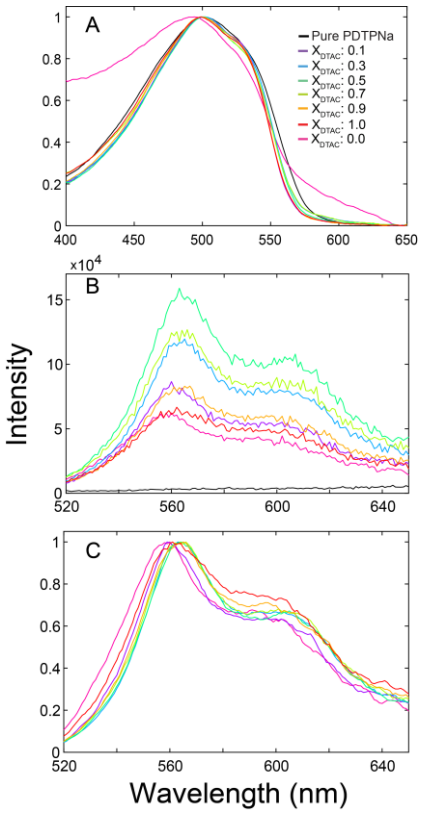

Figure 4.5 (A) Normalized OD of PDTPNa as a function of DTAC mole fraction. (B) Normalized PL corresponding to the OD in (A).

of the RA PTAK OD, which then monotonically shifts back to the red as X_{DTAC} is lowered, thereby decreasing the micelle surface charge density. The PL spectrum similarly shifts to the blue, though the intensity ordering of the nominal 0-0 and 0-1 PL transitions (to the extent that they can even be recognized) are opposite to that of PDTPNa.

Figure 4.6A and **Figure 4.6B** demonstrate that at $X_{DTAC} \geq 0.5$, the OD spectrum shapes and their trend as a function of X_{DTAC} are very similar for RA PTAK and RR

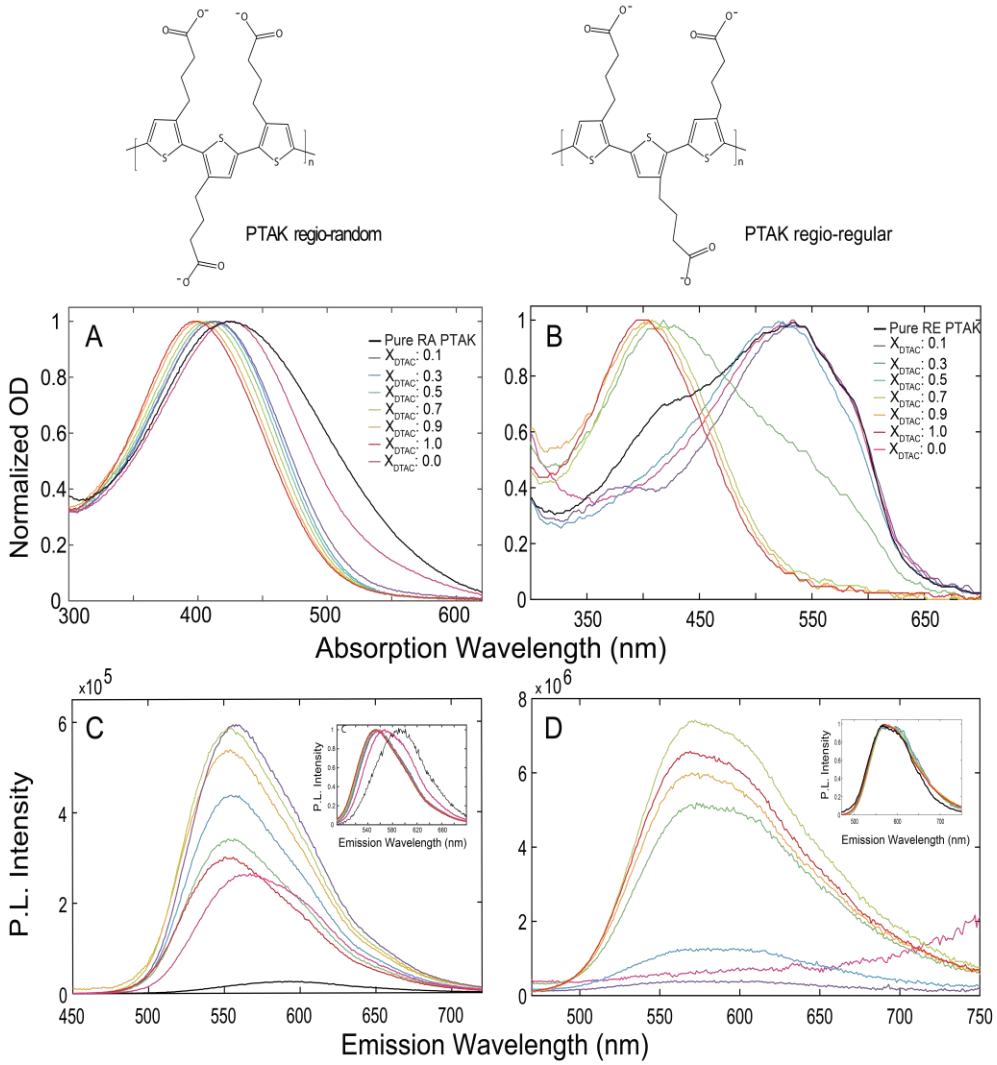

Figure 4.6 Top panels: OD of RA PTAK and diluted RE PTAK (A and B, respectively) as a function of X_{DTAC}. Bottom panels: PL of RA PTAK and diluted RE PTAK, respectively.

PTAK: Both become progressively more blue-shifted with increasing $X_{DTAC.}$ In the case of RR PTAK, it is clear that a structured red absorption band disappears as X_{DTAC} is increased. This corresponds to a break-up of intrachain π-stacking interactions as RR PTAK adsorbs onto the mixed micelle.

For both polymers, the OD-normalized PL intensity (**Figure 4.6C** and **Figure 4.6D**) increases sharply with X_{DTAC}, however, the trends show significant differences. The RR PTAK PL is clustered around the largest X_{DTAC}, whereas the PL of RA PTAK shows a more complex dependence on X_{DTAC}. Importantly, what is clear is that neither PTAK isomer displays the sharp, well-defined vibronic peaks that both PFPI and PDTPNa showed. Along with the blue shift in OD for the PTAK isomers upon adsorption onto the mixed micelle, the difference in S_R indicates that the CPE adsorption geometry depends sensitively on some combination of monomer charge density and relative sidechain orientation.

Radiative Exciton Dynamics

To form a better understanding of the photophysical properties of our CPE/mixed-micelle complexes, we have measured PL and PL anisotropy dynamics on nanosecond time scales. **Figure 4.7** shows time-resolved PL (top panels) and normalized time-resolved PL anisotropy decays (bottom panels) of PFPI and PDTPNa as a function of their respective mixed micelle composition. Pure PDTPNa has a distinct bi-exponential decay, which is dominated by a short ~269-ps component with a minority component of ~1 ns. The lifetime of the long component varies modestly with no obvious trend over the range of micellar conditions investigated – suggesting a fundamental decay lifetime of ~1 ns in solution. The lifetime of the short component

is uniquely sensitive to the conditions in solution. It increases upon addition of pure DTAC micelles and continues to climb as

X_{DTAC} is increased from 0 to 0.3. The rise in the short-component lifetime parallels a rise in the fractional contribution of the long component to the overall PL decay. The net effect is a dramatic (~2.5 x) increase in PDTPNa average fluorescence lifetime (from 337 ps to 859 ps), which is reflected in a large increase in steady-state PL quantum yield. This trend suggests that as X_{DTAC} is increased, PDTPNa adopts a more planar and rotationally hindered conformation relative to its state in isolation, and that individual PDTPNa strands are well-separated from one another with minimal π–π interaction.

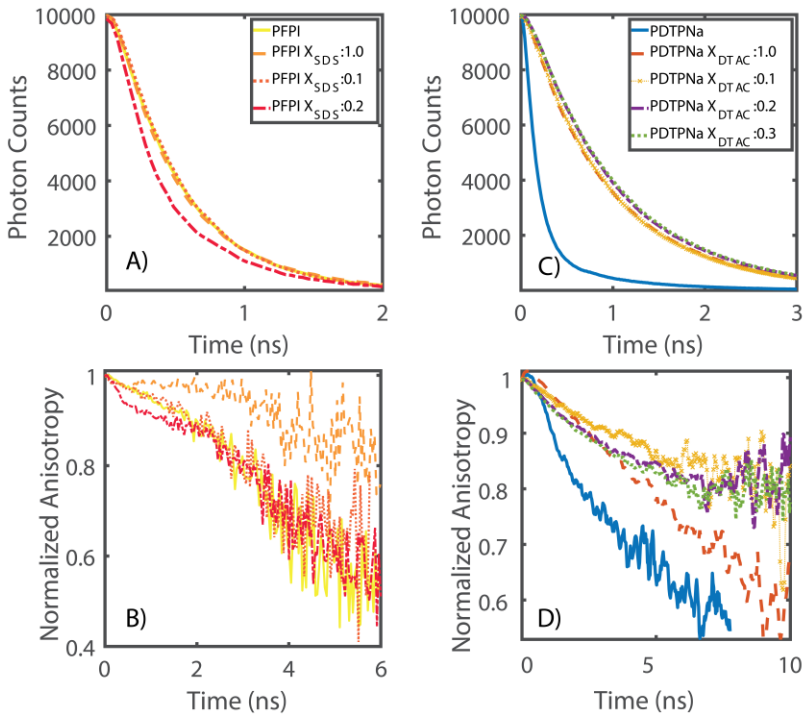

Figure 4.7 Panels A and C show time-resolved PL decays of , PFPI and PDTPNa (respectively) in isolated and micellar solutions. Panels B and D show normalized time resolved PL anisotropy decays of the CPEs under these same conditions.

The dynamics of PFPI similarly follow a bi-exponential decay law. The addition of SDS micelles increases the average fluorescence lifetime of PFPI by both increasing the lifetime of the short lifetime component while also increasing the fractional contribution of the long component. This trend persists when the X_{SDS} is changed to 0.1 but reverses sharply when the micelle composition reaches X_{SDS} = 0.4. The latter sample showed considerable cloudiness which, in conjunction with the sharp drop in fluorescence lifetimes (195 ps vs 402 ps for the 10:90 ratio), further suggests significant aggregation and compaction of PFPI strands. Compaction of CPE strands typically coincides with increased π–π interaction and the subsequent formation of non-emissive low energy states to which some fraction of excitons migrate via Förster-type exciton transfer.

Figure 4.8A and **Table 4.1** show time-resolved PL for both RA and RR PTAK and the corresponding fitting parameters, respectively, in isolated aqueous solution, as well as these CPEs with DTAC micelles in the composition region of interest. Pure RA PTAK exhibits a longer average lifetime than RR PTAK due to a lower propensity for intrachain π–π interaction owing to the irregularly spaced sidechain arrangement. Upon interaction with pure DTAC micelles, both types of PTAK achieve approximately the same fluorescence lifetime (~450 ps). This suggests that regardless of sidechain distribution, on average both achieve a similar final backbone microstate. Our measurements show that in mixed micelles, RR PTAK exhibits a very minor downward trend in average fluorescence lifetime as the percentage of ionic surfactant is increased(521 ps - 509 ps).

Figures 6B, D and 7B show normalized time-resolved anisotropy decays of the CPEs in isolated and micellar conditions. Because an anisotropy decay curve nominally reflects all possible modes of depolarization (e.g. exciton transfer, segmental motion, rotational diffusion of the CPE chain), it is, as a practical matter, difficult to disentangle multiple depolarization modes, except in the rare cases where they occur on very distinct time scales.[37-38] We expect, due to the size of the structures created via CPE-micelle interactions, that rotational depolarization is quite slow in relation to the PL lifetime of the CPE.

The anisotropy dynamics exhibit several broad trends that are worth noting. For both PDTPNa and RR PTAK (**Figure 4.7D** and **Figure 4.8B**, respectively), there is a clear move toward slower depolarization upon the inclusion of micelles in solution. This suggests modest (PDTPNa) to severe (PTAK) restriction of faster depolarization modes such as rotational motion and exciton transfer. This is presumably due to a

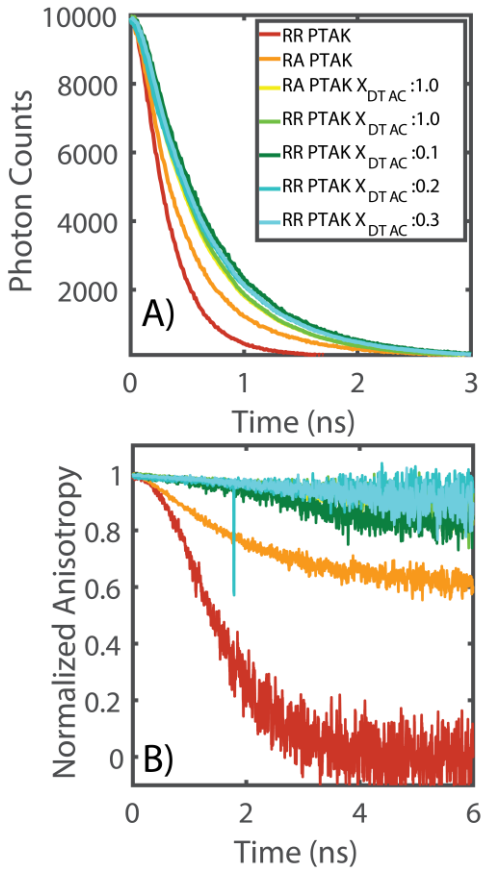

Figure 4.8 Panel A show time-resolved PL decays RA and RR PTAK (respectively) in isolated and micellar solutions. Panel B show normalized time resolved PL anisotropy decays of the CPEs under these same conditions.

break-up of intrachain π-stacking interactions and close association of the polyelectrolyte with the micelle surface. For PTAK, the latter is reasonable given the very slow anisotropy decay. Such a decay suggests that depolarization is dominated by

the overall motion of the CPE/micelle complex, which may be quite slow in relation to the PL lifetime.

Table 4.1 Time-resolved photoluminescence decay fitting parameters. All decays were fit to a bi-exponential model by non-linear least squares, with average fluorescence decay lifetimes reflected in the right-most column.

Sample	α_1	τ_1 (ns)	α_2	τ_2 (ns)	$\langle\tau\rangle$ (ns)
PDTPNa	0.9719	0.269	0.0281	0.982	0.337
PDTPNa X_{DTAC}=1.0	0.9172	0.364	0.0828	1.042	0.503
PDTPNa X_{DTAC}=0.1	0.7683	0.381	0.2317	0.989	0.648
PDTPNa X_{DTAC}=0.2	0.6469	0.482	0.3531	1.041	0.785
PDTPNa X_{DTAC}=0.3	0.5351	0.524	0.4649	1.052	0.859
Sample	α_1	τ_1 (ns)	α_2	τ_2 (ns)	$\langle\tau\rangle$ (ns)
PFPI	0.9054	0.204	0.0946	0.519	0.270
PFPI X_{SDS}=1.0	0.9458	0.290	0.0542	0.658	0.332
PFPI X_{SDS}=0.1	0.8504	0.354	0.1496	0.570	0.402
PFPI X_{SDS} =0.4	0.9917	0.184	0.0083	0.593	0.195
Sample	α_1	τ_1 (ns)	α_2	τ_2 (ns)	$\langle\tau\rangle$ (ns)
RR PTAK	0.9983	0.222	0.0017	0.689	0.224
RA PTAK	0.9873	0.297	0.0127	0.881	0.319
RR PTAK X_{DTAC}=1.0	0.8050	0.363	0.1950	0.675	0.460
RA PTAK X_{DTAC}=1.0	0.8722	0.369	0.1278	0.721	0.447
RR PTAK X_{DTAC}=0.1	0.7651	0.401	0.2349	0.734	0.521
RR PTAK X_{DTAC}=0.2	0.7255	0.375	0.2745	0.718	0.519
RR PTAK X_{DTAC}=0.3	0.7698	0.385	0.2302	0.718	0.504

4.4 Discussion

Our results show that with decreasing X_{SDS}, the PFPI extinction coefficient decreased before partially reversing when X_{SDS} dropped to 0.2. Within Spano's and Barford's exciton models, the extinction coefficient is expected to be a monotonically increasing function of the number of monomers associated with the average chromophore.[36, 39-41] We thus believe that the drop in OD with decreasing X_{SDS} is associated with a decrease in the average chromophore length. Although the 0-0 and 0-1 vibronic transitions in the PL spectrum remain quite sharp – surprisingly even for X_{SDS} as low as 0.2 – the nominal S_R also decreases with decreasing X_{SDS}.

At $X_{SDS} \leq 0.2$, the PL spectrum blue-shifts, while S_R remains largely unchanged. We interpret this as a decrease in the spatial extent of the exciton wavefunction of the ultimate emitting state. This is not surprising at such nominally low micelle charge densities. The fact that S_R stays approximately constant is somewhat surprising: It would be reasonable to expect S_R to decrease along with the blue-shift if the nonionic surfactants were distributed uniformly throughout the mixed micelle surface. We speculate that there exists a possibility for the formation of charged patches along the mixed-micelle surface. Though such a circumstance would increase the electrostatic free energy per micelle, it is feasible that the interaction with PFPI would stabilize such partial surfactant segregation within the mixed micelle.[29, 42-43]

Though the trend with X_{DTAC} is not quantitatively identical to that of X_{SDS}, the photophysics and radiative dynamics of PDTPNa as a function of X_{DTAC} are qualitatively similar to that of PFPI/SDS. This is consistent with the fact that (i) the sidechain orientation relative the backbone and the linear ionic charge density along

the backbone are similar to PFPI, and (ii) the *local* interactions between cationic quaternary methylammonium groups and anionic sulfonate groups are effectively shared by both PFPI/SDS and PDTPNa/DTAC.

Using molecular dynamics simulations, Shang and Larson *et al.* showed that, for the same dodecyl aliphatic tail, the sign of the surfactant charge was substantially more important in determining the micelle's interaction with the (neutral) poly(ethyleneoxide) (PEO) than the change in the head-group size between SDS and DTAC.[44] These authors also showed that the difference in interaction between water molecules and ions of opposite charge played a role in the different behavior exhibited by SDS and DTAC micelles in the presence of PEO. In our case, the local sidechain/micelle interactions are relatively similar for the PFPI/SDS and PDTPNa/DTAC. This suggests that their spectroscopic similarities can be tied to the adsorption geometry of the CPE on the mixed-micelle surface. Evidently, the structural constraint imposed by the bridging carbon atom that anchors the sidechains is quite severe, leading to substantial extension of the CPE backbone. This in turn leads to a well-structured PL spectrum with the 0-0 transition retaining most of the oscillator strength.

Unlike the PDTP/DTAC system, both PTAK isomers undergo substantial blueshifts in both OD and PL spectra upon binding to DTAC. Moreover, the vibronic PL peaks never become well-defined at any micelle composition. The combination of these observations points to a PTAK backbone, whose intrachain π-stacking interactions have been overcome in the act of binding to the micelle surface but whose

average microstructure is contorted along the surface. This leads to a bright emissive states albeit with a correspondingly small exciton delocalization length.

Our findings imply the following two broad takeaways. First, the spatial sidechain distribution along the backbone is of paramount importance when determining the average chain conformation upon binding to a charged micelle surface. Sidechain position was seen to lead to either highly structured or relatively featureless PL spectra, underscoring qualitative difference in the exciton delocalization along the adsorbed chain. For the doubly charged CPEs in this work the precise sidechain charge appeared relatively unimportant. If highly extended excitons are desired upon adsorption, then the branched two-sidechain arrangement is desired. On the other hand, for the singly charged monomers and a rapidly alternating sidechain orientation with respect to the backbone like in PTAK, the CPE is evidently unable to achieve highly extended conformations. This suggests that proper engineering of the backbone microstructure and linear charge density, the continuum of CPE microstructures spanning highly tortuous to highly extended states may be achieved.

Second, for a given CPE chemical structure, the micelle composition can be used to effectively manipulate the CPE adsorption geometry and thus its optoelectronic properties. We saw the PL intensity change by more than an order of magnitude for certain samples as a function of micelle composition. An intriguing possibility is the formation of charge patches on the micelle surface, which is expected to significantly alter the free energy of the CPE/micelle complex. We speculate that by judiciously engineering such patches may (i) allow for more flexibility in the adsorbed state, as well as (ii) allow access to certain adsorption geometries that would otherwise be

impossible. We envision that such characteristics may be leveraged for both light-harvesting and sensing applications.

4.5 Conclusion

In summary, we have shown that the micelle composition can be used to manipulate the excitonic wavefunction of a bound CPE. However, our results show that the change in CPE photophysics depends strongly on both the micelle charge and the ionic sidechains the CPE backbone. By varying the local monomer charge density, highly kinked as well as extended, highly emissive excitonic states may be achieved from kinked and extended microstructures .

4.6 References

1. Li, C.; Shi, G., Polythiophene-Based Optical Sensors for Small Molecules. *ACS Appl Mater Interfaces* **2013**, *5*, 4503-10.

2. Thomas, S. W.; Joly, G. D.; Swager, T. M., Chemical Sensors Based on Amplifying Fluorescent Conjugated Polymers. *Chemical Reviews* **2007**, *107*, 1339-1386.

3. Zhou, Q.; Swager, T. M., Fluorescent Chemosensors Based on Energy Migration in Conjugated Polymers: The Molecular Wire Approach to Increased Sensitivity. *Journal of the American Chemical Society* **1995**, *117*, 12593-12602.

4. Lu, L.; Zheng, T.; Wu, Q.; Schneider, A. M.; Zhao, D.; Yu, L., Recent Advances in Bulk Heterojunction Polymer Solar Cells. *Chemical Reviews* **2015**, *115*, 12666-12731.

5. Jenekhe, S. A.; Zhu, D., Conjugated Polymers. *Polymer Chemistry* **2013**, *4*, 5142-5143.

6. Wang, C.; Rivnay, J.; Himmelberger, S.; Vakhshouri, K.; Toney, M. F.; Gomez, E. D.; Salleo, A., Ultrathin Body Poly(3-Hexylthiophene) Transistors with Improved Short-Channel Performance. *ACS Appl Mater Interfaces* **2013**, *5*, 2342-6.

7. Rivnay, J.; Toney, M. F.; Zheng, Y.; Kauvar, I. V.; Chen, Z.; Wagner, V.; Facchetti, A.; Salleo, A., Unconventional Face-on Texture and Exceptional in-Plane Order of a High Mobility N-Type Polymer. *Adv Mater* **2010**, *22*, 4359-63.

8. Mei, J.; Kim do, H.; Ayzner, A. L.; Toney, M. F.; Bao, Z., Siloxane-Terminated Solubilizing Side Chains: Bringing Conjugated Polymer Backbones Closer and Boosting Hole Mobilities in Thin-Film Transistors. *J Am Chem Soc* **2011**, *133*, 20130-3.

9. Clark, A. P. Z.; Shi, C.; Ng, B. C.; Wilking, J. N.; Ayzner, A. L.; Stieg, A. Z.; Schwartz, B. J.; Mason, T. G.; Rubin, Y.; Tolbert, S. H., Self-Assembling Semiconducting Polymers—Rods and Gels from Electronic Materials. *ACS Nano* **2013**, *7*, 962-977.

10. Barford, W., Exciton Transfer Integrals between Polymer Chains. *J Chem Phys* **2007**, *126*, 134905.

11. Liu, B.; Bazan, G. C., *Conjugated Polyelectrolytes: Fundamentals and Applications*; Wiley, 2013.

12. Jiang, H.; Taranekar, P.; Reynolds, J. R.; Schanze, K. S., Conjugated Polyelectrolytes: Synthesis, Photophysics, and Applications. *Angew Chem Int Ed Engl* **2009**, *48*, 4300-16.

13. Wang, S.; Lv, F., *Functionalized Conjugated Polyelectrolytes: Design and Biomedical Applications*; Springer Berlin Heidelberg, 2013.

14. Duarte, A.; Pu, K.-Y.; Liu, B.; Bazan, G. C., Recent Advances in Conjugated Polyelectrolytes for Emerging Optoelectronic Applications. *Chemistry of Materials* **2011**, *23*, 501-515.

15. Dwivedi, A. K.; Iyer, P. K., Therapeutic Strategies to Prevent Alzheimer's Disease Pathogenesis Using a Fluorescent Conjugated Polyelectrolyte. *Macromol Biosci* **2014**, *14*, 508-14.

16. Ghosh, D., et al., Complexation of Amyloid Fibrils with Charged Conjugated Polymers. *Langmuir* **2014**, *30*, 3775-86.

17. Herland, A.; Thomsson, D.; Mirzov, O.; Scheblykin, I. G.; Inganäs, O., Decoration of Amyloid Fibrils with Luminescent Conjugated Polymers. *J. Mater. Chem.* **2008**, *18*, 126-132.

18. Margalith, I., et al., Polythiophenes Inhibit Prion Propagation by Stabilizing Prion Protein (Prp) Aggregates. *J Biol Chem* **2012**, *287*, 18872-87.

19. Wigenius, J.; Persson, G.; Widengren, J.; Inganas, O., Interactions between a Luminescent Conjugated Oligoelectrolyte and Insulin During Early Phases of Amyloid Formation. *Macromol Biosci* **2011**, *11*, 1120-7.

20. Monteserín, M.; Burrows, H. D.; Valente, A. J. M.; Lobo, V. M. M.; Mallavia, R.; Tapia, M. J.; García-Zubiri, I. X.; Di Paolo, R. E.; Maçanita, A. L., Modulating the Emission Intensity of Poly-(9,9-Bis(6‘-N,N,N-Trimethylammonium)Hexyl)-Fluorene Phenylene) Bromide through Interaction with Sodium Alkylsulfonate Surfactants. *The Journal of Physical Chemistry B* **2007**, *111*, 13560-13569.

21. Evans, R. C.; Knaapila, M.; Willis-Fox, N.; Kraft, M.; Terry, A.; Burrows, H. D.; Scherf, U., Cationic Polythiophene-Surfactant Self-Assembly Complexes: Phase Transitions, Optical Response, and Sensing. *Langmuir* **2012**, *28*, 12348-56.

22. Costa, T.; Garner, L. E.; Knaapila, M.; Thomas, A. W.; Rogers, S. E.; Bazan, G. C.; Burrows, H. D., Aggregation Properties of P-Phenylene Vinylene Based Conjugated Oligoelectrolytes with Surfactants. *Langmuir* **2013**, *29*, 10047-58.

23. Knaapila, M.; Evans, R. C.; Garamus, V. M.; Almasy, L.; Szekely, N. K.; Gutacker, A.; Scherf, U.; Burrows, H. D., Structure and "Surfactochromic" Properties of Conjugated Polyelectrolyte (Cpe): Surfactant Complexes between a Cationic Polythiophene and Sds in Water. *Langmuir* **2010**, *26*, 15634-43.

24. Monteserin, M.; Burrows, H. D.; Mallavia, R.; Di Paolo, R. E.; Macanita, A. L.; Tapia, M. J., How to Change the Aggregation in the DNA/Surfactant/Cationic Conjugated Polyelectrolyte System through the Order of Component Addition: Anionic Versus Neutral Surfactants. *Langmuir* **2010**, *26*, 11705-14.

25. Al Attar, H. A.; Monkman, A. P., Effect of Surfactant on Water-Soluble Conjugated Polymer Used in Biosensor. *The Journal of Physical Chemistry B* **2007**, *111*, 12418-12426.

26. Burrows, H. D.; Valente, A. J. M.; Costa, T.; Stewart, B.; Tapia, M. J.; Scherf, U., What Conjugated Polyelectrolytes Tell Us About Aggregation in Polyelectrolyte/Surfactant Systems. *Journal of Molecular Liquids* **2015**, *210*, 82-99.

27. Monteserín, M.; Burrows, H. D.; Valente, A. J. M.; Pais, A. A. C. C.; Di Paolo, R. E.; Maçanita, A. L.; Tapia, M. J., Fluorescence Enhancement of a Cationic Fluorene–Phenylene Conjugated Polyelectrolyte Induced by Nonionic N-Alkyl Polyoxyethylene Surfactants. *Langmuir* **2017**, *33*, 13350-13363.

28. Calver, C. F.; Schanze, K. S.; Cosa, G., Biomimetic Light-Harvesting Antenna Based on the Self-Assembly of Conjugated Polyelectrolytes Embedded within Lipid Membranes. *ACS Nano* **2016**, *10*, 10598-10605.

29. Shiloach, A.; Blankschtein, D., Predicting Micellar Solution Properties of Binary Surfactant Mixtures. *Langmuir* **1998**, *14*, 1618-1636.

30. Innerlohinger, J.; Wyss, H. M.; Glatter, O., Colloidal Systems with Attractive Interactions: Evaluation of Scattering Data Using the Generalized Indirect Fourier Transformation Method. *The Journal of Physical Chemistry B* **2004**, *108*, 18149-18157.

31. Ehmann, H. M. A.; Spirk, S.; Doliška, A.; Mohan, T.; Gössler, W.; Ribitsch, V.; Sfiligoj-Smole, M.; Stana-Kleinschek, K., Generalized Indirect Fourier Transformation as a Valuable Tool for the Structural Characterization of Aqueous Nanocrystalline Cellulose Suspensions by Small Angle X-Ray Scattering. *Langmuir* **2013**, *29*, 3740-3748.

32. Gerhard, F.; Otto, G., Structure and Interaction in Dense Colloidal Systems: Evaluation of Scattering Data by the Generalized Indirect Fourier Transformation Method. *Journal of Physics: Condensed Matter* **2006**, *18*, S2403.

33. Weyerich, B.; Brunner-Popela, J.; Glatter, O., Small-Angle Scattering of Interacting Particles. Ii. Generalized Indirect Fourier Transformation under Consideration of the Effective Structure Factor for Polydisperse Systems. *Journal of Applied Crystallography* **1999**, *32*, 197-209.

34. Brunner-Popela, J.; Glatter, O., Small-Angle Scattering of Interacting Particles. I. Basic Principles of a Global Evaluation Technique. *Journal of Applied Crystallography* **1997**, *30*, 431-442.

35. Glatter, O.; Kratky, O., *Small Angle X-Ray Scattering*; Academic Press, 1982.

36. Spano, F. C.; Silva, C., H- and J-Aggregate Behavior in Polymeric Semiconductors. *Annual Review of Physical Chemistry* **2014**, *65*, 477-500.

37. Cross, A. J.; Fleming, G. R., Analysis of Time-Resolved Fluorescence Anisotropy Decays. *Biophysical Journal* **1984**, *46*, 45-56.

38. Gochanour, C. R.; Andersen, H. C.; Fayer, M. D., Electronic Excited State Transport in Solution. *The Journal of Chemical Physics* **1979**, *70*, 4254-4271.

39. Yamagata, H.; Spano, F. C., Interplay between Intrachain and Interchain Interactions in Semiconducting Polymer Assemblies: The Hj-Aggregate Model. *J Chem Phys* **2012**, *136*, 184901.

40. Barford, W.; Marcus, M., Theory of Optical Transitions in Conjugated Polymers. I. Ideal Systems. *The Journal of Chemical Physics* **2014**, *141*, 164101.

41. Marcus, M.; Tozer, O. R.; Barford, W., Theory of Optical Transitions in Conjugated Polymers. Ii. Real Systems. *The Journal of Chemical Physics* **2014**, *141*, 164102.

42. Puvvada, S.; Blankschtein, D., Thermodynamic Description of Micellization, Phase Behavior, and Phase Separation of Aqueous Solutions of Surfactant Mixtures. *The Journal of Physical Chemistry* **1992**, *96*, 5567-5579.

43. Puvvada, S.; Blankschtein, D., Theoretical and Experimental Investigations of Micellar Properties of Aqueous Solutions Containing Binary Mixtures of Nonionic Surfactants. *The Journal of Physical Chemistry* **1992**, *96*, 5579-5592.

44. Shang, B. Z.; Wang, Z.; Larson, R. G., Molecular Dynamics Simulation of Interactions between a Sodium Dodecyl Sulfate Micelle and a Poly(Ethylene Oxide) Polymer. *The Journal of Physical Chemistry B* **2008**, *112*, 2888-2900.

Chapter 5

Layer-by-Layer Assembly of Oppositely Charged Conjugated Polyelectrolyte Complexes via a Cationic Lipid Membrane Template

Abstract

There has been an increase interest in developing new technologies for energy harvesting applications, one of which is using "soft" light-harvesting antennae composed of materials that can absorb a large fraction of the solar spectrum. This chapter focuses on the construction of a stable panchromatic layer-by-layer (LBL) assembly composed of a donor-acceptor conjugated polyelectrolyte pair absorbed onto a cationic liposome (DOTAP). It was shown that varying parameters such as temperature and the molar charge ratio of the conjugated polyelectrolytes can be used to control the morphology of these light harvesting complexes and manipulate their electronic properties.

5.1 Introduction

Conjugated polyelectrolytes (CPEs) are a class of quasi-1D structures whose delocalization of pi-electrons through their backbone enables the motion and transport of electrical charge and excitation energy; In addition, bear ionic sides chains per repeating monomer unit that enable these non-polar macromolecules to be water soluble. This sets them aside from other conjugated polymers whose processability and applications were limited to organic solvents. Their water solubility and prospects for environmental processability has made them attractive to applications in biomedicine and sensors.[1–13] They have a strong correlation between their physical structure and their electronic properties, have made them attractive candidates as basis for constructing light harvesting antennae.

Our work has focused on the self-assembly and photophysical behavior of conjugated polyelectrolytes (CPEs) for efforts to construct an artificial light harvesting system inspired by naturally photosynthetic machinery. It has shown that complexation of oppositely charged polyelectrolytes leads to emergent electronic excited states and rapid energy transfer dynamics between electronically coupled donor-acceptor CPEs.[14] We have constructed larger order assemblies composed of ionic and non-ionic surfactants. Through that work it was found that CPE-ionic surfactant interactions out-compete inter-CPE complexation and have a significant influence on the excitonic wavefunction of CPEs[15], where depending on the charge and charge density of micelles, they can template the CPE backbone and influence their microstructure. In this work we continue investigating the relationship and interaction of CPEs with amphiphilic systems. A cationic liposome (DOTAP) is used

as a template to build ionically assembled layer-by-layer (LBL) light harvesting system.

To the best of our knowledge, this is the first work done in creating a panchromatic donor-acceptor layer by layer CPE assembly onto a cationic lipid membrane. Previous work in CPE-lipid complexes, has solely focused on the absorption of single CPE to a lipid membrane surface or incorporation of small molecules, this the first of adding two oppositely charged CPEs onto a membrane surface in a layer-by-layer assembly in efforts to energy funnel like architecture. The chemical structures of the donor and acceptor CPEs, PFPI and PTAK are shown in **Figure 5.1** along with the cationic lipid, DOTAP.

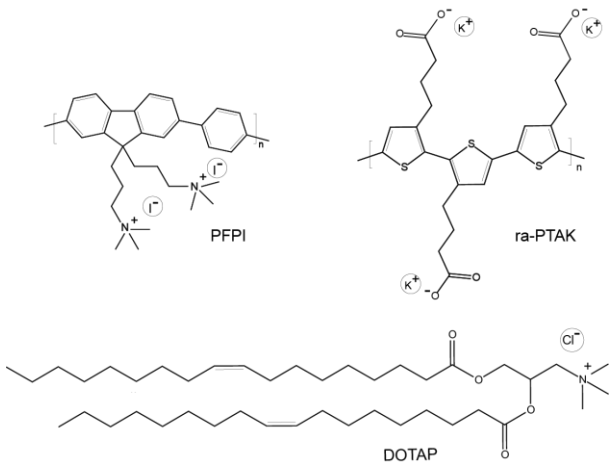

Figure 5.1 Chemical structures of conjugated polyelectrolytes and cationic lipid.

5.2 Results and Discussion

5.2.1 Regio-random DOTAP Complexation Behavior

As in previous work done in the complexation behavior of CPEs, thermal energy is needed to unwind the native conformational state of ra-PTAK and has shown to have

tremendous influence in the binding of oppositely charged species. In this work it has been shown to play a big role in the adsorption of ra-PTAK to the surface of DOTAP liposomes as shown from transmission and fluorescence images of ra-PTAK/DOTAP liposomes prepared at different temperatures (**Figure 5.2**). ra-PTAK/DOTAP liposomes prepared at room temperature showed poor adsorption of ra-PTAK to the DOTAP liposomes, this is clearly seen in comparing transmission image (**Figure 5.2A**) that shows several liposomes in the frame of the image in contrast to the corresponding fluorescence image (**Figure 5.2D**) a small fraction of the liposomes in the same image frame show fluorescence from ra-PTAK. This in contrast to ra-PTAK/DOTAP liposomes prepared at 70˚C (**Figure 5.2C/F**), 70˚C – fully covered, spherical, non-aggregated dispersed fluorescent liposomes. However, there seems to be something exclusive to elevated temperatures 70 ˚C, temperature dependence indicates

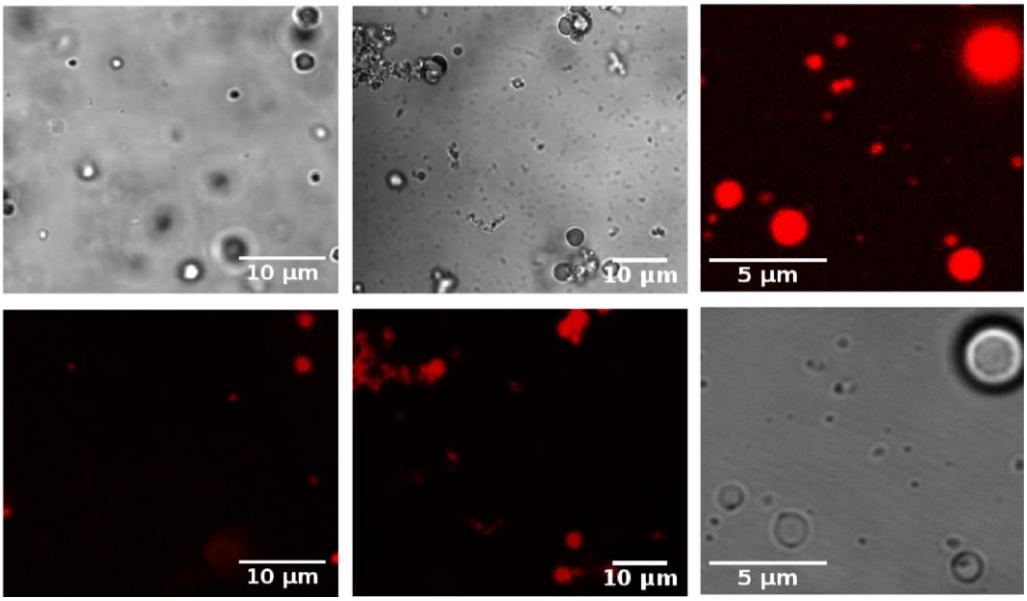

Figure 5.2 Temperature dependence CLSM Images ra-PTAK-DOTAP Complexes

that along with previous work[14–16] there is a type of microstructural change that the ra-PTAK backbone undergoes that optimizes its binding/interaction to the DOTAP surface.

Intermediate temperatures such as 35 ˚C lead to unstable ra-PTAK/DOTAP complexes, while there does seem to be an increase in the interaction between the CPE and liposomes based on the overlap of the corresponding transmission and fluorescence images there was a higher degree of aggregation , asymmetric complexes, as opposed to samples prepared at 70 ˚C. Its interesting to note from previous work done between in the interaction done between anionic ra-PTAK and cationic micelles DTAC, no additional heat was necessary for the unwinding and complexation of ra-PTAK to the DTAC micelles. This may have to due to the equilibria between DTAC micelles and single DTAC molecules, the hydrophobic tail of the DTAC surfactants are able to interact with the hydrophobic backbone of ra-PTAK disrupting pi-pi stacking of the backbone without additionally needed thermal energy. Liposomes don't have this type of monomer vesicle equilibria, therefore rely on thermal energy in the unwinding and disruption of pi-pi stacks prior to the

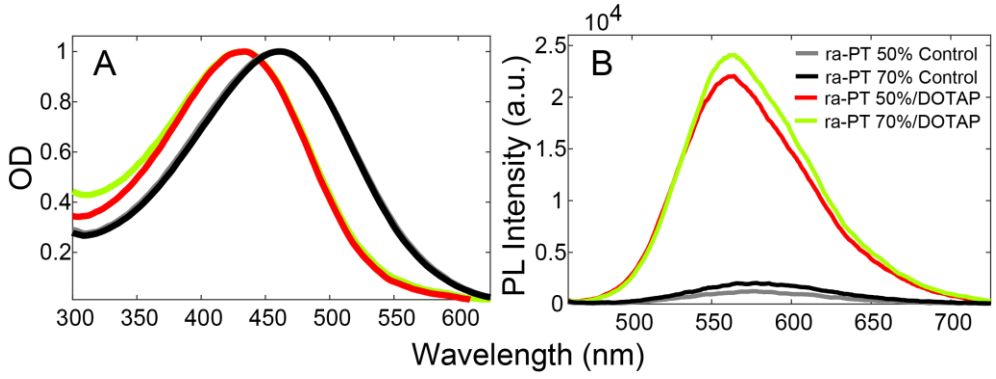

Figure 5.3 Steady State Spectroscopy OD (A) and PL (B) of ra-PTAK-DOTAP Complexes

adsorption of the CPE to its surface.

The results of the steady-state spectroscopy measurements (**Figure 5.3**) were complementary to microscopy images, indicate the binding/interaction of ra-PTAK to DOTAP. Upon binding the absorption of ra-PTAK undergoes a ~30nm blue shift from a λ_{max} of ~460nm to ~430nm, along with a turning on of the ra-PTAK emission when bound to DOTAP liposome by an order of magnitude. This coincides with previously mentioned work on ra-PTAK binding behavior to oppositely charged micelles.

Having established the temperature dependence binding behavior, coverage dependence of ra-PTAK(%):DOTAP(%) was done. The ra-PTAK/DOTAP complexes were prepared at molar charge ratios based on the anionic charge per ra-PTAK monomer unit and charge per DOTAP cationic head group. It was found through a series of increasing the molar charge ratio of ra-PTAK relative to DOTAP from 50-120%, that DOTAP liposomes were fully covered near ~ 50%-80% ra-PTAK

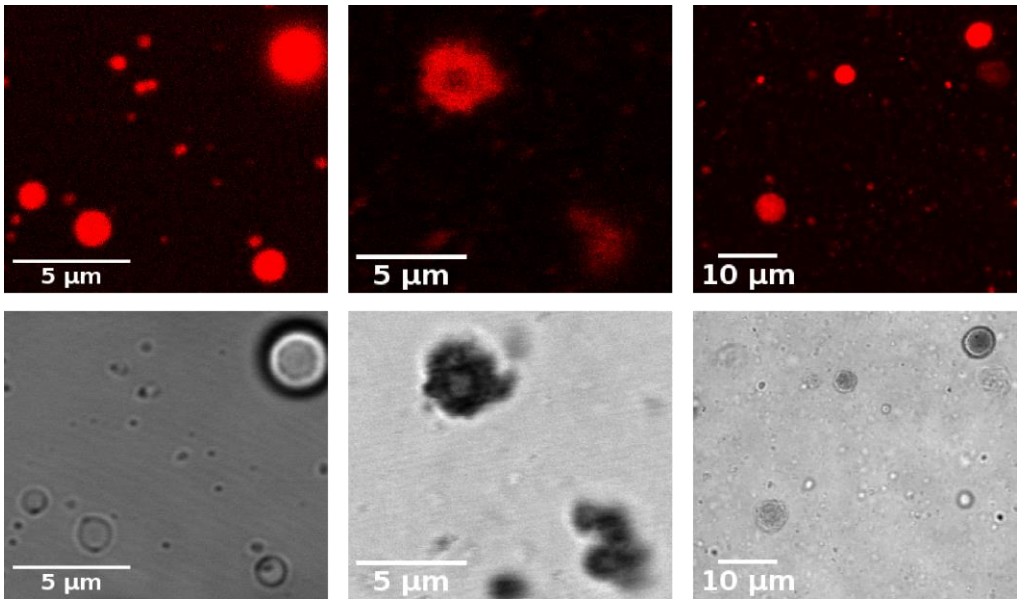

Figure 5.4 Temperature dependence CLSM Images ra-PTAK-DOTAP as a function of ra-PTAK concentration Complexes

molar charge coverage. Above 80% there is obvious hairiness observed on the surface of the liposomes

The microscopy images coincide with SAXS curves collected from the same sample set. While microscopy can give insight in the micrometer length scale, SAXS complements it by accessing nano length scale information; ranging from the backbone structure of the CPE, bilayer structure, and side chain interactions.[17–20]

Qualitatively the SAXS curves look different with the increased coverage of ra-PTAK added. As seen from the low Q of the SAXS curves (**Figure 5.5**), progressive addition of CPE leads

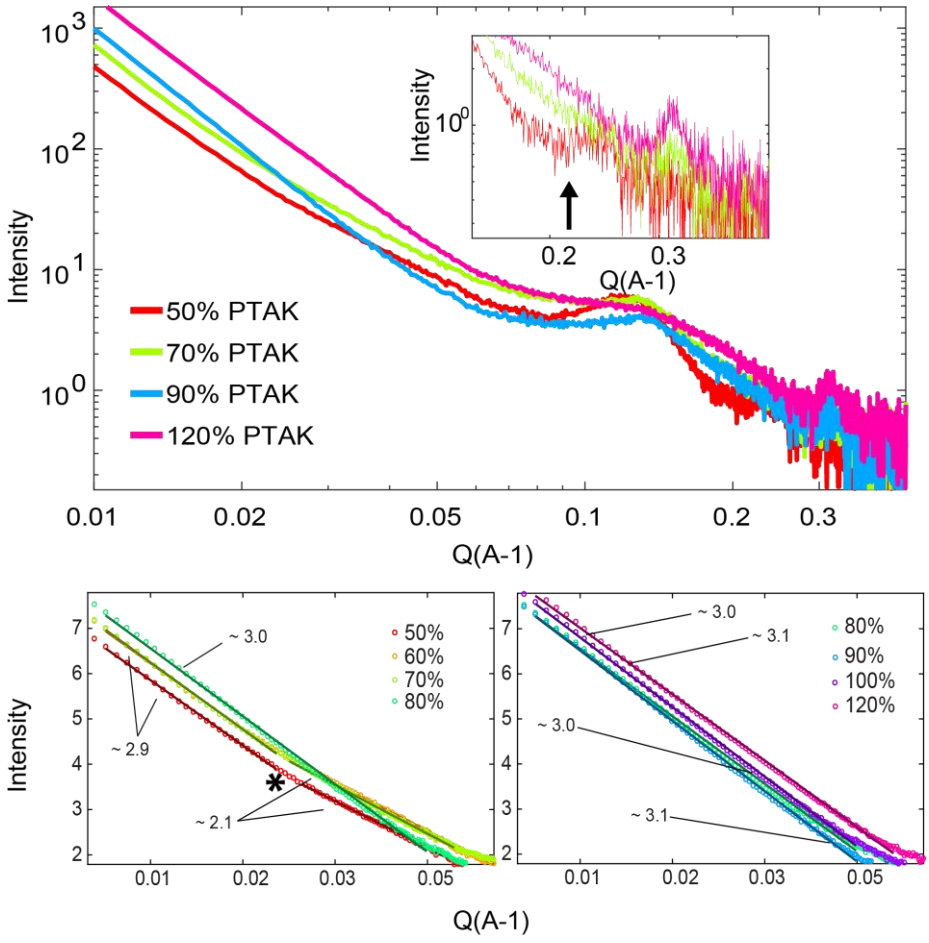

Figure 5.5 SAXS profiles and linear fits of ra-PTAK-DOTAP complexes as a function of ra-PTAK concentration Complexes

to higher aggregation. Through qualitative inspection at the low Q region it may seem that all curves have a constant linear slope, however, through closer inspection there is a change in slope for the lower percentage PTAK covered liposomes. By fitting this region of the SAXS profile for all samples, it is obvious that for samples covered with 50-70% ra-PTAK there is a slope change at Q*, while for samples with increased CPE coverage show a single linear slope of ~3. Past literature on solution SAXS of polythiophenes has used this Q* transition to obtain the persistence length[21–24] of the CPE backbone. It is clear there a structural change threshold between 70% and 80% that may be due to the packing of the CPEs on the surface. as increased concentration leads to higher proximity and interacting CPE chains

Diffusion Ordered Spectroscopy (DOSY-NMR) was used as another complementary method to characterize if ra-PTAK was binding to the DOTAP liposomes as well to distinguish any unbound ra-PTAK in solution. DOSY is often used to find the diffusion coefficient of macromolecules in solution and relate it to the hydrodynamic radius of molecules in solution[25–27], however in the case of the ra-PTAK/DOTAP Complexes, we know from the microscopy the complexes are highly polydisperse and reach sizes as large as 5-10 micrometers. We utilized NMR to trace the diffusion of the ra-PTAK and DOTAP based on their unique chemical shifts. Specifically, the aromatic region of ra-PTAK backbone, that is far enough downfield from the rest of the other resonances that it is distinguishable from those of the lipid protons.

We initially measured the DOSY NMR of ra-PTAK (**Figure 5.6A**), as can be seen with increasing gradient strength, the aromatic region decreases. The aromatic

region is highlighted using a transparent blue box. The integrated area intensity of aromatic region as a function of increasing gradient strength for each step clearly decays as shown in the inset of **Figure 5.6C**. Due to the large sizes of the raPTAK/DOTAP complexes there was no decay of the downfield protons between the gradient steps of the DOSY measurement concomitantly the aromatic region in the ra-PTAK/DOTAP complex disappears. This lose of the resonance is an indication that the raPTAK backbone is bound to the DOTAP liposomes due to the slow molecular rotation of the aromatic backbone due to it being bound to such large complexes.

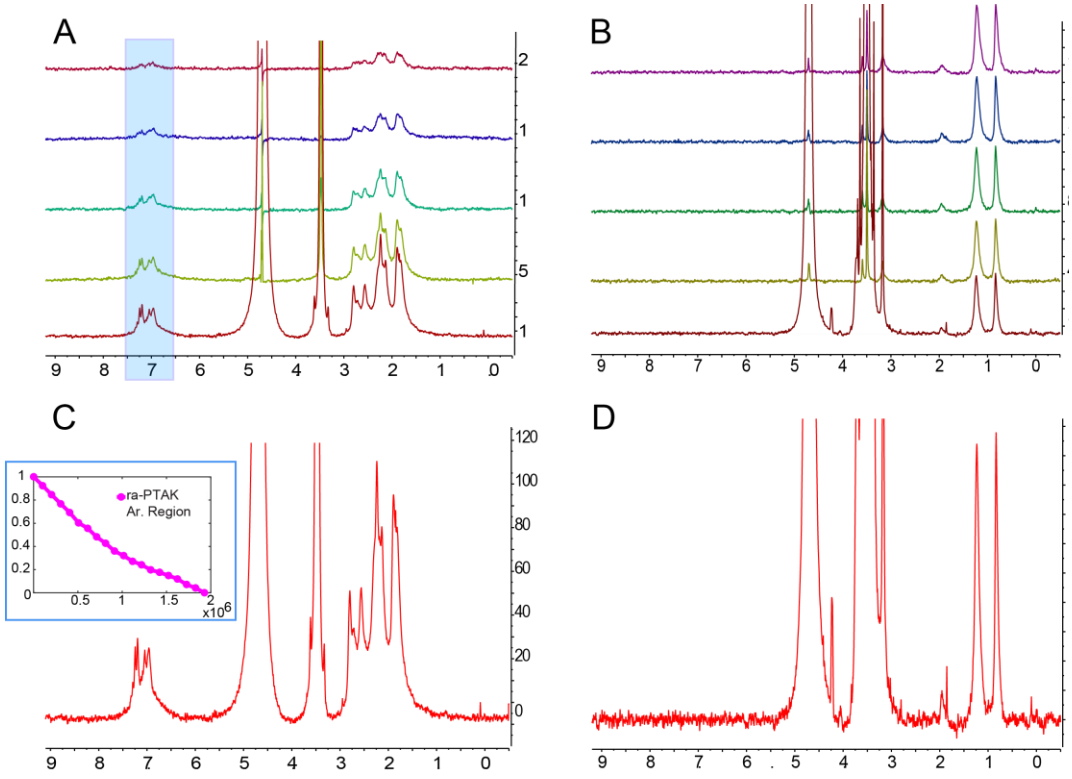

Figure 5.6 ra-PTAK 1D H NMR (C) and DOSY (A) ra-PTAK -DOTAP DOSY (C) and 1D HNMR.

5.2.2 Layer by Layer Donor – Acceptor – Liposome Assemblies

Having established the formation of donor covered liposomes we followed by adding the acceptor PFPI to form the layer by layer donor-acceptor assembly. Liposomes with 50% and 70% ra-PTAK coverage were chosen. These coverages were chosen due to the work mentioned in the previous section; liposomes prepared with these coverages showed the smoothest, fullest covered, spherical and stable liposomes as complimented by both microscopy and SAXS. The donor-acceptor-liposome assemblies were prepared based on the molar charges of the CPEs relative to the molar charges 'binding sites' of DOTAP in solution, the two charges per donor monomer unit were considered.

The steady – steady absorption and fluorescence spectroscopy of the LBL assemblies are shown in **Figure 5.7**. The PFPI emission is significantly quenched, while there is an increase of emission from ra-PTAK. Note there is a broadening of the ra-PTAK absorption, indicating a conformational change in the ra-PTAK backbone leading to a wider populations of lower energy chromophores. OD showed little signs of

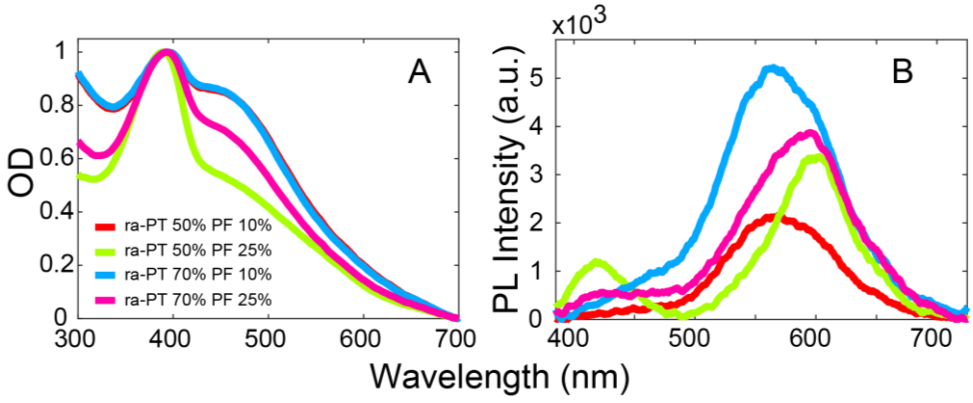

Figure 5.7 OD and PL of ra-PTAK/PFPI/DOTAP Complexes

scattering. Like in the previous work of cationic CPE interacting with similarly charged micelles. On its own PFPI is highly emissive, however, in the presence of other similarly charged surfaces, its emission intensity starts to decrease, possible as a result of PFPI collapsing in order to shield itself from similarly charged spheres.

To observe the contribution of PFPI to the ra-PTAK emission, an excitation spectrum was taken at an emission wavelength specific to the ra-PTAK, λ_{em}=600nm, shown in **Figure 5.8**. What can be observed from the PLE spectrum is that there higher contribution excitation wavelengths pertaining to the donor PFPI in the LBL

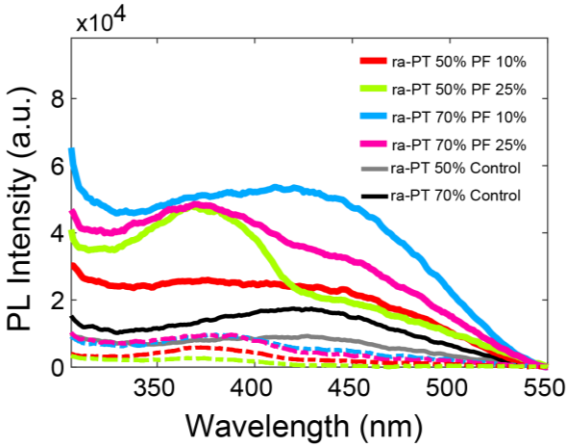

Figure 5.8 PLE of ra-PTAK/PFPI/DOTAP Complexes

complexes in comparison to raPTAK/DOTAP complex on its own. This observation is prominent for the LBL assemblies with higher fraction of the donor PFPI. This is an indication that electronic energy transfer occurring between the two CPEs.

The microscopy showed changes in the ra-PTAK/PFPI/DOTAP assemblies based on the ra-PTAK/PFPI charge composition as well. We notice that for assemblies where the liposomes are initially covered with ra-PTAK at 50% molar charge coverage, followed by the addition of PFPI, the ra-PTAK/PFPI/DOTAP assemblies have highly asymmetric assemblies. Comparing the PTAK and PFPI emission images, second and third column respectively, it is clear that CPEs are co-

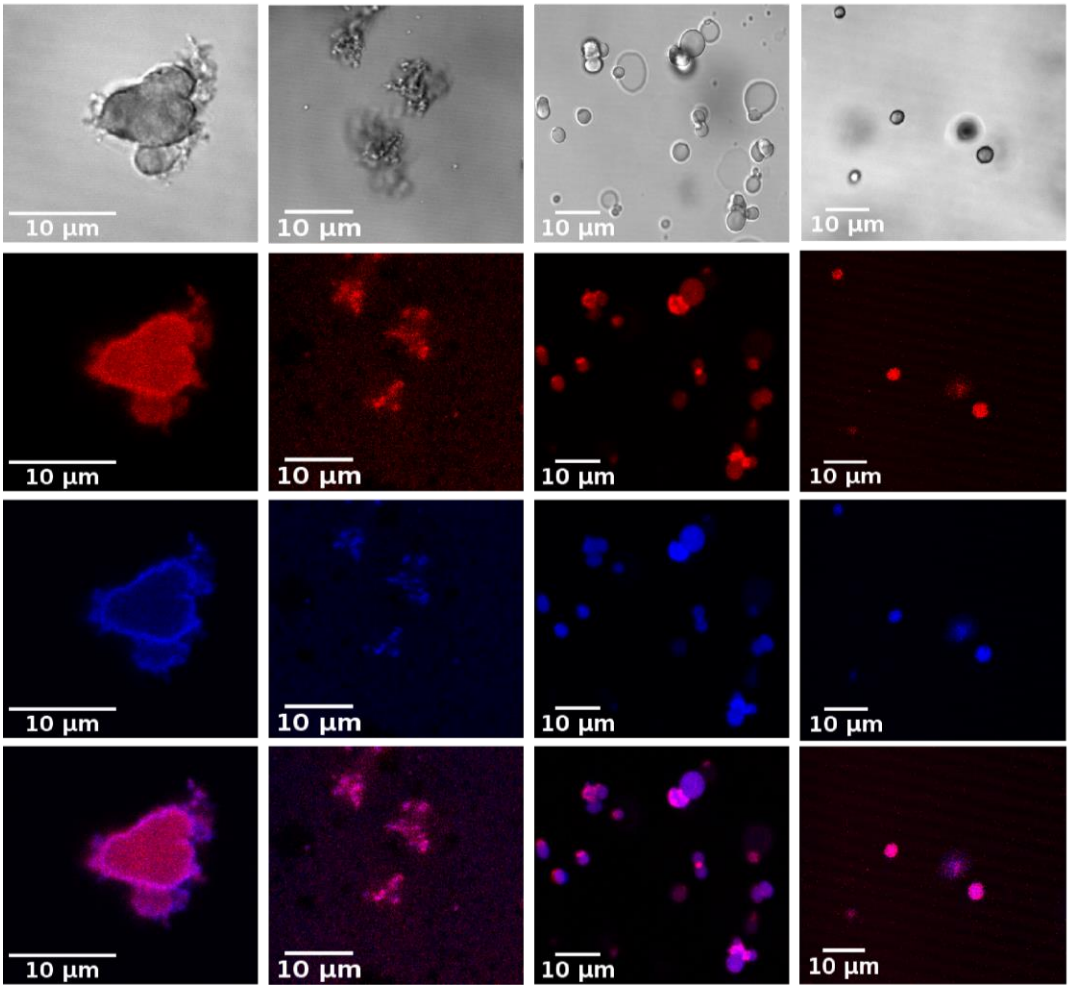

Figure 5.9 CLSM Images ra-PTAK/PFPI/DOTAP as a function of molar charge ratio

localized on the membrane of the asymmetric membrane scaffold, the bottom column shows the composite of those two images. When the molar charge ratio lessens

between the acceptor to donor, i.e. for the ra-PTAK(50%)/PFPI there is a higher degree of aggregation. Its possible that PFPI behaves as a binding agent, when there is less of an excess of the acceptor on that surface, such that it bridges several ra-PTAK/DOTAP liposomes, that leads to the merging or aggregation of individual liposomes. For the 70% there are enough ra/PTAK binding sites for the PFPI, however, bridging of different liposomes is still seen, its important to note that raPTAK/DOTAP complexes on their own don't lead to this multiple bridged or aggregated liposomes only when PFPI is present.

The SAXS profiles of the raPTAK/PFPI/DOTAP complexes all show the characteristic bilayer bump centered at ~0.13Å^{-1}, again corresponding to the bilayer thickness of the liposomes. The raPTAK(70% to PFPI(10%) DOTAP lbl sample showed a sharp in this region, indicating higher periodicity pertaining to this bilayer

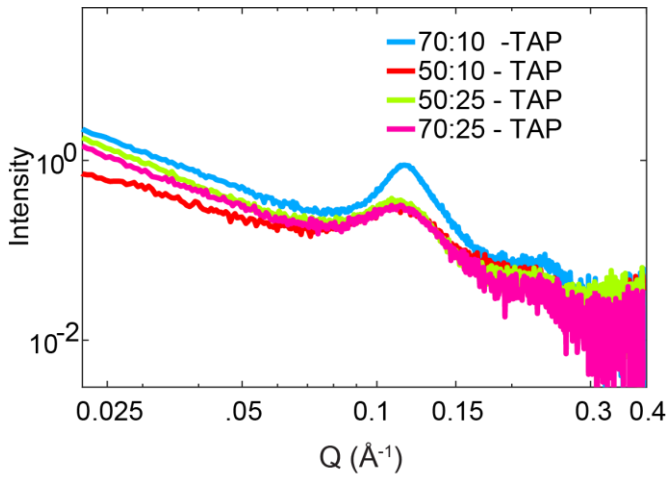

Figure 5.10 SAXS of ra-PTAK/PFPI/DOTAP Complexes

length scale. This higher periodicity is an indication that these samples have a higher number of multilamellar liposomes in solutions.[28,29]

Similar to the higher concentration of ra-PTAK/DOTAP complexes there is a pronounced bumped centered at ~0.25$Å^{-1}$ a 0.5$Å^{-1}$ distance larger that corresponding the side chain interaction of the ra-PTAK sidechains due to the packing of ra-PTAK on the DOTAP surface. However, there is an obvious decrease in the sharpness of the peak along with a broadening. Indicates that the addition of PFPI causes disrupts the microstructural ordering of the ra-PTAK chain on the DOTAP surface, creating a wider distribution of different local CPE side-chain interactions.

NMR was used again as a complementary and supplemental technique to characterize the binding of PFPI to the prepared ra-PTAK/DOTAP liposomes. **Figure 5.11** shows representative H NMR spectra of the CPEs on their own (A/C) and complexed to together without and with DOTAP present (figure B and D respectively). The separation of the aromatic region of the PFPI and ra-PTAK is convenient in that it allows the individual tracking and discrimination of the CPEs. Therefore, if they didn't bind or there was unbound PFPI in solution, its diffusion could be tracked. As expected, due to the large sizes of the ra-PTAK/PFPI/DOTAP complexes there is no trackable DOSY decay, however, the individual CPEs and CPE Complex without DOTAP present there is a trackable decay for the NMR peaks pertaining to the CPEs. There is an increased in broadness of the resonance peaks, this is to be expected that the complexes of the ra-PTAK and PFPI would lead to larger complexes and would in turn lead to broadening of this peaks.

Further indication, that a LBL assembly is being formed, where the donor (PFPI) is primarily docked on the outer surface of the LBL assembly is the sharpness of NMR peaks specific to its side chain protons while its aromatic region is gone, free rotation of side chain but not backbone because it is bound to such large LBL liposome assemblies.

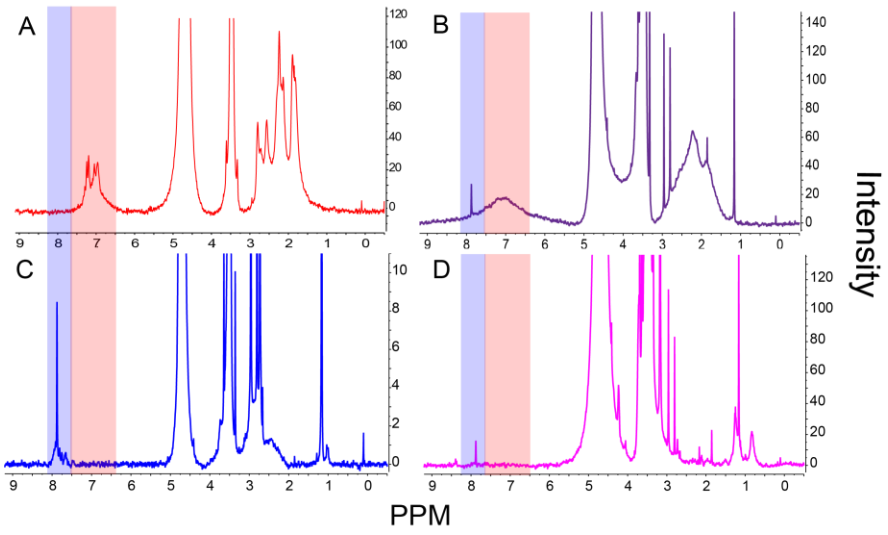

Figure 5.11 NMR of ra-PTAK (A), PFPI (C), ra-PTAK/PFPI (B) and ra-PTAK/PFPI/DOTAP Complexes (D)

5.3 Conclusion

In summary, we have constructed a layer-by-layer assembly composed of electronically coupled CPEs (PFPI and ra-PTAK), that cover a wide range of the UV/Vis spectrum and are able to undergo energy transfer. Temperature was shown to play a significant influence in the binding of the acceptor (ra-PTAK). In the LBL assembly it was shown that polyion ratio plays a significant role in the morphology of CPE covered liposome assemblies as well as local CPE microstructural ordering and changes in the electronic excited states.

5.4 Experimental Methods

Materials

The cationic polyfluorene CPE (PFPI) (average MW = 21,000 Da; polydispersity = 1.2) was obtained from Solaris Chem Inc. The anionic regiorandom polythiophene CPE (ra-PTAK) (average MW = 8,000 Da; polydispersity = 1.8) was obtained from Rieke Metals. Tris(hydroxymethyl)aminomethane (Tris) was obtained from sigma aldrich. Sodium chloride (NaCl) was obtained from sigma aldrich. The cationic lipid, 1,2-dioleoyl-3-trimethylammonium-propane (chloride salt), 18:1 TAP (DOTAP) was purchased from Avanti (Alabaster, AL). All materials were used as received.

Sample Preparation

Buffer solution:

Samples were all prepared from the same buffer solution. The buffer solution was fixed at 20mM Tris/ 25mM NaCl concentrations. They were diluted from separate 100mM Tris and 100mM NaCl stocks.

Preparation of liposomes:

Solid DOTAP was dissolved in chloroform to obtain a final concentration of 10 mg mL−1. The solvent was then evaporated by gently blowing N2 over the surface to create a thin film on the bottom of a borosilicate vial. The film was dried overnight under vacuum, to allow the evaporation of any residual chloroform. Films were hydrated to final concentrations between 5-20 mM with prepared buffer solution. The films were then sonicated for 5min in order to suspend the liposomes into the aqueous

solution. The lipid stock was then extruded with a Mini-Extruder (Avanti Lipids) with a 200 nm pore size polycarbonate membrane to reduce them to smaller polydiesperse liposomes.

ra-PTAK/DOTAP and ra-PTAK/PFPI/DOTAP Solutions:

The ra-PTAK/DOTAP solutions were prepared with respect to the charge per CPE monomer to charge per DOTAP charge in solution. The DOTAP concentration was fixed to 2mM for all solutions, the ra-PTAK concentration was adjusted to achieve the desired ra-PTAK (%) / DOTAP (%) molar charge ratio.The solutions were prepared as follows: ra-PTAK from previously prepared stock (24.3mM) was titrated to 2mM DOTAP solutions while stirring. The ra-PTAK/DOTAP solutions where stirred under heat for 2hrs at 70C and allowed to cool down on the hot plate. For layer-by-layer solutions, PFPI was added at a desired ra-PTAK (%) / PFPI (%)/DOTAP (%) molar charge ratio. PFPI was added to ra-PTAK/DOTAP solutions that have been stirring for two hours at 70C, PFPI/ra-PTAK/DOTAP solutions stirred for a continued 5mins at 70C, followed by rapid transfer of the solutions to an ice-bath for 30 minutes. All solutions were stored at 4C.

Small-Angle X-ray Scattering (SAXS)

SAXS measurements were performed at beamline 4−2 at the Stanford Synchrotron Radiation Laboratory (SSRL) using a Rayonix MX225-HE detector. The incident photon energy was 11 keV X-ray (1.17 Å), and the sample-detector distance was 2.5 m. Multiple 1s exposures were taken and averaged prior to analysis. To avoid

degradation, samples were oscillated during data collection. SasTool (SSRL) was used to convert collected 2D TIFF images to intensity vs scattering vector length and to subtract solvent scattering (HPLC water). SAXS measurements were also performed at the Advanced Light Source (ALS, Lawrence Berkeley National Laboratory). Experiments were conducted with a 1.5 m sample-to-detector distance at 11 keV at the SIBYLS beamline. We found excellent agreement between measurements made at both synchrotron facilities. Pair distance distribution functions were calculated using the indirect Fourier Transform (Glatter).

Steady-State Spectroscopy

Optical density measurements were taken with a Shimadzu UV-2700 Spectrophotometer at 1.0nm increments with an integration time of 0.1s and a 2.0 nm slit width over the desired range. Photoluminescence measurements were taken using a Horiba Fluoromax-4 spectrofluorometer in a right-angle geometry. The measured integration time was 0.5s. Both the emission and excitation slit widths were 2.5 nm. Both optical measurements used cuvettes with 1 mm pathlengths.

CLSM

CLSM images of the CPE/C-DOTAP liposomes were obtained using a Leica-SP5 confocal laser scanning microscopy (CLSM; Leica Microsystems Heidelberg GmbH, Heidelberg, Germany). Excitation wavelengths used were 405nm and 488nm. Emission bins collected were specific to the CPE, 415-435nm for PFPI and 625-

695nm for ra-PTAK. CPE/DOTAP samples were directed pipetted (5uL) onto 1.5 coverslip slide.

NMR Experiments

NMR measurements were performed on a Bruker AVANCE 500 MHz spectrometer. All CPE/-DOTAP samples were prepared in deuterated buffer. The 1H-PGSE NMR measurements were performed at 298 K with deuterium lock. A square gradient pulse was used with lengths of 30ms. Diffusion times used ranged from 150-200ms. All other parameters were left unchanged.

5.4 References

1. Duarte, A., Pu, K. Y., Liu, B. & Bazan, G. C. Recent advances in conjugated polyelectrolytes for emerging optoelectronic applications. *Chem. Mater.* **23**, 501–515 (2011).

2. Choi, H. *et al.* Conjugated polyelectrolyte hole transport layer for inverted-type perovskite solar cells. *Nat. Commun.* **6**, 7348 (2015).

3. Marques, A. T. *et al.* Spectroscopic properties, excitation, and electron transfer in an anionic water-soluble poly(fluorene-alt-phenylene)-perylenediimide copolymer. *J. Phys. Chem. B* **116**, 7548–7559 (2012).

4. Evans, R. C. Harnessing self-assembly strategies for the rational design of conjugated polymer based materials. *J. Mater. Chem. C* **1**, 4190 (2013).

5. Evans, R. C. *et al.* Cationic polythiop1. Evans, R. C. et al. Cationic polythiophene-surfactant self-assembly complexes: phase transitions, optical response, and sensing. Langmuir 28, 12348–56 (2012).hene-surfactant self-assembly complexes: phase transitions, optical response. *Langmuir* **28**, 12348–56 (2012).

6. Liu, X., Fan, Q. & Huang, W. DNA biosensors based on water-soluble conjugated polymers. *Biosens. Bioelectron.* **26**, 2154–2164 (2011).

7. Liu, Y., Ogawa, K. & Schanze, K. S. Conjugated polyelectrolytes as fluorescent sensors. *J. Photochem. Photobiol. C Photochem. Rev.* **10**, 173–190 (2009).

8. Wang, F. *et al.* Synthesis and Characterization of Water-Soluble Polythiophene Derivatives for Cell Imaging. *Sci. Rep.* **5**, 1–8 (2015).

9. Huang, Y. *et al.* Cationic Conjugated Polymer/Hyaluronan-Doxorubicin Complex for Sensitive Fluorescence Detection of Hyaluronidase and Tumor-Targeting Drug Delivery and Imaging. *ACS Appl. Mater. Interfaces* **7**, 21529–21537 (2015).

10. Feng, G., Mai, C. K., Zhan, R., Bazan, G. C. & Liu, B. Narrow band gap conjugated polyelectrolytes for photothermal killing of bacteria. *J. Mater. Chem. B* **3**, 7340–7346 (2015).

11. Wang, Y., Schanze, K. S., Chi, E. Y. & Whitten, D. G. When worlds collide: Interactions at the interface between biological systems and synthetic cationic conjugated polyelectrolytes and oligomers. *Langmuir* **29**, 10635–10647 (2013).

12. Costa, T. *et al.* Self-assembly of poly{1,4-phenylene-[9,9-bis(4-phenoxy-butylsulfonate)]fluorene-2,7-diyl} with oppositely charged phenylenevinylene oligoelectrolytes. *J. Phys. Chem. B* **118**, 613–23 (2014).

13. Fan, C. *et al.* Beyond superquenching: Hyper-efficient energy transfer from conjugated polymers to gold nanoparticles. *Proc. Natl. Acad. Sci.* **100**, 6297–6301 (2003).

14. Hollingsworth, W. R. *et al.* Exciton Transfer and Emergent Excitonic States in Oppositely-Charged Conjugated Polyelectrolyte Complexes. *J. Phys. Chem. B* **120**, 7767–7774 (2016).

15. Segura, C. J., Lucero, M. & Ayzner, A. L. Disassembly of an Interconjugated Polyelectrolyte Complex Using Ionic Surfactants. (2019). doi:10.1021/acsapm.9b00023

16. Hollingsworth, W. R. *et al.* Polyion Charge Ratio Determines Transition between Bright and Dark Excitons in Donor/Acceptor Conjugated Polyelectrolyte Complexes. *J. Phys. Chem. C* acs.jpcc.8b06195 (2018). doi:10.1021/acs.jpcc.8b06195

17. Fritz, G. & Bergmann, A. Interpretation of small-angle scattering data of inhomogeneous ellipsoids. *J. Appl. Crystallogr.* **37**, 815–822 (2004).

18. Ehmann, H. M. A. *et al.* Generalized indirect fourier transformation as a valuable tool for the structural characterization of aqueous nanocrystalline cellulose suspensions by small angle X-ray scattering. *Langmuir* **29**, 3740–3748 (2013).

19. Glatter, O.; Kratky, O. *Small Angle X-ray Scattering*. (Academic Press, 1982).

20. Iampietro, D. J., Brasher, L. L., Kaler, E. W., Stradner, A. & Glatter, O. Direct Analysis of SANS and SAXS Measurements of Catanionic Surfactant Mixtures by Fourier Transformation. *J. Phys. Chem. B* **102**, 3105–3113 (1998).

21. Bilger, D. *et al.* Multi-Scale Assembly of Polythiophene-Surfactant Supramolecular Complexes for Charge Transport Anisotropy. *Macromolecules* acs.macromol.6b02416 (2017). doi:10.1021/acs.macromol.6b02416

22. Gettinger, C. L., Heeger, A. J., Drake, J. M. & Pine, D. J. A photoluminescence study of poly (phenylene vinylene) derivatives : The effect of intrinsic persistence length. **1673**, (2003).

23. Borsali, R., Schappacher, M., Deffieux, A., Supe, Ä. N. & Cotton, J. P. Effect of Dense Grafting on the Backbone Conformation of Bottlebrush Polymers : Determination of the Persistence Length in Solution. 8878–8881 (2002). doi:10.1021/ma0203344

24. Beaucage, G. *et al.* Persistence Length of Isotactic Poly(hydroxy butyrate). **4**, 4158–4162 (1997).

25. Groves, P. Diffusion ordered spectroscopy (DOSY) as applied to polymers.

Polym. Chem. **8**, 6700–6708 (2017).

26. Jr, C. S. J. Diffusion ordered nuclear magnetic resonance spectroscopy : principles and applications. **34**, 203–256 (1999).

27. Valentini, M. *et al.* Diffusion NMR Spectroscopy for the Characterization of the Size and Interactions of Colloidal Matter: The Case of Vesicles and Nanoparticles. *J. Am. Chem. Soc.* **126**, 2142–2147 (2004).

28. Komorowski, K. *et al.* Vesicle Adhesion and Fusion Studied by Small-Angle X-Ray Scattering. *Biophys. J.* **114**, 1908–1920 (2018).

29. Pabst, G., Rappolt, M., Amenitsch, H. & Laggner, P. Structural information from\nmultilamellar liposomes at full hydration: Full q-range fitting with high quality x-ray\ndata. *Phys. Rev. E* **52**, 4000–4009 (2000).